Corrosion of Electronic and Magnetic Materials

Phillip J. Peterson

EDITOR

ASTM STP 1148

STP 1148

Corrosion of Electronic and Magnetic Materials

Phillip J. Peterson, editor

ASTM Publication Code Number (PCN)
04-011480-27

ASTM
1916 Race St.
Philadelphia, PA

Library of Congress Cataloging in Publication Data

Corrosion of electronic and magnetic materials/Phillip J. Peterson.
editor.
p. cm.—(STP; 1148)
Contains papers presented at the symposium held in San Francisco.
Calif., May 22, 1990, and sponsored by the ASTM Committee G-1 on
Corrosion of Metals.
"ASTM publication code number (PCN) 04-011480-27."
Includes bibliographical references and index.
ISBN 0-8031-1470-2
1. Electronics—Materials—Corrosion—Congresses. 2. Magnetic
materials—Corrosion—Congresses. I. Peterson, Phillip J.
II. ASTM Committee G-1 on Corrosion of Metals.
TK7871.C67 1991 91-42686
621.381—dc20 CIP

Photocopy Rights

Peer Review Policy

Each paper published in this volume was evaluated by three peer reviewers. The authors addressed all of the reviewers' comments to the satisfaction of both the technical editor(s) and the ASTM Committee on Publications.

The quality of the papers in this publication reflects not only the obvious efforts of the authors and the technical editor(s), but also the work of these peer reviewers. The ASTM Committee on Publications acknowledges with appreciation their dedication and contribution to time and effort on behalf of ASTM.

Printed in Philadelphia
1992

Foreword

This publication, *Corrosion of Electronic and Magnetic Materials,* contains papers presented at the symposium of the same name held in San Francisco, California on 22 May 1990. The symposium was sponsored by ASTM Committee G-1 on Corrosion of Metals. Phillip J. Peterson, IBM Corporation, San Jose, California, presided as symposium chairman.

Contents

Overview

Modern civilization has an insatiable appetite for ever faster and improved communication plus a never-ending desire to store, retrieve, and manipulate information no matter where we are, whether in our offices, stuck in a traffic jam on the freeway, or sunning ourselves on the beach. This desire and appetite has driven the use of electronic and magnetic materials to dimensions that are rapidly approaching atomic units, to include exotic materials for which little if any corrosion experience exists, and to survive hostile environments. Through global competition, these products must be produced at decreasing costs, increasing reliability, and decreasing development time.

The shrinking size of our electronic and magnetic devices have forced us to take a closer look at corrosion. We must extend our limits for what we call corrosion. Is Pourbaix's 10^{-6} limit still valid? Is what we used to consider mild inconsequential tarnish now to be considered devastating corrosion? This new closer look at corrosion is reflected in the papers of Rickett and Payer, Goodson and Chang, and Hadad and Pizzo.

In the past, engineers have shied away from using materials they had no experience with or for which they could not find corrosion data. At present and especially in the future, we cannot afford to do this and stay competitive. We must either produce our own corrosion data and/or encourage and facilitate publication of corrosion studies of new materials such as those by Kim and Camp; DeBold, Masteller, Werley, and Carpenter; and Lee and Stevenson.

Computer power that only a few years ago was found exclusively in clean, air-conditioned rooms that would rival medical operation rooms can now be found on laps by the seashore. Telephones now have such scanty protective covers that even Superman is taken back. Today we carry on our wrists through rain, snow, swimming pools, and saunas sophisticated electronic devices that would make Dick Tracy envious. And yet, thanks to global competition, many of these devices are so cheap we would rather discard them than replace their batteries. In the past, sophisticated electronic and magnetic materials were protected in hermetically sealed packages, a costly overprotection for most applications but requiring little knowledge of either the environment or its corrosive effects on these materials. But now, to be cost competitive, we must carefully define what is just-sufficient-protection for our products to survive the environment in which they are to be used. It is work like that of Schubert, Sproles, Setchell, and Yee and Bradford that enable cost competitiveness to be achieved without sacrificing product reliability.

To ensure the reliability of products with new materials or even old materials with new packaging, environmental exposure tests are required. From the pressures of competitive time development, it is desirable for many of these exposure tests to be accelerated and their results made available at the time the new product is introduced in the marketplace. To do this, preagreed upon tests accepted by vendors, manufacturers, and customers must be in place. It is here where ASTM will play an important role in the development of new electronic and magnetic materials.

Phillip J. Peterson

IBM Corporation, San Jose, CA 95193;
symposium chairman and editor

Rudolf Schubert,[1] Angelo Veca,[2] and Elizabeth Fischer[3]

Corrosion-Resistant Outdoor Electronics

REFERENCE: Schubert, R., Veca, A., and Fischer, E., "**Corrosion-Resistant Outdoor Electronics,**" *Corrosion of Electronic and Magnetic Materials, ASTM STP 1148,* P. J. Peterson, Ed., American Society for Testing and Materials, Philadelphia, 1992, pp. 1-10.

ABSTRACT: The operating telephone companies are committed to assuring reliable and continuous quality telephone service. Environmental durability must be designed into the components of the electronic coin telephone that is often located in uncontrolled environments and in areas of continuous exposure to corrosive pollutants. To observe and quantify the effect of the environmental pollutants on coin telephone equipment, functional but unhoused electronic printed circuit board assemblies, a fully assembled, unhoused electronic chassis and coin acceptor, and a fully housed electronic chassis and coin acceptor were placed in a chamber and exposed to a pollutant-containing environment along with copper, nickel, and electroplated gold control coupons. The test pollutant atmosphere was a Battelle Laboratories Class III atmosphere consisting of air at 30°C and 70% relative humidity with H_2S, Cl_2, and NO_2 at 100, 20, and 200 ppb, respectively. We report the results of Auger electron spectroscopy with Ar^+ ion depth profiling that was done on various electronic components from housed and unhoused circuit packs and the control coupons. In general, corrosion film thicknesses on circuit components were less than coupon film thicknesses. This is attributed to the circuit pack geometry and component shrouding. A theoretical model supports the experimental results. Repeated functional testing at 95% relative humidity of both the housed coin telephone and unhoused assemblies was performed after exposure in the polluted atmosphere. After exposure, all circuits performed according to specification with respect to laboratory central office equipment and a fully active coin operation telephone line.

KEY WORDS: corrosion, contacts, electronics, tin, gold, copper, nickel, nitrogen dioxide, chlorine, hydrogen sulfide, flowing mixed gas testing

Customers expect reliable and continuous quality telephone service, and the Bell operating companies (BOCs) are committed to assuring such service. Providing this level of service requires that environmental durability be designed into the components of coin telephone stations to assure reliability, to minimize the cost of field repairs, and to increase revenue. Electronic coin telephone station equipment is often located in uncontrolled environments and in areas of continuous exposure to corrosive pollutants with the external telephone housing acting as the primary barrier to the expected pollutants. The pollutant compounds of interest include NO_X, O_3, SO_X, H_2S, and Cl-containing molecules in urban, outdoor, street-level environments [*1-3*]. Furthermore, the equipment must tolerate various salts and organic vapors at relative humidities as high as 100% and operate over a temperature range of -34 to $+66$°C.

A number of simulated environmental tests already exist, i.e., salt fog [*4*], sulfur dioxide [*5*], humidity, and temperature cycling [*6*], as well as numerous modifications to these tests. These tests are of questionable use for general atmospheric corrosion for electronic devices. For example, the salt fog test simulates an atmosphere found primarily on the seacoast or on

---

[1] Bellcore, Red Bank, NJ 07701.
[2] Mars Electronics International, Inc., West Chester, PA 19380.
[3] NYNEX Enterprises, New York, NY 10001.

board seagoing vessels. The sulfur dioxide (SO_2) test uses concentrations greatly in excess of normal atmospheres and does not include any chlorine-containing gas. Humidity and temperature cycling do not include any specific pollutants. The Battelle Laboratories flowing mixed gas test [7] overcomes the above objections by using chlorine (Cl_2), hydrogen sulfide (H_2S), and nitrogen dioxide (NO_2) gases at the part per billion (ppb) level.

Most people are familiar with the outside of a coin-operated telephone terminal. It is an enclosure which has few accesses for the intake or exhausting and exposure of the electronic components to flowing pollutant gases. However, there are flow paths that allow the housing to intake or exhaust gases caused by atmospheric temperature and pressure changes and wind-induced venturi effects. These accesses are located at the rear of the terminal housing for mounting and wiring purposes, in the front by the coin slot, the coin return chute, and the vault door, and at the interface between the upper and lower housing. In addition, the system components are fully exposed to the outside street atmosphere during short periods of time while the upper housing is removed for maintenance.

The internal housing volume is approximately 10 L, and the internal components' volume utilizes approximately 6 L. The remainder is free space. The internal surface area of the covered electronic chassis and coin chute exposed to the enclosed atmosphere (not including the inner housing walls) is approximately 1900 cm^2, of which 1300 cm^2 is plastic and the remainder is printed circuit board and metal chassis. Other internally exposed surfaces were not assessed. However, it is noted that these internal surfaces appear to be bare (and unpassivated) metal consisting of carbon steel and brass, except for paint overspray on the inside of the upper and lower housings. The major portions of the external upper and lower housing surfaces are painted, and various external components such as the switch hook, key-pad dial bezel, coin return door, handset retainer, and instruction placard trim and bezels are chromium plated. However, it is the electronics which are of prime importance with regard to corrosion.

In this paper, we report the results of accelerated atmospheric corrosion testing of the electrical components from electronic coin telephones. Surface analysis shows substantial corrosion occurring on copper surfaces and gold electroplated surfaces, but minimal corrosion on tin or shrouded surfaces. All electronic components worked as specified after the exposure.

Experiments

The equipment subjected to the flowing mixed gas corrosion chamber (FMGCC) test discussed below were Mars Electronics modular retrofit components and a complete system for coin-operated telephone sets.[4] The retrofit system (LES-100-WE) consists of an electronic communication and control chassis and an electronic coin chute. The sample materials for corrosion testing were randomly selected from production output that were manufactured according to Mars' standard processes and specifications. Then they were acceptance tested according to established test protocols which are proprietary.

The printed circuit boards were manufactured using FR4 material, subtractive process, and solder mask over print wires. This process meets surface insulation resistance requirements in accordance with established measuring procedures [*8*]. Printed circuit board layout and design are consistent with various industry standards and recommended techniques [*9*].

The separable connectors used to interconnect the circuit boards and components are typically AMPMODU styles manufactured by AMP. These are made from a copper alloy strip which is nickel and tin plated in certain areas and then selectively gold plated in the contact

---

[4] These new units were designed to convert the existing analog coin telephone to a centrally diagnosable, digital telephone.

regions. Finally, the strip is stamped and formed into the individual contacts. This process leaves exposed edges of copper alloy from the stamping operation at several locations.

Other than assuring printed circuit board cleanliness prior to and subsequent to manufacture, no special processing or substances are used to specifically guard against or retard the possible effects of exposure to aggressive atmospheric contaminants. Cleanliness of the printed circuit boards is established by using recognized industry cleaning methods after assembly, i.e., a 104°C CFC-6% methanol process suitable for removal of solder flux or temporary solder resist materials. Cleanliness is maintained throughout the assembly and test process by operators wearing protective gloves to avoid the deposition of residues resulting from perspiration.

In order to gain the maximum amount of information from the test samples, the experiment was arranged to expose a variety of electronic components at different stages of assembly, as well as multiple control coupons. A set of individual printed circuit boards with a full complement of components, a set of printed circuit boards assembled as a chassis mount pack, a mount pack assembled into a chassis without covers, a completed chassis with covers, a chassis installed in a lower coin-operated telephone housing without upper housing, and a completely assembled coin-operated terminal as would be placed into operation in the street environment were all exposed in the FMGCC. In total, the electronic components sample consisted of seven sets of electronic printed circuit boards exposed in a manner to range from minimum protection to maximum protection from a corrosive mixed gas atmosphere. Three types of control coupons, electroplated acid hard gold over sulfamate plated nickel over copper, pure copper (Cu), and pure nickel (Ni), were placed inside the assembled housing, on the housing surface, and at several other free-standing locations near the circuit packs. The control coupons' function was to provide visual verification that corrosion was proceeding normally during the test [7].

Each set of boards was assembled into a complete chassis prior to exposure, and the chassis was tested for full operation and functionality on a live coin-operated telephone line and then disassembled to the necessary state in preparation for the FMGCC test.

Individual circuit boards, assembled components, a fully assembled, working, housed coin telephone, and metal control coupons were all tested together in Battelle Laboratories' (Columbus, OH) FMGCC [7] for seven days. The exposure atmosphere was 100 ppb H_2S, 20 ppb Cl_2, and 200 ppb NO_2 in air at 30°C and 70% relative humidity (RH); this corresponds to a Class III environment [7]. Chamber air was exchanged six times per hour. Pollutant gases were stabilized prior to insertion of the samples; all conditions were monitored continuously except Cl_2, which was only verified at the beginning and the end of the experiment. All component sets were electrically isolated and spatially separated by at least 5 cm. After exposure, all electrical components were functionally tested to manufacturing specifications.

The process of functionally testing the exposed sets of electronics consisted of three phases: (a) under ambient laboratory conditions of 22°C and 56% RH after FMGCC exposure; (b) after equilibrating for 24 h in an environment of 60°C and 95% RH after (a); and (c) after equilibrating with the ambient laboratory conditions of 25°C and 54% RH subsequent to the 60°C and 95% RH test.

In addition to the three completely assembled sets, i.e., a set in the complete housing, a set in the lower housing without upper housing, and a set in the complete chassis with covers but no housing, the remaining exposed free-standing printed circuit boards were assembled into chassis in order to facilitate operational tests.

The coin telephone operates from power supplied to the "tip-ring" telephone terminals from the telephone central office at the specified telephone line voltage ranging from 42.5 to 52.5 Vdc and telephone loop currents ranging from 23 to 80 mA. No telephone line power is required in the "on-hook" condition.

The objective of the operational tests subsequent to exposure was to assure that the performance and functions of the Mars' Modular Electronic Retrofit System satisfied the specified operating requirements. This included: (1) receive, transmit, and side tone audio quality; (2) electronic data acquisition, processing, and retention; (3) transmission of station status, alarms, and scheduled reports; (4) dual tone multifrequencies and tone quality; (5) coin tone quality and frequencies; (6) coin acceptance, central office coin collection, and coin return. These specification values are listed in Table 1. Other properties tested were dielectric withstand, electrostatic discharge immunity, and the on-hook/off-hook impedances [*10*]. These functions all operate on a voltage of 6.8 to 7.0 V.

After FMGCC exposure and electronic testing, the components were inspected and analyzed by Auger electron spectroscopy (AES). A Perkin-Elmer PHI 600 spectrometer was used with an 80-namp, 10-keV electron beam used in the spot mode for analysis. Depth profiling was done with a 3-keV argon ion (Ar^+) beam with an effective sputtering rate in silicon dioxide (SiO_2) of 9.1 nm/min. For some thicker films, the sputtering rate was increased to 13.5 nm/min. No cleaning of the samples was done prior to analysis. No analysis was done in visible scratches, wear marks, or debris. Areas chosen for analysis were considered typical of the surfaces, for both exposed and unexposed samples.

Results

The electroplated acid hard gold over sulfamate plated nickel over copper, pure copper, and pure nickel control coupons showed different degrees of corrosion depending on whether they were exposed in a free-standing position or within the coin telephone housing, as expected. Those samples exposed within the housing showed no visible corrosion. Figure 1 is a photograph of plated gold (Au) samples; the bright Au sample on the right was mounted inside of the housing, and the corroded sample on the left was mounted directly on the outside of the housing. Clearly, substantial pore corrosion occurred on the sample outside of the housing. Both the Ni and Cu samples exposed on the outside of the housing had turned black after the seven-day exposure, whereas the Ni and Cu coupons inside the housing showed no evidence of corrosion. Thicknesses of the corrosion films on the control coupons are given in Table 2 and were determined by coulometric reduction. The corrosion films on unprotected samples were sufficiently thick that no AES depth profiles were obtained.

The upper and lower housings were serviceable units that had prior field usage for an unspecified period of time. On areas where there were scratches in the painted surfaces, the scratches appeared to be blackened subsequent to exposure. No analysis was performed on the housings.

Although no specific analyses were done on any of the nonmetallic surfaces after the seven-

TABLE 1—*Some electronic functions and typical requirements.*

Function	Examples	Specifications
Audio quality and loudness	Transmit, receive, side tones	Over 4.5 km with 26 AWG wire, ±50 dB loudness
Digital data	Acquisition, retention, alarm/report	1200/2400 Baud
Analog data	Coins, dialing, voice	Frequency, ±8 Hz Amplitude, <10 dBm loss Timing, tens of ms

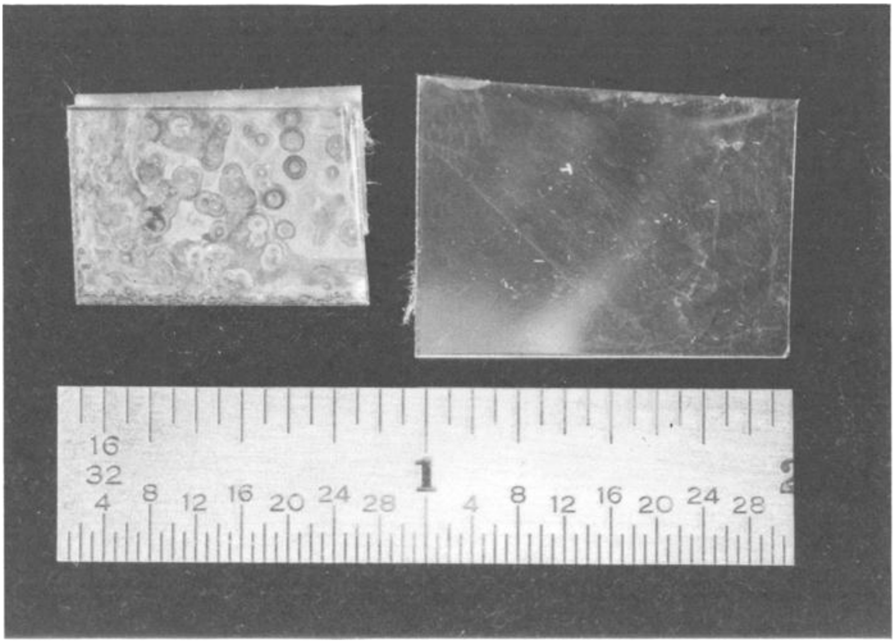

FIG. 1—*Porous gold plate control coupons exposed for seven days in the FMGCC. The sample on the left was inside the coin telephone housing, and the sample on the right was on the outside surface of the housing.*

day FMGCC exposure, visual inspection did not show any cracking, crazing, discoloration, or delamination. These surfaces will not be discussed further.

Visual inspection of the exposed tinned electrical components showed minimal corrosion. Exposed, unhoused tin surfaces showed a dulling and slight whitening as compared to the exposed, housed tin (Sn) surfaces, which retained their smooth and bright finish. Exposed, unhoused electroplated Au surfaces on some DIP lead frames had sufficient corrosion on the surface such that they appeared to be made of Cu.

A typical AES analysis of a Sn surface is shown in the differentiated spectrum in Fig. 2. Sn is the major component with lesser amounts of oxygen and carbon and with traces of sulfur and chlorine, which can all be attributed to typical adsorption of air components. Ar^+ depth profiling of this spot indicates that the surface contamination is less than 5 nm thick, i.e., the

TABLE 2—*Equivalent film thicknesses on Cu control coupons.*

Exposure Time, h	Location	Average Film Thickness, nm
48	Chamber	266
96	Chamber	377
145	Chamber	454
168	Chamber	605
168	On housing	600
168	In housing	33
192	Chamber	653

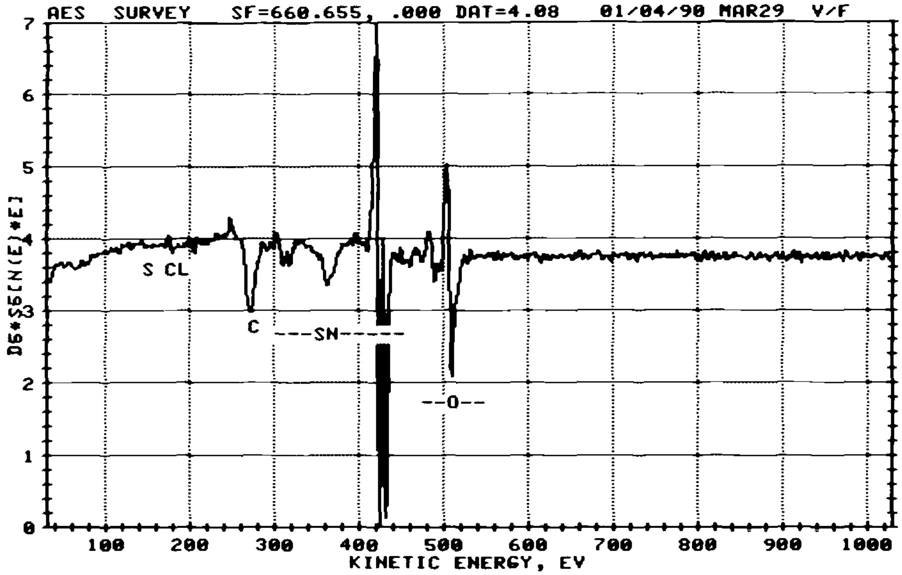

FIG. 2—*A typical AES differentiated spectrum of a tin surface which had been exposed in the FMGCC for seven days. The surface contaminants are only in the uppermost 5 nm.*

oxygen (O) and carbon (C) decreased to <50 at% and the Sn signal increased to >50 at% in less than 30 s of sputtering. These results are typical of both the housed, exposed samples and the unhoused, exposed samples.

Unhoused, exposed electroplated Au surfaces on DIP lead frames were sputter etched for over 120 min with no decrease in the Cu signal. Figure 3 is a survey spectrum of the sputtered area after 120 min of bombardment and shows mostly Cu with lesser amounts of sulfur (S), chlorine (Cl), C, and O; the strong Au peak at 69 eV is not visible. This corresponds to an equivalent thickness of SiO_2 of > 1600 nm. Unexposed and exposed, but housed, electroplated Au lead frames both show a trace of Cu, which is only present in less than the top 20 nm of the surface. The AES survey shown in Fig. 4 was recorded after 4 min of sputtering; only Au is seen.

A full connector contact is shown in Fig. 5; the photo was taken using a scanning electron microscope after exposure and testing, removal from the polymer housing, and unfolding of the formed contact. On the fully exposed circuit boards, heavy corrosion occurred on the leading edge of the contacts at the open end (Areas A in Fig. 5), i.e., opposite the end where it was soldered to the circuit board. Areas A contain exposed Cu alloy from the stamping operation during manufacture. Areas B are primarily Ni plated and Areas C are primarily Au plated. Visible edges D are also exposed Cu from the stamping operation, but no significant corrosion is seen. The particles seen in Areas C are primarily Sn, which is also the surface material of the left-hand edge of the contact and the section where it is soldered to the circuit board. Energy dispersive X-ray analysis of the corroded edge, which was at the opening of the assembled contact and was exposed after the stamping operation, showed Cu, Cl, O, and S. No significant corrosion was observed in the Au contact region, nor was there any significant corrosion along the Cu alloy edge parallel to the contact edge, which was also exposed after the stamping operation.

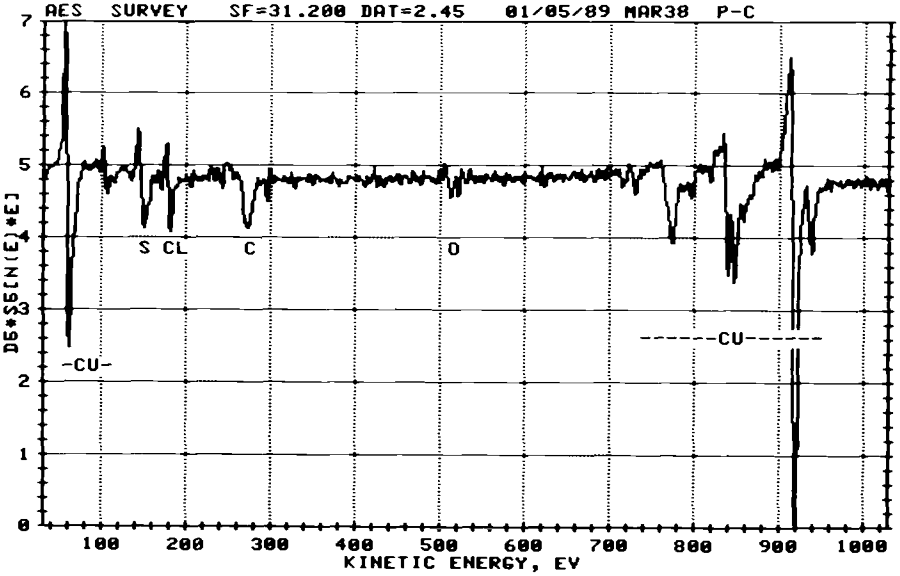

FIG. 3—*A survey spectrum of an unhoused, exposed plated Au surface after 120 min of sputtering. The large low energy peak is the 60-eV Cu peak and not the 69-eV Au peak.*

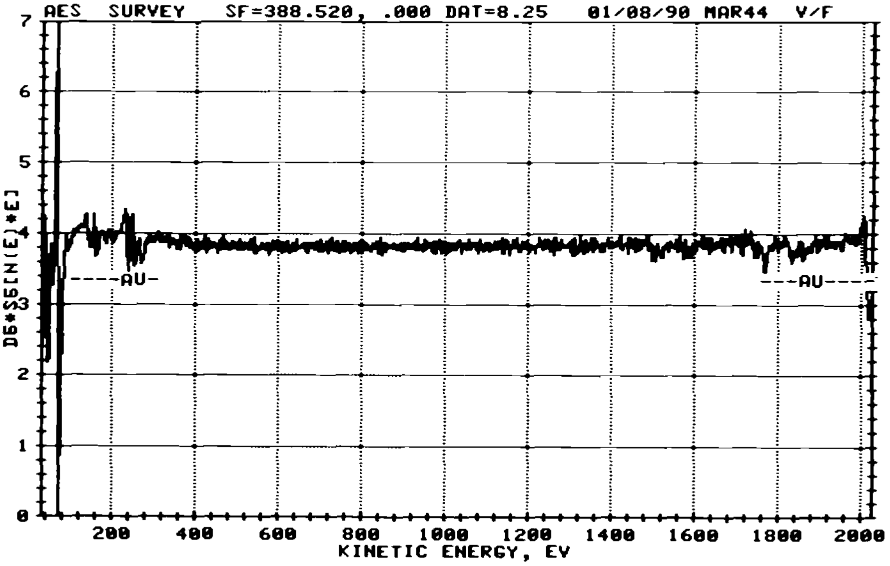

FIG. 4—*An AES survey spectrum of an exposed, but housed plated Au surface.*

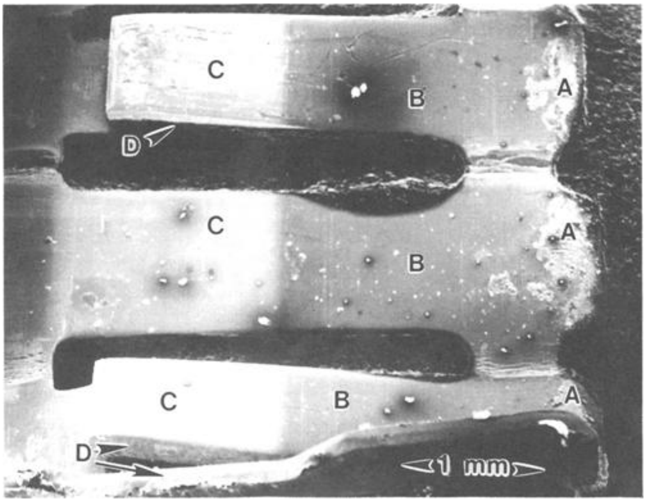

FIG. 5—*A photo of an unfolded view of a typical contact used on the circuit boards.*

Discussion

There are several reasons for the excellent survivability of the complete system to the harsh environmental tests to which it was subjected. These include the housing, system materials, a limited number of separable connections, and connection design.

From the visual and AES results, it is obvious that the telephone housing acts as an excellent shroud. This occurs for two reasons. The low air-exchange rate caused by limited openings is the primary reason. The second reason is the potential sacrificial nature of the carbon steel from which the housing is made. This surface can adsorb and react with most pollutants as they enter the housing, thereby lowering the concentration before the pollutants can reach the electronic components.

The two primary exposed electronic system materials, tin and plastic, are both relatively inert to the types of pollutants used in the tests. The AES results shown in Fig. 2 for Sn verify that Sn does not readily continue to corrode after the first few nanometers of oxide have formed on the surface.

Gold-plated surfaces were only exposed to the atmosphere in two places on the circuit boards. The unhoused, exposed, plated Au DIP lead frame was very corroded because of galvanic corrosion of the underlying Cu substrate at pores in the Au plating. However, this package was soldered into the circuit board, and the Au surface did not participate in the electrical performance of the circuit. The second Au surface was in the connector and is discussed below.

The copper alloy substrate in the connectors becomes exposed after the stamping and forming operation when the contact is manufactured. If this copper was exposed to the street atmosphere, a significant corrosion problem could exist. However, the shrouding effect of the assembled contact limits the amount of pollutant reaching the contact area, and the reactive nature of the copper tends to trap the diffusing pollutant at the entrance to the contact well. These two effects reduce the impact of pollutants in the actual contact region, as is shown by the following model. Consider a three-dimensional channel closed at one end and whose dimensions are x depth, y width, and z height, as illustrated in Fig. 6. Assume that the x-y plane surfaces are made of copper and that $y_0 \ll z_0$. Then for the copper surface to corrode

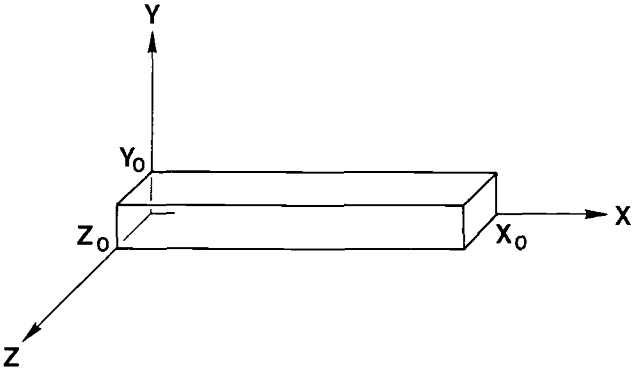

FIG. 6—*Schematic illustration of a corrosion channel:* $Y_0 \ll Z_0$.

down the length of the channel, the pollutant gas must diffuse past the copper at the open end of the channel. The time for the corrosion to proceed down the channel and accumulate on the walls to a thickness of M g/cm^2 is approximated by[5]

$$t = \left(\frac{2M}{DC_0}\right)\frac{x^2}{z} \tag{1}$$

Let D, the diffusion constant, equal 0.2 cm^2/s; let C_0, the free air concentration of Cl_2, equal 20 ppb, which equals 5.6×10^{-11} g/cm^3; and let M, the mass density of the corrosion film, equal 10^{-4} g/cm^2. For the connector channel in this case, the approximate active depth is 0.47 cm and the approximate spacing between the pin and connector body (the channel in the example) is 0.019 cm. Thus the time needed to corrode the copper at the bottom of the channel to a 1-μm depth is 2.1×10^8 s or more than six years. Therefore, for the seven-day experiment described above, we only expect corrosion at the entrance to the channel and that is precisely what is observed. In the actual field case an equipment lifetime of much more than six years is needed, but the Cl_2 concentration in the outdoor air is much less than 20 ppb (and still less inside of the housing). Therefore, based on the assumption that our test atmosphere reflects a substantially accelerated street atmosphere corrosiveness, we expect the apparatus to last substantially longer than six years.

Conclusions

We have demonstrated that an electronic coin telephone will operate normally after a seven-day exposure in a Battelle Class III atmosphere followed by exposure in a 95% RH atmosphere used for the electronic testing. In general, corrosion film thicknesses on Au plated or Cu circuit component surfaces were less than corrosion film thicknesses on control coupons. This is attributed to the circuit pack geometry and component shrouding. Specifically, we demonstrate that with reactive surfaces in a narrow channel, the corrosion film does not progress rapidly down the length of the channel. On Sn or nonmetallic surfaces, no significant corrosion was found as determined by AES and Ar$^+$ ion depth profiling.

[5] This derivation by R. Schubert and H. G. Tompkins (Motorola) will be published separately.

Acknowledgment

The authors thank Susan M. D'Egidio of Bellcore for the scanning electron microscopy work and W. A. Abbott of Battelle Laboratories for the exposure and cathodic reduction work.

References

[*1*] Abbott, W. H., "Effects of Industrial Air Pollutants on Electrical Contact Material," *IEEE Transactions on Parts, Hybrids, and Packaging,* PHP-10, Vol. 24, 1974.

[*2*] Rice, D. W., Suits, J. C., and Lewis, S. J., "Magnetic, Corrosion, and Surface Properties of Ni-Fe-Cr Thin Films," *Journal of Applied Physics,* Vol. 47, No. 3, March 1976, p. 1158.

[*3*] Rice, D. W., Peterson, P., Rigby, E. B., Phipps, P. B. P., Cappell, R. J., and Tremoureux, R. "Atmospheric Corrosion of Copper and Silver," *Journal of the Electrochemical Society,* Vol. 128, 1981, p. 275.

[*4*] International Electrotechnical Commission 68-2-11, Test Ka, 3rd ed., 1981, Geneva, Switzerland.

[*5*] International Electrotechnical Commission 68-2-42, Test Kc, 2nd ed., 1982, Geneva, Switzerland.

[*6*] International Electrotechnical Commission 68-2-30, Test Db, 2nd ed., 1980, Geneva, Switzerland.

[*7*] Abbott, W. H., "The Development and Performance Characteristics of Mixed Flowing Gas Test Environment," *IEEE Transactions on Components, Hybrids, and Manufacturing Technology,* CHMT-11, Vol. 11, No. 1, 1988, p. 22.

[*8*] "Generic Physical Design Requirements for Telecommunications Products and Equipment," Bellcore Technical Reference: TR-TSY-000078, Issue 2, Bellcore, Piscataway, NJ, December 1988.

[*9*] "Component Packaging and Interconnecting with Emphasis on Surface Mounting," ANSI/IPC-SM-780, Institute for Interconnecting and Packaging Electronic Circuits, New York, March 1988.

[*10*] "Functional Product Class Criteria—Telephones," Bell System Voice Communications Technical Reference Publication 48005, American Telephone and Telegraph Company, 1980.

Edward S. Sproles, Jr.[1]

Electrical Resistance of Wires Used as a Corrosion Rate Monitor

---

REFERENCE: Sproles, E. S., Jr., **"Electrical Resistance of Wires Used as a Corrosion Rate Monitor,"** *Corrosion of Electronic and Magnetic Materials, ASTM STP 1148,* P. J. Peterson, Ed., American Society for Testing and Materials, Philadelphia, 1992, pp. 11–20.

ABSTRACT: As a wire corrodes, its electrical resistance increases due to a loss of metallic cross-sectional area. By continuously monitoring resistance, corrosion can be monitored in the ambient where the wire is exposed. Although simple in principle, this technique has a number of practical problems when applied to atmospheric corrosion tests used with electronic equipment. These problems include: (1) the need to use very small diameter wires which are quite fragile; (2) the need to clean the wire in a reproducible and effective initialization process; and (3) the need to hold the wire in a resistance-measuring fixture without using solder and solder flux. This paper describes methods developed to overcome these problems and to implement the technique in a practical way for use as corrosion rate monitors for mixed gas atmospheric corrosion tests. Data are shown to illustrate the use of the method and to show the degree of reproducibility obtained between separate monitoring wires. The application of the method to fundamental studies of the effect of shielding on atmospheric corrosion is also illustrated.

KEY WORDS: copper, atmospheric corrosion, annealing, heat treatment

Laboratory atmospheric corrosion tests for electronic components require careful calibration and monitoring to obtain reproducible and meaningful test results on the components under test [*1–3*]. Ideally, a calibration and monitoring technique should be simple, accurate, and continuous to provide useful information promptly and efficiently. Change in resistance of metallic conductors has been used where the conductors are copper paths on printed circuit boards [*4*]. Such monitors are relatively easy to handle, but are readily available only with copper as the monitor material and require fabrication of appropriate test patterns on the test boards. Wires, however, are available in a wide range of materials and sizes. Wire is made in a continuous process; therefore, variations within the short lengths of wire required should be minimal.

In contrast, circuit boards are made in a batch process which may make them more susceptible to unit-to-unit variations. Furthermore, wires can be freely exposed to the ambient, while only one side of the sheet copper laminated to printed wiring boards can be exposed to the ambient; therefore, wires may show greater sensitivity to the ambient.

Wires have some obvious drawbacks as monitors. Fine wires are somewhat difficult to handle without breakage throughout the preparation and installation process; therefore, a robust fixture must be developed if the technique is to be practical for routine measurements. Connections to fine wires are also not easy. The fragility of the wire limits the options for screw terminations or other types of mechanical connections to the wire. Soldering is undesirable because it could: (1) introduce contamination from flux; (2) dissolve enough copper to reduce the wire cross section in the termination area; (3) set up an undesirable electrochemical couple.

[1] AT&T Bell Laboratories, Whippany Road, Whippany, NJ 07981.

As a result, for the method to be practical, the user must develop fixtures and techniques to connect the measurement wires to the resistance measurement instrumentation, preferably without solder and solder flux.

This paper discusses results of exploratory studies using wires as corrosion rate monitors and explains methods developed to overcome some of the problems in their application to this technique.

Development of Fixtures and Technique

One fixture to be developed is a measurement fixture in which wire can be exposed continuously to the test ambient while the resistance is monitored. Figure 1 shows the basic fixture developed to hold, expose, and monitor four wires. Each wire is freely exposed over the center portion of its length, approximately 50 mm. At each end of the wire, a cover presses the monitor wire against two measuring, or sensing, leads. These leads, made of gold wire, provided the four-wire connection to the monitor wire for precision resistance measurements. Silicone rubber pads backed up by a rigid plastic cover attached by screws provide the pressure.

Another fixture developed is the cleaning fixture. This fixture is made entirely of polymethylmethacrylate (PMMA) plastic and nylon screws. The fixture holds wires at the correct spacings to be later transferred to the measurement fixture with a minimum of disturbance and freely exposes the portion of the wire which will later be placed in the measurement fixture. The test wire is threaded onto the fixture and immersed in a series of liquid baths to bring the wire to an initial state of cleanliness. Figure 2 illustrates a cleaning fixture with wire installed in preparation for cleaning and transfer to the measurement fixture. Appropriate mechanical fixtures are provided so that the cleaning fixture and the measurement fixture can be fastened together without damage to wire already in place in the cleaning fixture. Figure 3 illustrates how the two fixtures are positioned in preparation for transfer of wire from the cleaning to the measurement fixture.

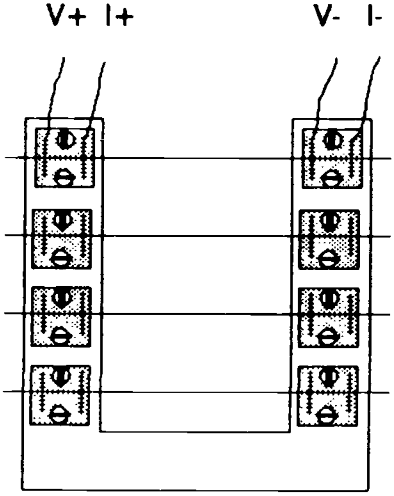

FIG. 1—*Wire-holding and measurement fixture.*

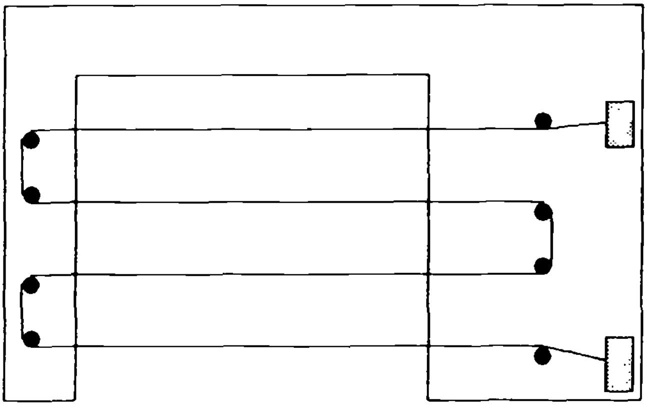

FIG. 2—*Wire-cleaning fixture loaded with wire.*

Instrumentation

Measurement instrumentation is fairly straightforward, which is one of the advantages of this technique. Figure 4 shows schematically the arrangement used to monitor the resistance of the wires. As shown in the figure, the leads from each wire are attached to a four-wire scanner, and the scanner leads are connected to a four-wire resistance meter. A computer periodically actuates the scanner and records the resistances measured by the meter. In this study of an aggressive test operating at a constant temperature, temperature compensation was not necessary because the resistance changes were relatively large. If these conditions are not applicable, it would be appropriate to include temperature measurement instrumentation and recording as part of the instrumentation. Alternatively, one might include a standard copper wire protected from the corrosive environment and measure its resistance with the same circuitry used for the test wires.

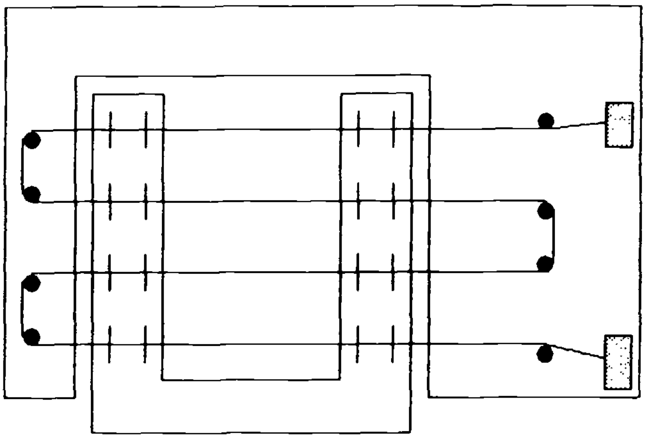

FIG. 3—*Wire-cleaning fixture and wire-measurement fixture prepared for wire transfer.*

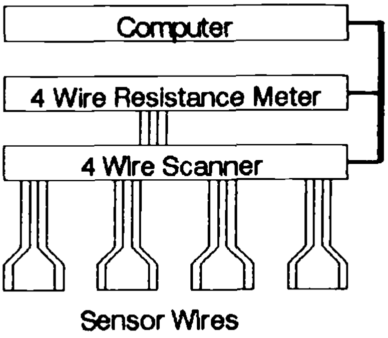

FIG. 4—*Block diagram of measurement electronics.*

Application of Technique

Selection of Wire

Copper wire is commercially available in sizes as small as AWG 55, which is nominally about 0.015 mm (0.00057 in.) in diameter. For this study, small lots of uninsulated No. 55 and No. 45 copper wire were purchased from a vendor of magnet wire (No. 45 wire has a nominal diameter of 0.046 mm). Reported corrosion film thicknesses on copper coupons in mixed gas corrosion tests are of the order of hundreds of nanometers; therefore, changes in wire resistance for small wires should be detectable. Experience quickly showed that No. 55 wire corrodes away too quickly (a few hours) to serve as a useful monitor in this type of test ambient. As a result, No. 45 wire was used for most of the studies.

Preparation Method

Prior to the start of a test, the wire must be cleaned and loaded onto the measurement fixture. The technique developed included the following steps:

1. Load wire onto cleaning fixture and secure ends with tape in the area that will not be immersed in liquid.
2. Clean wire through a series of liquid baths.
3. Attach measurement fixture to cleaning fixture.
4. Secure pressure pads on measurement fixture.
5. Cut wire on cleaning fixture.
6. Separate cleaning fixture from measurement fixture.
7. Install measurement fixture in test chamber.

Loading fine wire into the cleaning fixture without overstress or excessive slack can be difficult. The author found that the following procedures worked well. Attach one end of the wire with tape to the handle end of the fixture and attach a small weight with tape to the other end of the wire. Hold the fixture in an open area allowing the weighted end to hang freely, then manipulate the fixture to thread the wire between the appropriate pins or screws in the cleaning fixture. After the last leg is threaded, manipulate the fixture to bring the wire back toward the handle and tape the free end to the handle. The weight applies a constant load to the wire, pulling it tight enough to be straight but not applying so much load that it breaks.

Aggressive mechanical or chemical cleaning of fine wire is to be avoided because the wire could be broken, damaged, or chemically attacked through a significant fraction of its diameter. As a result, it is recommended that a stock of clean wire be obtained and stored carefully to protect it from receiving additional contamination. Fortunately, because wire is made in a continuous process, one spool contains enough material to last indefinitely in the test monitoring application.

Assuming that the wire has only light oxide and organic contamination films on its surface, cleaning to a reproducible initial state is fairly straightforward. In this study, the operator dipped the sample in the following sequence of liquid baths (immersion time 15 to 20 s in each bath):

1. Boiling 1,1,1 trichloroethane.
2. A 1:1 solution of concentrated HCl and water.
3. Deionized (DI) water.
4. Boiling DI water.

At the end of this sequence the wire showed a uniformly bright copper color.

Test Exposure

The measurement fixture holding the cleaned wires was mounted in a mixed gas test chamber. The chamber ambient conditions had previously been set to 10 ppb hydrogen sulfide (H_2S), 10 ppb chlorine (Cl_2), 200 ppb nitrogen dioxide (NO_2) at 70% RH and 25°C. Figure 5 shows the measured resistance of each of the wires plotted against exposure time. Each wire shows a similar increase in resistance with time over the first portion of the exposure. Later in the exposure there is some divergence, especially in the period shortly before the wire breaks. Figure 6 shows the data for the same wires plotted as the ratio of resistance to the initial resistance of the wire, giving a direct measure of the reproducibility of the technique.

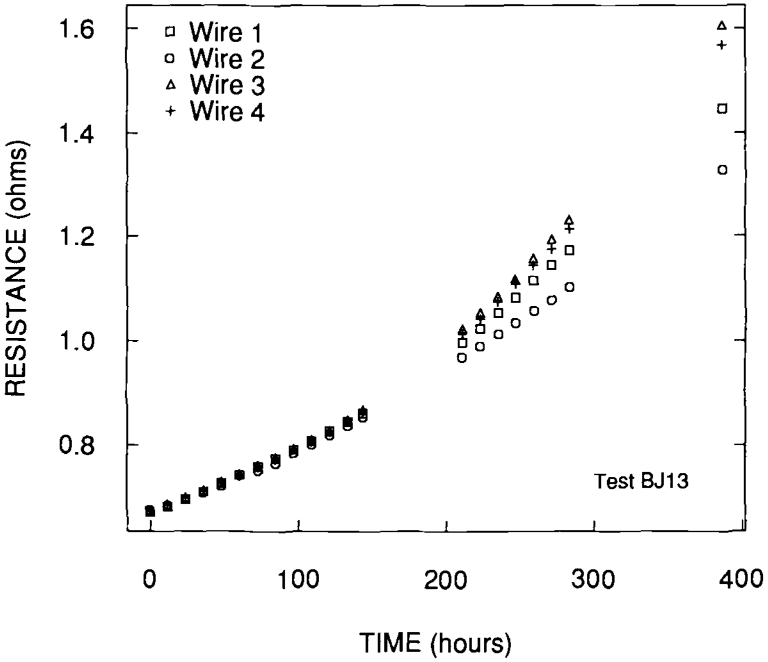

FIG. 5—*Resistance versus time of No. 45 copper wire freely exposed to corrosive ambient.*

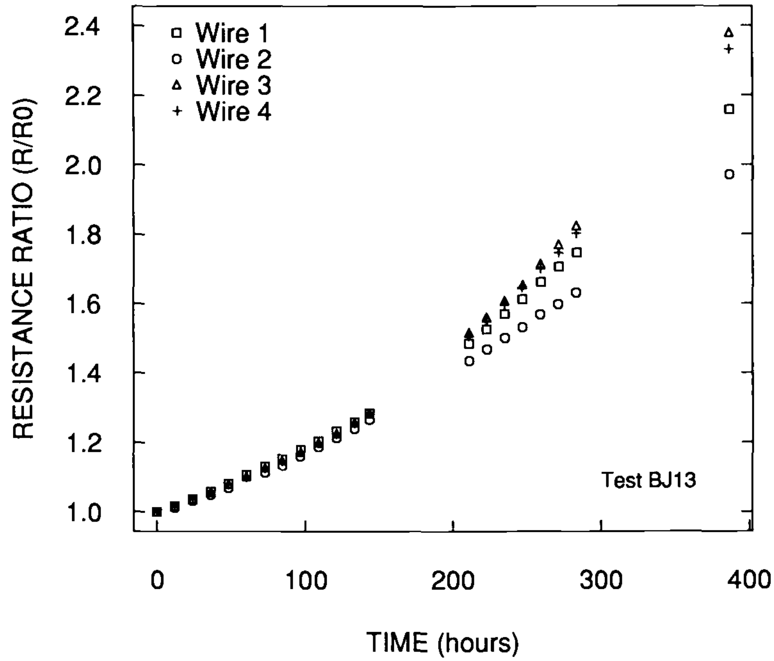

FIG. 6—*Resistance ratio versus time of No. 45 copper wire.*

Data Analysis

The results in Fig. 5 clearly show a nonlinear characteristic shape. Test conditions were nominally the same throughout the wire exposure, and independent measurements of reaction rate using a quartz crystal oscillator confirm constant conditions. Figure 7 shows the behavior of a silver-coated quartz crystal exposed to the same ambient. The quartz crystal technique has been described elsewhere [5–7]. This observation of constant reaction rate in the chamber suggests a different explanation for the nonlinear change in resistance. One plausible model is a constant film growth rate which, on a wire sample, translates into a constant decrease in wire radius with time. Since wire resistance is inversely related to wire cross-sectional area, a relation between resistance and time can be predicted. Specifically, it can be shown that if this model is valid, the relation between resistance, R, and time, t, should follow the form $1/\sqrt{R} = at + b$ where a and b are constants. Figure 8 shows a plot of $1/\sqrt{R}$ versus t. Since the plot is practically linear, the results of this experiment support the model of constant film growth rate.

Effect of Microstructure

As mentioned earlier, most of the studies were performed with No. 45 copper wire. The wire manufacturer makes such wire by cold drawing through a die, an operation that introduces cold work into the copper. Most of our studies were performed with such "hard drawn" wire, but we also investigated the effect of changing the microstructure by thermal treatment. A small quantity of the No. 45 wire was annealed in an inert atmosphere, then prepared for exposure according to the same procedure described earlier. Figure 9 shows the results of exposing the two batches of wire to an ambient of 90 ppb of Cl_2 in air at 25°C and 70% RH. The results

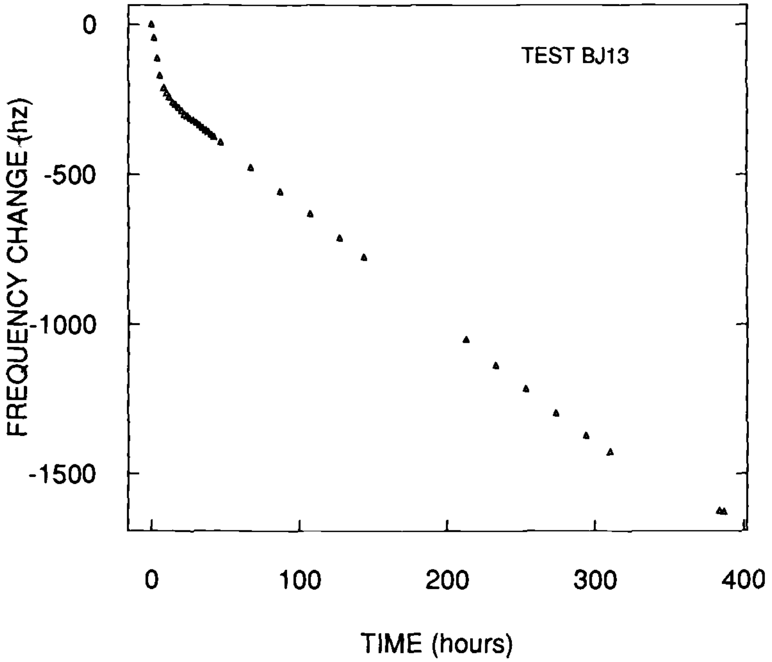

FIG. 7—*Frequency change versus time of silver-coated 5-MHz quartz crystal.*

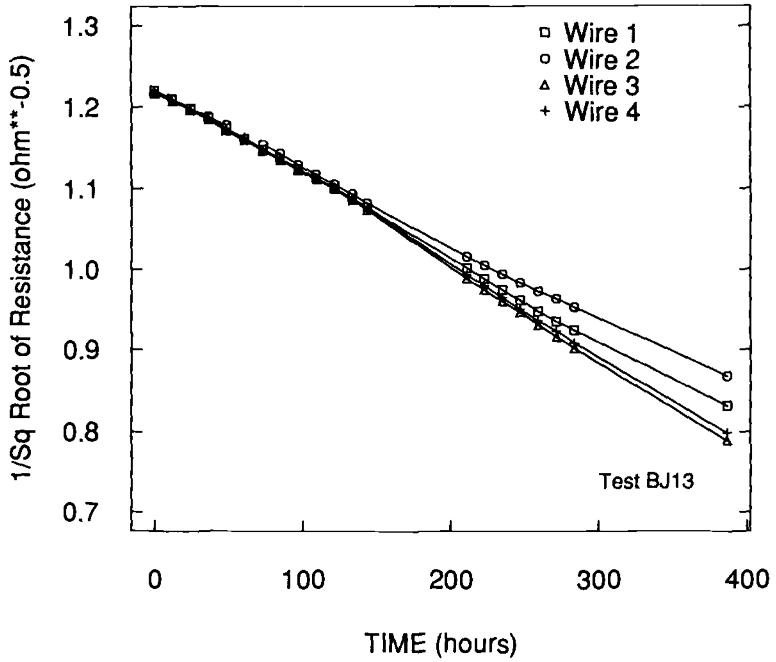

FIG. 8—*1/square root of resistance versus time (No. 45 copper wire).*

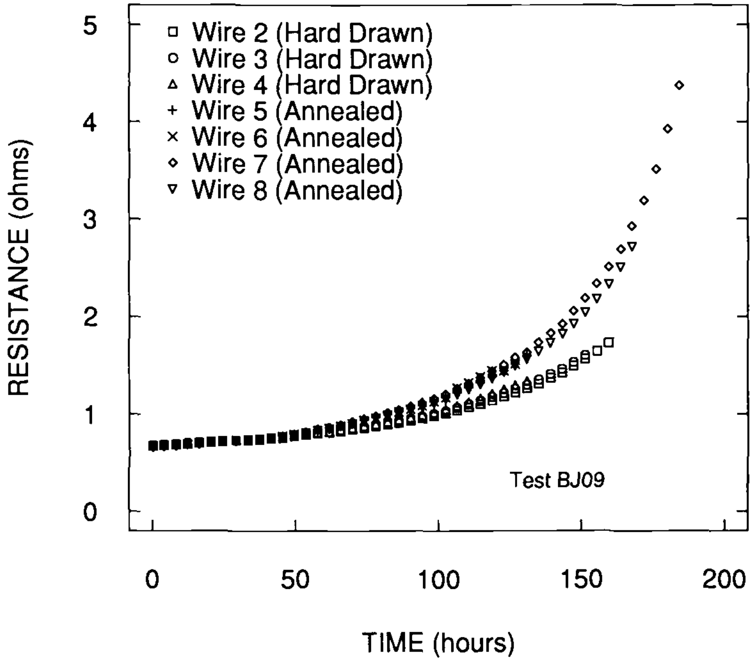

FIG. 9—*Resistance versus time of No. 45 copper wire.*

in Fig. 9 show that, upon exposure, such annealed wires increase in resistance at a higher rate than the hard-drawn wire. Also, such wires generally survived to a higher absolute resistance before going to an open circuit condition than the hard-drawn wire. The time to failure in this experiment was similar for the two wire conditions. We concluded that such annealed wires offered no particular advantage over hard-drawn wires as monitor devices, and since they require an extra preparation step, we abandoned their use.

The cause of the difference in resistance change behavior between the two wire treatments was explored. Both types of wire were etched and examined in a scanning electron microscope. The annealed wire showed distinct grain boundaries, while the hard drawn wire did not. Grain boundaries show up after etching because the etchant attacks them at a higher rate than the surrounding material. In an atmospheric corrosion test, the grain boundaries may also corrode at a faster rate than the surrounding material, showing behavior similar to that in the etching treatment. If the annealed wire is attacked in a more localized manner than the cold drawn wire, the resistance change behavior may be different. The more localized attack of the annealed wire may raise the resistance more rapidly if the corrosion progresses more rapidly toward the center of the wire than in the more uniform attack in the hard-drawn wire.

Application to Fundamental Studies

Many connector designs rely upon the effect of "shielding" or "shrouding" to reduce atmospheric corrosion of metallic parts. These terms refer to the phenomenon where access of the ambient to a metal surface is limited by other parts of the connector structure such as the insulator body. Wire resistance monitors offer a way to improve the understanding of the shielding phenomenon. Figure 10 shows schematically the cross section of a fixture designed to study quantitatively effects of geometry on shielding. The spacing between a wire and the fixture wall, as well as the size of the opening, may be varied to quantify the effects of each parameter.

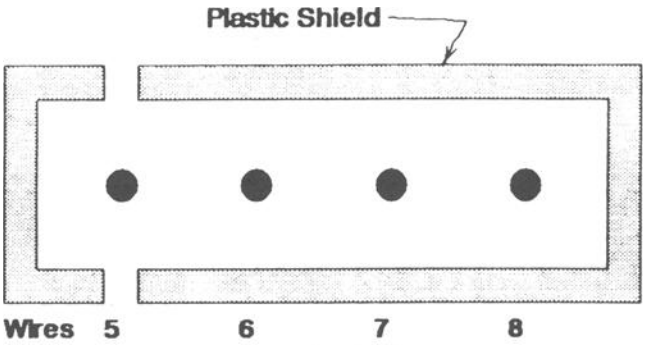

FIG. 10—*Test fixture for shielding experiment.*

Figure 11 shows the results of exposure of wires in such a fixture as compared with free exposure of wires to an ambient of 140 ppb Cl_2 at 25°C and 70% RH. The freely exposed wires (Wires 2 and 3) corrode at a much greater rate than the wires in the shielding fixture (Wires 5, 6, and 8), and the wires closer to the opening in the fixture corrode faster than those further from the opening.

Suggestions for Further Work

A number of wires showed immeasurably high resistance on the initial measurement. In general, these wires had broken at the pressure contact to the sensing wires under the rubber

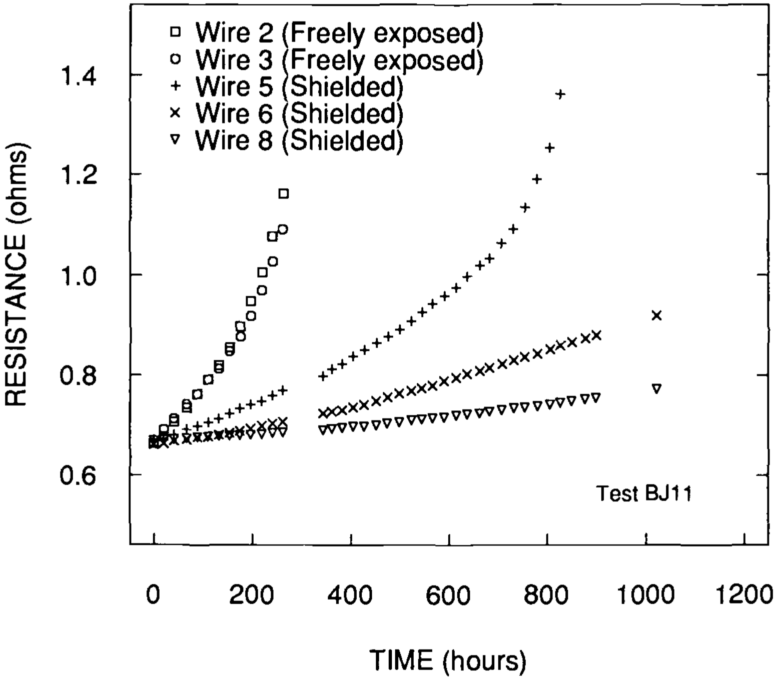

FIG. 11—*Resistance versus time of No. 45 copper wire freely exposed to or partially shielded from ambient.*

pads. The monitor wire is severely stressed at these points as it is forced to conform around the sense wire. An improved holding fixture would reduce these sharp bends and presumably decrease the chance of wire breakage. Flat contacts made by a suitable metallization technique are a possible approach. A holding fixture fabricated from a patterned printed circuit board where circuit paths replace the sensing wires is an alternate design that offers some additional advantages in simplification, flexibility, and reliability.

Conclusions

1. Fine wire monitors are effective devices for measuring the corrosion rate in mixed gas atmospheric corrosion tests.
2. Appropriate fixture design makes fine wire monitors usable on a routine basis.
3. Microstructure influences the resistance change behavior of copper wire in an atmospheric corrosion test.
4. Fine wire monitors are well suited to fundamental studies of phenomena such as the effect of shielding on corrosion rate.

Acknowledgment

The author gratefully acknowledges the assistance of M. Drozdowicz in this work.

References

[*1*] Schubert, R., "A Second Generation Accelerated Atmospheric Corrosion Chamber," *Degradation of Metals in the Atmosphere, ASTM STP 965*, 1988, p. 374.

[*2*] Gore, R., Witska, R., Kirby, J., and Chao, J., "Corrosive Gas Environmental Testing for Electric Contacts," *Proceedings*, 1989 IEEE Holm Conference on Electrical Contacts, Institute of Electrical and Electronic Engineers, 1989, p. 123.

[*3*] Abbott, W. H., *IEEE Transactions, Components, Hybrids, and Manufacturing Technology*, Vol. 11, 1988, p. 22.

[*4*] Allen R. C. and Trzeciak, M. J., "Measuring Environmental Corrosivity," *Proceedings*, 25th Holm Conference, Illinois Institute of Technology, Chicago, 1979, p. 29.

[*5*] Stockbridge, C. D., *Vacuum Microbalance Techniques*, K. Behrndt, Ed., Plenum Press, New York, Vol. 5, p. 193.

[*6*] Thomas, J. H. and Sharma, S. P., *Journal of Vacuum Science and Technology*, Vol. 13, 1976, p. 549.

[*7*] *Applications of Piezoelectric Quartz Crystal Microbalances*, C. Lu and A. W. Czandema, Eds., Elsevier, New York, 1984.

Sandeep K. Chawla,[2] Bretton I. Rickett,[1] and Joe H. Payer[1]

Formation of Copper Sulfide in Moist Air-Sulfur Dioxide

REFERENCE: Chawla, S. K., Rickett, B. I., and Payer, J. H., **"Formation of Copper Sulfide in Moist Air-Sulfur Dioxide,"** *Corrosion of Electronic and Magnetic Materials, ASTM STP 1148,* P. J. Peterson, Ed., American Society for Testing and Materials, Philadelphia, 1992, pp. 21–35.

ABSTRACT: Films formed on copper exposed to various sulfur-bearing environments were analyzed by XPS and electrochemical reduction to study the formation of copper sulfide. The S-2p photoelectron band showed the presence of copper sulfide in the film in addition to oxysulfur species. Coulometric reduction analysis of the film suggested that the sulfide was nonstoichiometric. The formation of copper sulfide was also noted on copper immersed in "sulfurous" acid and in sulfuric acid. The properties of the sulfide that formed reductively on copper from these oxysulfur environments were compared with those of copper sulfide that formed from a moist hydrogen sulfide environment. Formation of copper sulfide from the oxysulfur environments showed that sulfur could participate as a reducible species in the film-forming corrosion reactions.

KEY WORDS: atmospheric corrosion, copper, sulfur dioxide, hydrogen sulfide, XPS, coulometric reduction, sulfide, thin film

Recent work by the authors has shown that copper sulfide is one of the products of the atmospheric corrosion of copper in moist air with sulfur dioxide [*1*]. The finding is quite significant because it proves that sulfur participates as a reducible species in the electrochemical process of copper corrosion in moist air. The sulfur is reduced from S(+IV) in SO_2 to S(−I, −II) in the sulfide. The objective of this paper is to examine and verify the formation of copper sulfide when copper corrodes in moist air with sulfur dioxide.

This work is part of a research program to increase the understanding of corrosion processes in thin films of electrolyte. In moist air, several monolayers of adsorbed water can form a thin electrolyte on surfaces. Electrochemical processes account for the corrosion and surface reactivity of metals and semiconductors under these conditions. Copper was selected as the initial metal for study because of the wealth of knowledge regarding copper's behavior in bulk electrolytes and its industrial importance in electronics. Sulfur dioxide was selected as the initial, single gas species for study because it is an important atmospheric pollutant. Further work involves additional corrosive gas species and mixtures of corrosive species. Our interest is in the early stages of surface reactivity and the growth of thin, tarnish films (less than 200 nm). The processes which control the development of tarnish films in thin layers of electrolyte are poorly understood and, hence, worthy of study.

There is prior evidence of sulfide formation within sulfur dioxide environments. Sydberger and Vannerberg [*2*] exposed Cu to air with 100 ppm SO_2 + 98% relative humidity (RH) for

---

[1] Graduate student and professor, respectively, Department of Materials Science and Engineering, Case Western Reserve University, Cleveland, OH 44106.

[2] Research scientist, Tata Energy Research Institute, New Delhi, India.

3 h and found that the predominant crystalline phase in the corrosion product was hydrated copper sulfate, with significant amounts of sulfite and sulfide. McLeod and Rogers [*3,4*] exposed low carbon steel (a) to moist air containing 0.7 to 2.2% SO_2 and (b) to deaerated solutions of sulfurous acid (H_2SO_3). Using X-ray diffraction (XRD), oxygen-containing compounds Fe_3O_4, α-FeO·OH, and ferrous sulfate were detected in the corrosion products of the former. The corrosion products formed on steel exposed to sulfurous acid solutions without air were shown to contain FeS and S (FeS was detected by chemical analysis). The solutions contained Fe^{2+}, S^{2-}, $S_2O_4^{2-}$, and $S_2O_3^{2-}$ ions after the exposures. The corrosion rates were high in these solutions and increased with increasing amounts of SO_2 in solution. Atomic hydrogen is a product of cathodic reductions in acids, and the hydrogen produced during reaction was proposed by McLeod and Rogers to encourage the step-wise reduction of SO_3^{2-} to S^{2-}. Ross and Callaghan [*5*] also detected the presence of sulfides and elemental sulfur in the corrosion products of mild steel exposed to an atmosphere containing 1 vol% SO_2 + 90% RH. Johansson and Vannerberg [*6*] found iron sulfide in the corrosion products of steel exposed to a gas containing 3% O_2, 12% CO_2, 10 ppm SO_2, bal. N_2 with 90% RH. XRD showed that the crystalline corrosion products were hydrated sulfates and sulfites. The FeS was found to be amorphous and could only be detected by wet chemical analysis and ESCA. Sydberger and Ericsson [*7*] also noted the formation of amorphous iron sulfide on mild steel exposed to air with a ppm level of SO_2 and high RH. ESCA indicated that the outer layer of the corrosion product had sulfate, whereas the inner layers consisted of iron sulfite and sulfide.

Methods to Detect Copper Sulfide

Two principal techniques were used to detect the presence of copper sulfides in corrosion films: X-ray photoelectron spectroscopy (XPS or ESCA) and coulometric reduction. These techniques are briefly described below. The specimens utilized in this study were cut from a sheet of oxygen-free, high-conductivity (OFHC) copper (99.99+% Cu from Metal Samples Inc.) into rectangular coupons 30 by 15 by 0.6 mm.

X-Ray Photoelectron Spectroscopy

XPS is a valuable tool for studying the surface chemistry of corrosion films. It is especially suited to the detection of different sulfur species because the binding energy of sulfur core photoelectrons (S-2p) is sensitive to the oxidation state of sulfur in surface layers. In conjunction with ion sputtering, XPS can provide chemical information as a function of depth from the surface (depth profiling).

In order to determine the nature of sulfur in the corrosion films formed on copper after exposure to various sulfur-bearing environments, the XPS spectral features of the S-2p band (strongest photoline) from sulfur in different oxidation states were based upon analytical standards. Commercially available, reagent grade powders of the following compounds were examined: copper (I) sulfide (Cu_2S), copper (II) sulfide (CuS), sodium thiosulfate ($Na_2S_2O_3$), sodium dithionite ($Na_2S_2O_4$), sodium bisulfite ($NaHSO_3$), and copper (II) sulfate ($CuSO_4$). This set of materials encompassed a broad range of sulfur oxidation states ranging from +VI to −II.

XPS was performed using a PHI 5400 ESCA system (Perkin Elmer Corp.). Unmonochromatized Mg-K_α radiation [at characteristic energy: 1253.6 eV and full width half maximum (FWHM): 0.7 eV] was used for the analyses. The anode of the X-ray source was operated at a total power dissipation of 400 W (15 kV, 26.7 mA). Spectral analysis was done with a spherical capacitor analyzer (SCA) connected to a channeltron electron multiplier and single channel detector. The spectrometer was calibrated for two standards, viz. Cu-$2p_{3/2}$ at 932.6 eV binding energy (BE) and Au-$4f_{7/2}$ at 84.0 eV BE. Static charge referencing was done with respect to the C-$1s_{1/2}$ peak (from adventitious surface hydrocarbon), assumed to be at 284.7 eV BE in all cases.

The summary of the XPS standardization data for the O-$1s_{1/2}$ and S-2p peaks is presented in Table 1. The S-2p photopeaks from the anion ligands are shown in the Fig. 1 montage. All S-2p peaks displayed an asymmetry on the high-BE side as a result of being unresolved spin-orbit doublets. It was observed that in the ligands where S was coordinated to O (S-O coordination, oxysulfur anions), the S-2p photopeak occurred at BE $>$ 166 eV (see Fig. 1 for coordination). In contrast, for ligands without O (S-S coordination, sulfide homologues), the S-2p photopeak occurred at BE $<$ 163 eV. Therefore, the distinction between the initial state of sulfur in SO_2 and the final state of sulfur in sulfides in the corrosion films can be made quite readily on the basis of the S-2p centroid BE. Copper sulfides are prone to reaction with air at room temperature, and the small high-BE peak in the spectrum of Cu_2S arises from reaction with air at the sample surface [*8*]. The result is that S-O coordinations from oxidation of sulfide are observed at the surface in contact with air.

The distinction between Cu_2S and CuS by XPS is difficult [*9*]. As the Cu-2p photoelectron band exhibits characteristic shake-up satellites on the high-BE side of the $2p_{1/2,3/2}$ doublet for Cu^{2+} ($3d^9$) species, cupric compounds may be readily distinguished from cuprous compounds and pure copper, both of which lack shake-up peaks [*9*]. Indeed, the ability to discriminate between CuO and Cu_2O in corrosion films relies upon this phenomenon. However, in the case of copper sulfides, CuS and Cu_2S, no shake-up satellites appear in the Cu-2p spectra because of electron orbital interactions [*9–11*].

For covellite, CuS, the d-type band lies at low enough energy to allow the transfer of electrons from the valence band created by sulfur to the localized copper d-orbital. This resultant change in charge for the copper and sulfur species contradicts intuitive sensibilities about the oxidation states of the elements [*12*]. Thus, the Cu^{2+} effectively reduces to Cu^{1+}, and the S^{-2} oxidizes to the S^{-1} state. Importantly, the absence of electrons from the upper energy levels of the nonlocalized, sulfur-dominated valence band permits electronic conduction (p-type) by holes. The bonding instability created by the presence of a large number of the holes encourages an interaction between the S^{-1} atoms to stabilize with S_2^{-2} structure [*12*].

Further support for the cuprous oxidation state in Cu_2S and CuS may be found in the magnetic response of these materials. Both compounds exhibit a net diamagnetic response as a result of filled $3d^{10}$ electron orbitals [*13*]. Indeed, a link between the occurrence of XPS shake-up satellites and paramagnetic behavior has been made as both phenomena result from unpaired electron spin [*11*]. Thus, CuS effectively contains Cu^{+1} and S^{-1}. The only distinguishing XPS spectral feature is a +0.7 eV shift in the S-2p centroid of CuS vis-a-vis Cu_2S (Table 1).

TABLE 1—*Summary of XPS binding energies determined from standard sulfur-bearing anion ligands.*

Material, anion	Oxidation State of S	O-$1s_{1/2}$	S-2p
Cu_2S (sulfide)	−II	. . .	161.8
CuS (sulfide)	−I	. . .	162.5
$Na_2S_2O_3$ (thiosulfate)	+II (−II, +VI)	531.4	161.8/167.9
$Na_2S_2O_4$ (dithionite)	+III	531.3	166.1/168.2
$NaHSO_3$ (bisulfite)	+IV	531.4	166.4/166.7
$CuSO_4$	+VI	531.9	168.8

NOTE: Analysis with Mg-K_α radiation (1253.6 eV).
All binding energy values in eV.
S-2p binding energies for centroid of doublet.

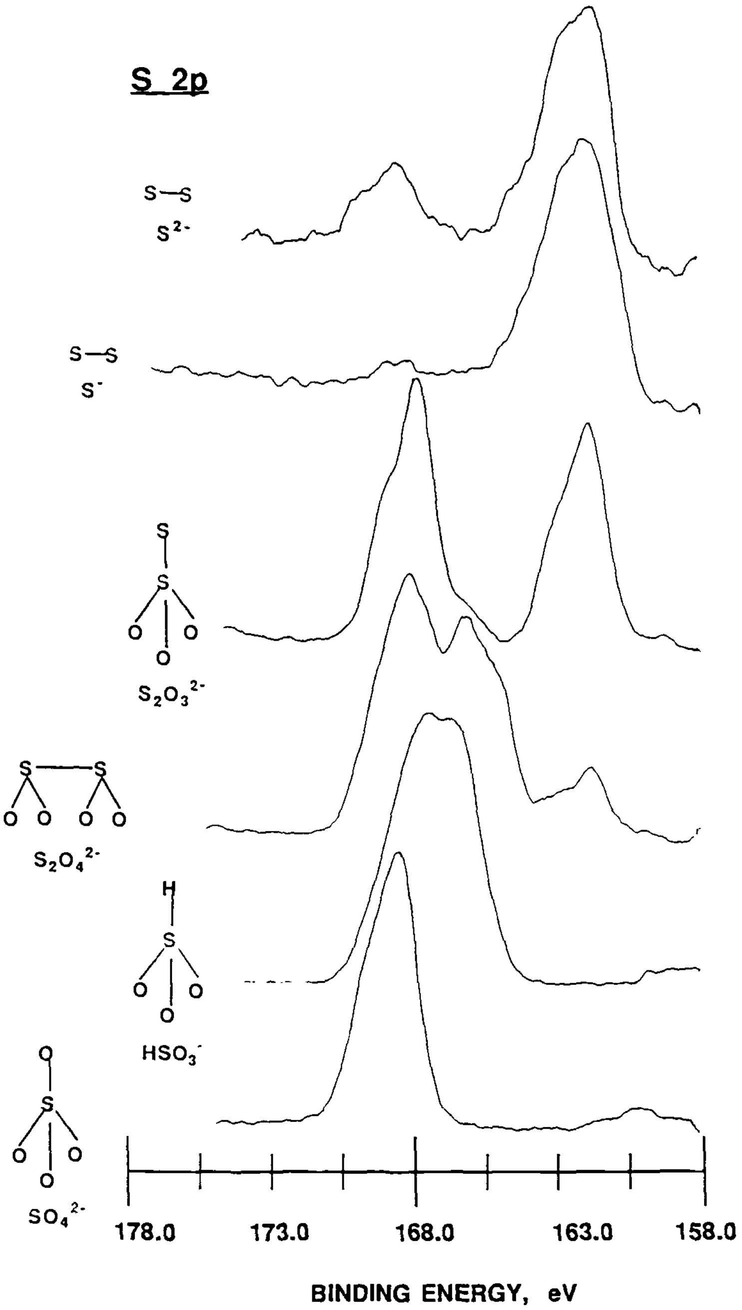

FIG. 1—*XPS multiplex montage of the S-2p band obtained from various standard sulfur-bearing anion ligands. The atomic coordination within the ligands is shown at the left of the spectra.*

In the case of thiosulfate, $S_2O_3^{2-}$, two asymmetric S-2p peaks (unresolved spin-orbit doublets) separated by 6.1 eV were observed. The high-BE peak originates from the core level of S in triangular coordination with O (called "central S"), whereas the low-BE peak originates from the core level of the second S atom (called "peripheral S"), which is coordinated to the central S [*14*]. Although the formal valence of S in $S_2O_3^{2-}$ is (+II), the actual oxidation state of S in the two types of coordination is different; that is, central S is (+VI) and peripheral S is (−II) with the average being (+II). The binding energy of the S-2p peak from the central S was indeed close to the energy of the S-2p peak from SO_4^{2-}, S(+VI). Likewise, the binding energy of the S-2p peak from the peripheral S was close to the measured energy of the S-2p peak from S^{2-}, S(−II).

The binding energies for the O-$1s_{1/2}$ photopeak ranged from 531.3 to 531.9 eV for the various oxysulfur anions. No major chemical shift in peak position or other spectral changes were noted for this photopeak in the different coordinations, and, as such, this peak did not have great diagnostic value.

Coulometric Reduction

Coulometric reduction analysis is also an important technique for studying surface films on metals. Both galvanostatic stripping (chronopotentiometry) as well as voltammetry may be used. Coulometric reduction is useful as it can give chemical as well as quantitative information about film constituents. Insoluble electroactive species present within the film are reduced at characteristic potentials, and the charge required to reduce them is related to their quantity in the film. The principles of coulometric reduction used for identifying corrosion products on metal surfaces have been discussed by Kruger [*15*].

Reduction potentials for copper oxides present in copper sulfide were determined by Vedel and Soubeyrand [*16*]. The composition of the tarnish film formed on copper exposed to humid air (100% RH at 25°C) containing 0.05 volumetric parts per million (ppmv) H_2S for 168 h was analyzed by Peide et al. [*17*] using coulometric reduction. The film was found to contain CuS, Cu_2S, Cu_2O, and CuO. Examination of the corroded surface by SEM revealed circular corrosion products ranging from 25 to 100 μm in size. Fiaud et al. [*18*] studied the corrosion products on copper exposed to moist air containing SO_2, H_2S, and SO_2 + H_2S using cathodic stripping voltammetry. Compounds identified in the films were Cu_2S, Cu_2O, CuO, and a mixed compound (CuO + Cu_2O). Hoar and Stockbridge [*19*] have shown that the reduction potentials for various compounds in tarnish film depend on the polarization characteristics of the film as well as the applied current density. Based on the above studies, the coulometric reduction potentials for oxides and sulfides of copper have been compiled in Table 2. The values are dependent on test conditions such as solution pH and reduction current density. Film thicknesses from reduction analysis can be computed using Faraday's law and electrochemical equivalents for the compounds as described by Allen [*20*].

Some preliminary coulometric reduction analyses were carried out on copper tarnish films formed by the exposure conditions detailed in later sections of this work. The coulometric reduction was performed in deaerated 0.1 *M* KCl solution with an applied cathodic current density of 0.05 mA/cm^2. Electrode potentials were recorded versus a saturated calomel electrode (SCE). Results are reported in given sections.

Formation of Sulfide Films on Copper

Films formed on copper exposed to various sulfur-bearing environments were analyzed by XPS and electrochemical reduction to study the formation of copper sulfide. Only XPS results

TABLE 2—*Electrochemical reduction potentials for copper oxides and sulfides reported in the literature.*

Source	Ref.	Test Conditions	Component	Potential, mV_{SCE}
Peide et al.	*17*	0.1 *M* Na_2CO_3, 100–500 $\mu A/cm^2$	CuO	−150
			Cu_2O	−650
			CuS	−800
			Cu_2S	−1070
Hoar and Stockbridge	*19*	0.2 *M* KCl, buffered 300 $\mu A/cm^2$	Cu_2S	−896 to −946
			H^+	−1038
Vedel and Soubeyrand	*16*	0.1 *M* sodium acetate	in Cu_2S	Versus Cu_2S/Cu
			CuO	+840
			Cu_2O	+550
			CuS	+300
			Cu_2S	0
			H_2O	−210
Zakipour	Private Communication		CuO	−200
			Cu_2O	−600
			CuS	−800
			Cu_2S	−1100

pertinent to the S-2p peak are presented here since this peak was the primary diagnostic focus. The results from four exposure conditions are detailed. First, short-term exposures were carried out in atmospheres containing moist SO_2. Two other exposures were carried out in (a) an aqueous environment of SO_2 dissolved in water and (b) in concentrated sulfuric acid. Finally, the results of these tests were compared with that of an exposure to moist H_2S.

Moist Air-Sulfur Dioxide Exposures

In an earlier paper results were presented for copper exposed to moist air containing a high SO_2 level and a low SO_2 level [*1*]. The high level exposure was carried out in a moist, stagnant environment with ≈0.5% SO_2. The tarnish film was analyzed by Auger electron spectroscopy and electron microscopy and was found to contain a mixture of copper (I) oxide and copper sulfide [*1*]. Additional results are presented here for trace level exposures which were performed in mixed flowing gas (MFG) chambers. The first set of experiments was carried out in an MFG system[3] similar in design to the system of Curren et al. [*21*]. Exposures were carried out for up to 60-h time periods in an atmosphere with 110 ppb SO_2 + 70% RH at 30°C. XPS analysis of a coupon exposed for 8 h showed that about 70% of the copper in the top layer was present in the univalent state, i.e. Cu^{1+}. The remaining copper was in the divalent state, i.e. Cu^{2+}. Oxygen was present within adsorbed species ($OH + OH_2$) and as lattice oxygen in Cu_2O. The S-2p band from the surface of this coupon is shown in Fig. 2. Sulfur appeared in two envelopes. The high-BE envelope was from S-O coordinated species, i.e. oxysulfur anions. Curve synthesis using the standard photopeak positions from Table 1 suggested that the dominant species was bisulfite with some dithionite and/or thiosulfate, and traces of sulfate. The low-BE envelope was from S-S coordinated species and corresponded to the peak positions for copper sulfide.

Coulometric reduction was performed on coupons exposed to the above trace SO_2 environment for 12 and 60 h. The reduction plots from these coupons are illustrated in Fig. 3a and

---

[3] At Digital Equipment Corp., Colorado Springs, CO.

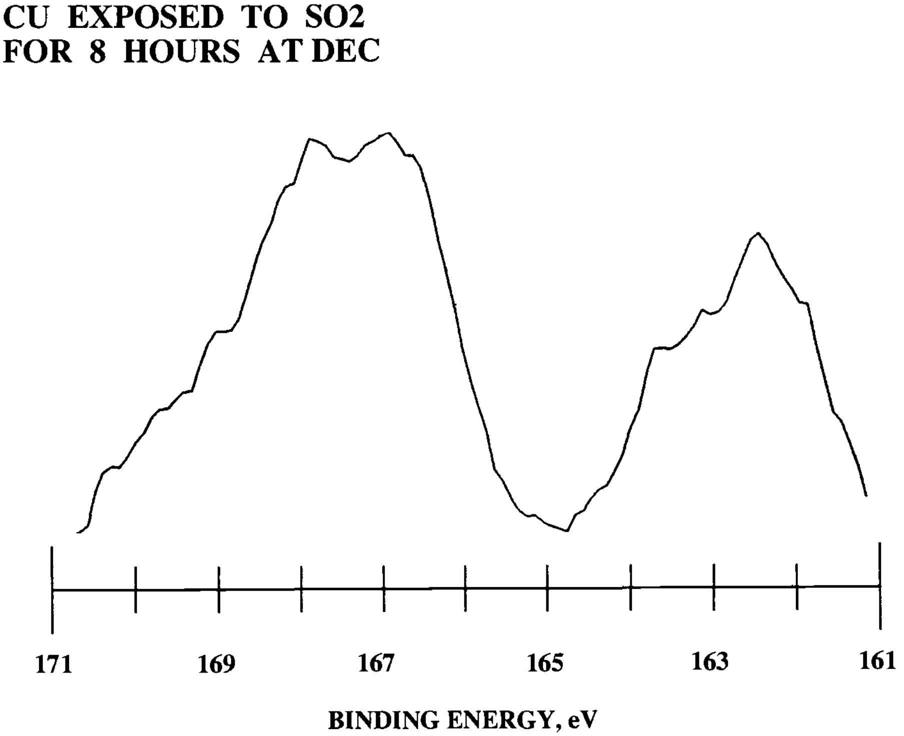

FIG. 2—*The S-2p band obtained by XPS analysis of copper exposed to air with 110 ppb SO_2 + 70% RH at 30°C for 8 h.*

3b, respectively. In both cases, three arrests in the potential were observed. The first arrest at about -550 mV_{SCE} corresponded to the reduction of Cu_2O in the film. The second arrest at about -840 mV_{SCE} was within the range of values reported for CuS and Cu_2S, possibly a nonstoichiometric Cu_2S (Table 2). The third arrest at about -1100 mV_{SCE} corresponded to H^+ ion reduction. The duration of the second arrest increased greatly with increased exposure time to the environment.

Another set of trace SO_2 exposures was carried out in a mixed flowing gas system[4] similar in design to that of Volpe and Peterson [*22*]. Copper coupons were exposed to air with about 100 ppb SO_2 + 60% RH at 23°C for 36 h. The S-2p band from XPS analysis of the coupon surface is shown in Fig. 4a. Only one S-2p envelope with a centroid at 167.0 eV was observed. This peak appeared to be from the anionic precursor of SO_2, viz. bisulfite or sulfite, with sulfur as S(+IV). However, after light sputtering of the surface with Ar^+ ions, the intensity of this envelope diminished and a low-BE envelope centered at 162.0 eV appeared in the S-2p multiplex spectrum. The S-2p bands, with vertical scales adjusted to show spectral detail, are shown in Fig. 4b and 4c for approximately 1 nm sputtering and 2 nm sputtering, respectively. These spectra were similar to those obtained for the trace level exposure described earlier (Fig. 2) and again showed the presence of copper sulfide in the inner layers of the film. These observations on copper were very similar to the ESCA results reported by Johansson and Vannerberg [*6*]

---

[4] At Case Western Reserve University, Cleveland, OH.

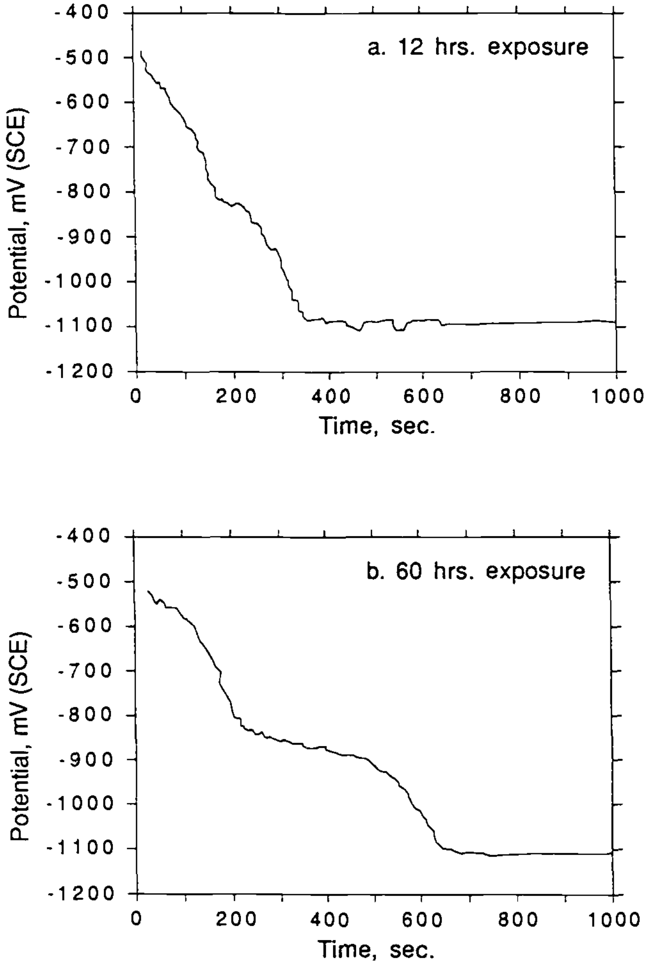

FIG. 3—*Potential-time plots obtained from electrochemical reduction analysis of copper exposed to air with 110 ppb* SO_2 + *70% RH at 30°C for* (a) *12 h and* (b) *60 h.*

and Sydberger and Ericsson [7] for low-carbon steel exposed to moist SO_2-containing atmospheres, i.e. sulfides were detected as products of the corrosion reactions for both copper and iron.

"Sulfurous" Acid and Sulfuric Acid Exposures

Two long-term immersion exposures of copper in environments containing oxysulfur acids were carried out. In the first exposure, a copper coupon was immersed in distilled water in a glass vial and pure SO_2 gas was bubbled through the water for 1 min forming "sulfurous" acid. The vial was then sealed for seven days. In the second exposure, a copper coupon was immersed in concentrated sulfuric acid (98% analytical reagent, 1.84 sp gr) and sealed in a glass vial for seven days. After seven days, black spots were observed on the copper coupon

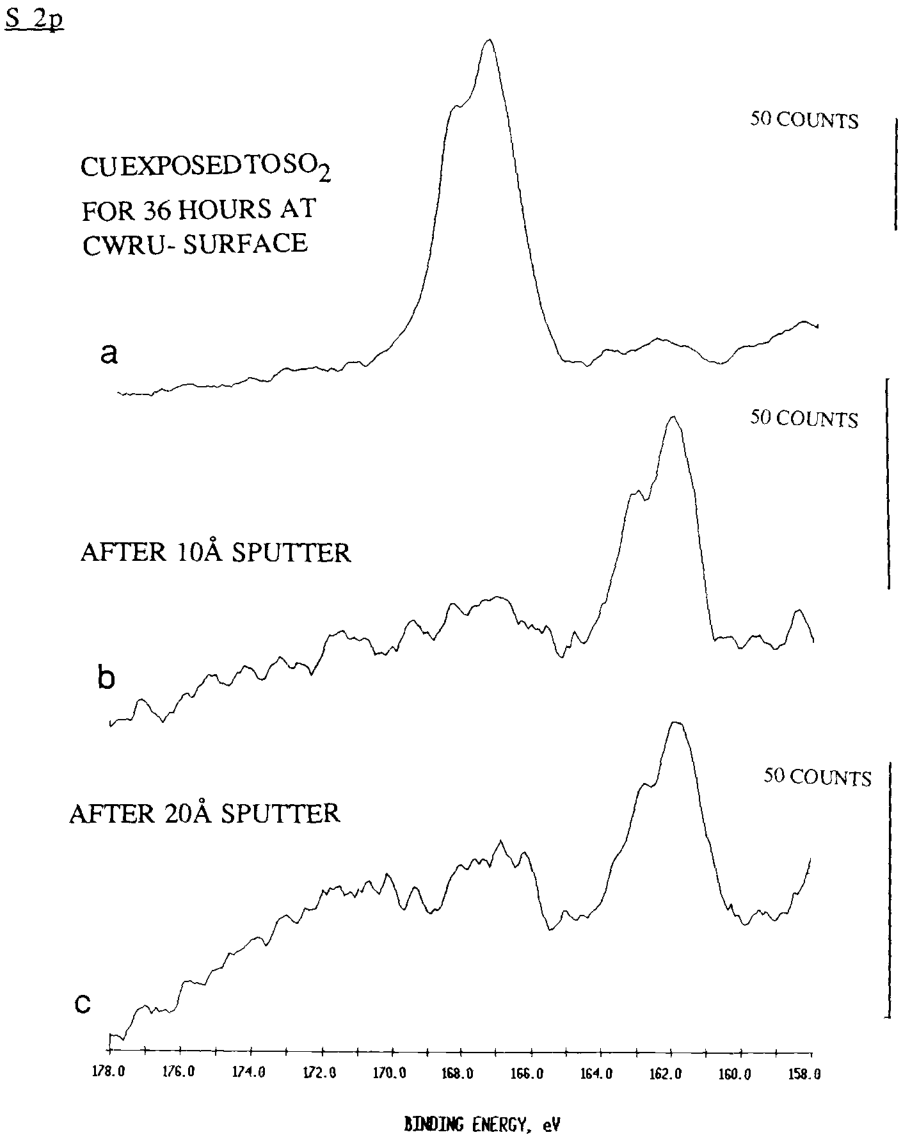

FIG. 4—*The S-2p band obtained by XPS analysis of copper exposed to air with 100 ppb* SO_2 *+ 60% RH at 23°C for 36 h:* (a) *before sputtering,* (b) *after ≈1 nm sputter, and* (c) *≈2 nm sputter.*

immersed in "sulfurous" acid, and a thick black crust was observed on the coupon immersed in sulfuric acid. The coupons were removed from solution, dried, and analyzed by XPS.

The S-2p photopeaks from the surface of the coupons exposed to "sulfurous" acid and sulfuric acid are shown in Fig. 5a and 5b, respectively. In both cases, the low-BE envelope of S-2p with a centroid at 162.0 eV was dominant, indicating the presence of copper sulfide. Additionally, no shake-up satellites were observed in the Cu-2p multiplex band of both films, which suggested that only univalent copper was present in the film.

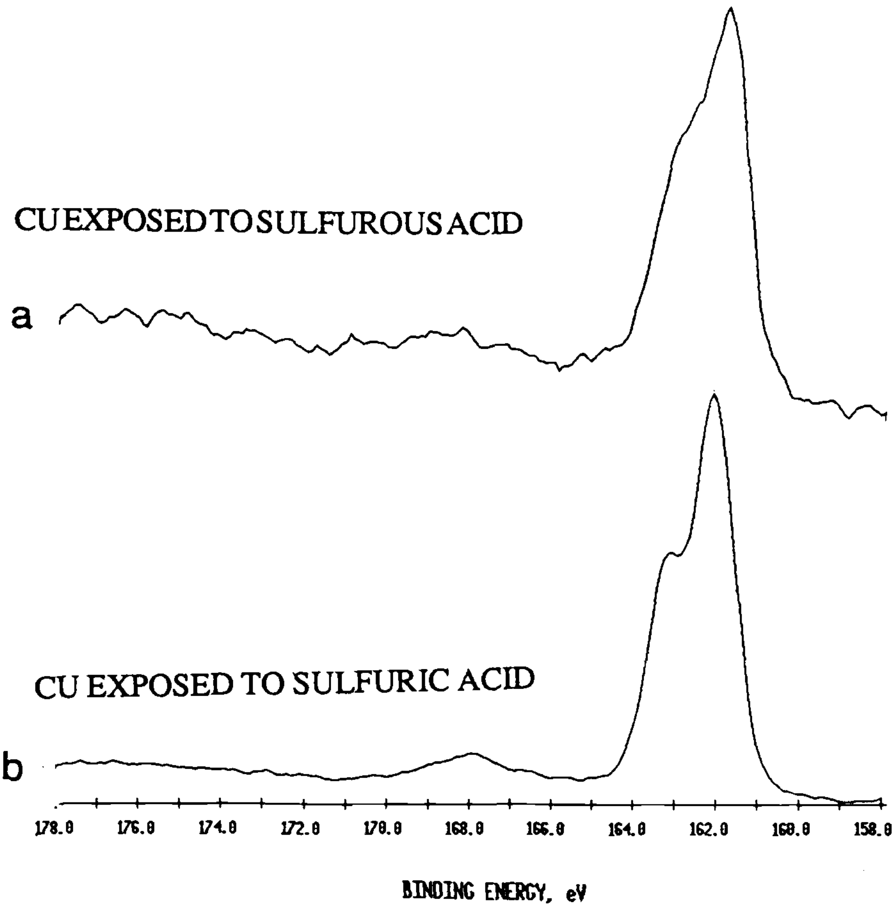

FIG. 5—*The S-2p band obtained by XPS analysis of copper after immersion for seven days in* (a) *"sulfurous" acid, and* (b) *concentrated sulfuric acid.*

Moist Hydrogen Sulfide Exposures

In order to compare the sulfide formed on copper from the oxysulfur environments (SO_2, H_2SO_3, H_2SO_4) with the sulfide formed in reduced sulfur environments, i.e., H_2S, copper coupons were exposed to a gas flow of 2% H_2S with the balance H_2 at 95% RH and 23°C for 36 h. After exposure, the coupon showed a thick, black film on the surface.

XPS analysis of the black film indicated that the dominant S-2p peak was again centered at 162.0 eV as shown in Fig. 6a. A peak at 168 eV was also observed, indicating the presence of S-O coordinated species. Upon light sputtering ($\approx$2 nm etch), this high-BE peak disappeared altogether (Fig. 6b) leaving only the low-BE peak. This suggested that the outer layer of corrosion products reacted slightly subsequent to the test exposure. The oxysulfur species were present only in the superficial layers of the film. Indeed, as mentioned earlier, the XPS standards work on copper sulfide indicated similar S-O coordinations on the immediate surface layer. Copper in the film was present only in the univalent state.

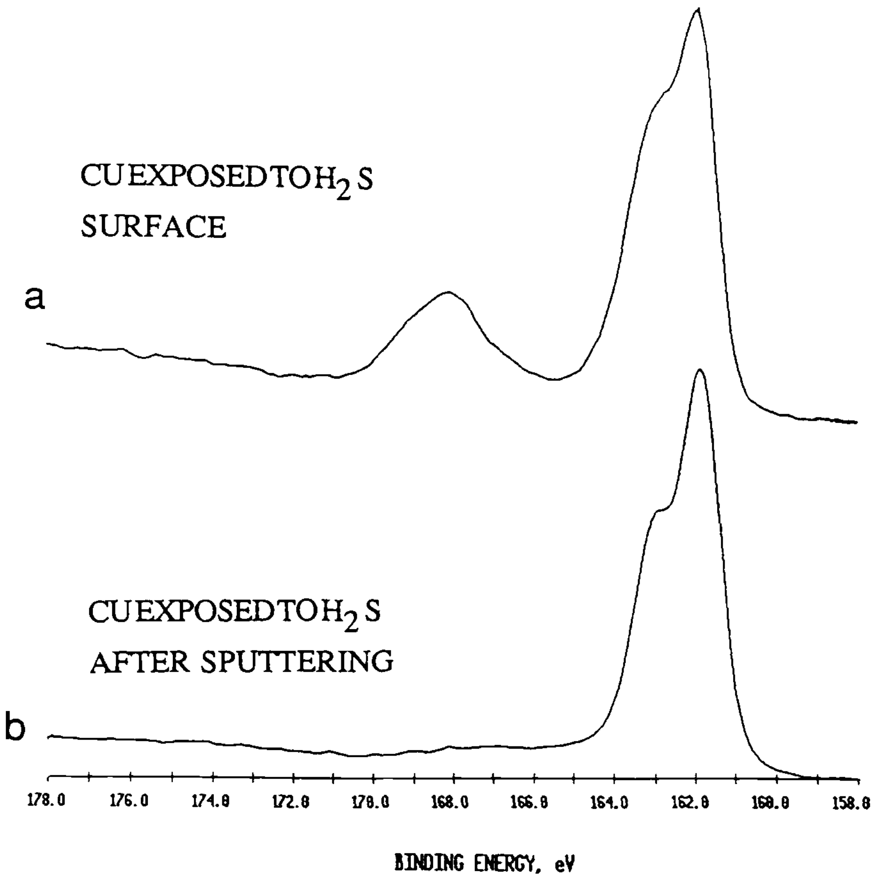

FIG. 6—*The S-2p band obtained by XPS analysis of copper exposed to air with 2% H_2S in H_2 with 95% RH at 23°C for 36 h:* (a) *before sputtering, and* (b) *after* ≈*2 nm sputter.*

Discussion

From the results of exposures of copper to the oxysulfur environments (SO_2, H_2SO_3, H_2SO_4), it is seen that some of the sulfur is transformed from its precursor S(+IV) state (in SO_2, H_2SO_3) and S(+VI) state (in H_2SO_4) to the S (−I, −II) state in copper sulfide in the corrosion film. It is difficult to distinguish by XPS analysis whether Cu_2S or CuS is formed. In the air-SO_2 exposures, some transformation of S(+IV) to S(+VI) also takes place. Yet, the formation of sulfides from these environments indicates that sulfur participates as a reducible species in the corrosion reactions as proposed previously by Rozenfeld [*23,24*]. The propensity of oxysulfur compounds such as SO_2 and H_2SO_4 to undergo reduction at the surface of copper, forming a black film of copper sulfide, has been extensively documented in literature (see compilation by Mellor *25*). The formation of sulfides in the corrosion products of metals exposed to SO_2-containing atmospheres has also been reported in several studies as discussed earlier. The results of the present work are in agreement with these studies.

Role of SO_2 in the Corrosion Reactions

The role of SO_2 in corrosion reactions on metals surfaces is commonly viewed as one of acidification of the adsorbed surface electrolyte and of incorporation into the corrosion products as sulfate. Rozenfeld [*23,24*], however, showed experimentally that addition of SO_2 to the atmosphere over a thin-film electrolyte on Cu caused a positive shift in the open-circuit potential of the metal. Thus, SO_2 could also function as an oxidizer (or a reducible species) in the system. Furthermore, Rozenfeld showed that the presence of SO_2 caused a change in the cathodic polarization characteristics of Cu under a thin electrolyte film. In the presence of SO_2, cathodic kinetics became more facile with a significant decrease in the absolute value of the cathodic Tafel slope. This was the result of SO_2 itself acting as an additional reducible species and participating directly in the reduction reaction. No significant effects of SO_2 were observed on the anodic polarization behavior of Cu under the same conditions. These features of SO_2 were characteristic of a cathodic depolarizer. The formation of sulfides was proposed to occur by a stepwise reduction of dissolved SO_2 through the dithionite anion ($S_2O_4^{2-}$) and the thiosulfate anion ($S_2O_3^{2-}$) to the sulfide ion in the cathodic process. The formation of sulfates was not precluded by this mechanism since the intermediate dithionite could also be oxidized in air to sulfate. Mikhailovskii et al. [*26,27*] proposed a slightly different mechanism for the formation of sulfates and sulfides in moist SO_2 exposures. The mechanism of electroreduction of SO_2 has also been investigated by electrochemical techniques such as polarography [*28*] and chronopotentiometry, coulometry, and voltammetry [*29*]. The mechanism is quite complex and appears to involve several stable intermediates such as sulfoxylic acid (H_2SO_2), dithionite ($S_2O_4^{2-}$), thiosulfate ($S_2O_3^{2-}$), and elemental sulfur.

Thermodynamic Calculations

Equilibrium calculations by Chawla and Payer [*30*] have shown that the reduction of SO_2 in thin film electrolytes on the surface of copper yielding a mixture of $Cu_2O + Cu_2S$ is thermodynamically possible. Thus, the thermodynamic calculations support the experimental analysis of corrosion product films. Like Rozenfeld's calculations, these calculations also suggest that the reduction of SO_2 can occur at more positive potentials than the reduction of Cu^+ ions over a wide range of SO_2 pressures. The overall electrochemical corrosion reaction includes the reduction of sulfur in SO_2 and the oxidation of copper to soluble ions.

Sulfide Formation in SO_2 Versus H_2S Exposures

The copper sulfides formed in SO_2 and in H_2S showed qualitative spectral similarity in XPS. The binding energy of the sulfide component (low BE) of the S-2p photopeak was approximately 162 eV in both cases. As mentioned earlier, the distinction between CuS and Cu_2S by XPS is difficult. There are other cation-deficient, nonstoichiometric sulfides of the type $Cu_{2-x}S$, such as djurleite and digenite, in the copper-sulfur system [*31*] which may also form during exposure. These species are also likely to be indistinguishable by XPS for similar reasons. However, this remains to be experimentally verified through the use of analytical standards. The high-BE S-2p envelope in the H_2S exposure was probably a result of air oxidation of the sulfide as noted by Murata et al. [*8*]. In the case of the SO_2 exposure, the high-BE S-2p peak was probably a result of the precursor and intermediate S-O coordinated species as well as some air oxidation of the sulfide.

Nevertheless, differences between the sulfides produced by the two exposures can be expected on the basis of their formation process. In the case of the H_2S exposure, sulfur is already present in the reduced S(−II) state in the environment and directly forms Cu_2S on the copper. However, in the case of the SO_2 exposure, the sulfur is present in an oxidized S(+IV) state in the environment, and the sulfide on copper forms through a reductive process. The reduction process involves several intermediates and may not proceed entirely to the terminal S(−II) state in the corrosion film. It is therefore quite possible that the reductively formed sulfide is defective both stoichiometrically as well as crystallographically. This would explain the poorly crystallized or amorphous nature of the sulfide formed in SO_2 exposures [*6,7,25*]. This may also explain why the coulometric reduction potential of the sulfide formed in the SO_2 exposures (Fig. 3) was different (200 mV more positive) from the reduction potential of the Cu_2S formed in typical H_2S exposures (Table 2). The reduction potential of sulfide formed in the SO_2 exposure was actually between the reported values for CuS and Cu_2S. The reduction characteristics of the film formed in SO_2 exposures need further examination in detail to evaluate these possibilities.

Conclusion

The following conclusions were drawn from this study:

1. XPS analysis shows that some sulfide is formed during the early stages of tarnishing of copper in moist air-sulfur dioxide environments. Copper sulfide is also formed on copper immersed in "sulfurous" and sulfuric acids after longer exposures. The spectral features of the sulfide formed reductively from the above exposures are similar to the spectral features of the sulfide formed by an H_2S exposure.
2. The electrochemical reduction potential of the film formed in the SO_2 exposure is between the reported values for CuS and Cu_2S. The reduction potential of this film is about 200 mV more positive than the reduction potential of the sulfide formed in H_2S exposures. This may be a result of nonstoichiometry of the reductively formed sulfide (from SO_2). However, the coulometric reduction behavior of this sulfide requires more detailed investigation.
3. The formation of some sulfide in the SO_2, H_2SO_3, and H_2SO_4 exposures of copper reaffirms the results of prior studies which have concluded that some of the sulfur in sulfur dioxide participates as a cathodic depolarizer in corrosion reactions and is reduced to sulfide.

Acknowledgments

This research was partially funded by the Foil Division of Gould Inc. The authors would like to thank Earl Johns at Digital Equipment Corp., Colorado Springs for conducting some of the flowing mixed gas exposures and performing electrochemical reduction analyses. The XPS work was conducted with the assistance of N. Sankarraman at the Center for Surface Analyses of Materials at CWRU. B. I. Rickett acknowledges support under a National Science Foundation graduate fellowship. The authors appreciate the assistance of Theo Shlien in preparing the final manuscript.

References

[*1*] Chawla, S. K. and Payer, J. W., "The Early Stage of Atmospheric Corrosion of Copper by Sulfur Dioxide," *Journal of the Electrochemical Society*, Vol. 137, 1990, p. 60.

[2] Sydberger, T. and Vannerberg, N.-G, "The Influence of the Relative Humidity and Corrosion Products on the Adsorption of Sulfur Dioxide on Metal Surfaces," *Corrosion Science*, Vol. 12, 1972, p. 775.

[3] MLeod, W. and Rogers, R. R., "Sulfurous Acid Corrosion of Low Carbon Steel at Ordinary Temperature," *Corrosion*, Vol. 22, 1966, p. 143.

[4] McLeod, W. and Rogers, R. R., "Corrosion of Metals by Aqueous Solutions of the Atmospheric Pollutant Sulfurous Acid," *Electrochemical Technology*, Vol. 6, 1968, p. 231.

[5] Ross, T. K. and Callaghan, B. K., "A Sulfide Mechanism in the Rusting of Mild Steel," *Electrochemical Metallurgy*, Vol. 2, No. 1, 1967, p. 22.

[6] Johansson, L.-G. and Vannerberg, N.-G., "The Corrosion of Unprotected Steel in an Inert-gas Atmosphere Containing Water Vapor, Oxygen, Nitrogen and Different Amounts of Sulfur Dioxide and Carbon Dioxide," *Corrosion Science*, Vol. 21, 1981, p. 863.

[7] Sydberger, T. and Ericsson, R., "Laboratory Testing of the Atmospheric Corrosion of Steel," *Werkstoffe und Korrosion*, Vol. 28, 1977, p. 154.

[8] Murata, K., Ikeda, S., Utsunomiya, T., and Yasui, A., "X-Ray Photoelectron Spectrometric and X-Ray Fluorometric Studies of Sulfur Compounds on the Surface of Copper Plates Exposed to the Atmosphere," *Talanta*, Vol. 23, 1976, p. 529.

[9] Chawla, S. K., Sankarraman, N., and Payer, J. H., "Diagnostic Spectra for XPS Analysis of Cu-O-S-H Compounds," submitted to *Journal of Electron Spectroscopy and Related Phenomena.*

[10] Prewitt, C. T. and Rajamani, V. in *Sulfide Mineralogy*, Mineralogical Society of America, Short Course Notes, Southern Printing Co., Blacksburg, VA, 1974, p. PR-30.

[11] Romand, M., Rouzam, M., and Deloume, J. P., "ESCA Studies of Some Copper and Silver Selenides," *Journal of Electron Spectroscopy and Related Phenomena*, Vol. 13, 1978, p. 229.

[12] Adou, J. J. and Baudet, J., *Journal de Chimie Physique*, Vol. 64, 1967, p. 1540.

[13] Jellinek, F. in *Inorganic Sulfur Chemistry*, D. M. Brewis, Ed., Elsevier Publishing Company, Amsterdam, 1968, p. 682.

[14] Wagner, C. D., *Journal of Vacuum Science and Technology*, Vol. 15, 1978, p. 518.

[15] Kruger, J., "Some Brief Remarks on Electrochemical Reduction," in *Corrosion and Metal Artifacts—A Dialogue Between Conservators and Archaeologists and Corrosion Scientists,* NBS Special Publication 479, B. F. Brown, H. C. Burnett, W. T. Chase, M. Goodway, J. Kruger, and M. Pourbaix, Eds., National Bureau of Standards, Gaithersburg, MD, 1977, p. 59.

[16] Vedel, J. and Soubeyrand, M., "Electrochemical Analysis of Copper Oxides Present in Copper Sulfides," *Journal of the Electrochemical Society*, Vol. 127, 1980, p. 1730.

[17] Peide, Z., Procter, R. P. M., Grant, W. A., and Ashworth, V., "Tarnishing of Ion Implanted Copper in Hydrogen Sulfide Containing Atmospheres," *Nuclear Instruments and Methods*, Vol. 209/210, 1983, p. 841.

[18] Fiaud, C., Safavi, M., and Vedel, J., "Identification of the Corrosion Products Formed on Copper in Sulfur Containing Environments," *Werkstoffe Korrosion*, Vol. 35, 1984, p. 361.

[19] Hoar, T. P. and Stockbridge, C. D., "Coulometric Reduction of Cuprous Sulfide Films on Copper," *Electrochimica Acta*, Vol. 3, 1960, p. 94.

[20] Allen, J. A., "Oxide Films on Electrolytically Polished Copper Surfaces," *Transactions of the Faraday Society*, Vol. 48 I, 1952, p. 273.

[21] Curren, W. J., Martin, J. R., and Gilson, P., "Design and Characteristics of a Mixed Gas Environmental Chamber," *Proceedings*, CORROSION/85, NACE, Houston, TX, 1985, Paper No. 326.

[22] Volpe, L. and Petersen, P. J., "The Atmospheric Sulfidation of Silver in a Tubular Corrosion Reactor," *Corrosion Science*, Vol. 29, 1989, p. 1179.

[23] Rozenfeld, I. L., "Atmospheric Corrosion of Metals—Some Questions of Theory," *Proceedings*, 1st International Congress on Corrosion, Butterworths, London, 1962, p. 243.

[24] Rozenfeld, I. L. in *Atmospheric Corrosion of Metals*, E. C. Greco, Ed., NACE, Houston, TX, 1972, p. 125.

[25] Mellor, J. W., *A Comprehensive Treatise on Inorganic and Theoretical Chemistry*, Vol. III, Longmans, Green and Co., London, 1923, p. 213.

[26] Mikhailovskii, Y. N., Strekalov, P. V., and Balandina, T. S., "Adsorption of Sulfur Dioxide on Metals and Its Influence on Atmospheric Corrosion," *Zaschita Metallov*, Vol. 14, No. 3, 1978, p. 248.

[27] Mikhailovskii, Y. N. and Sokolov, N. A., "New Ideas on the Mechanism by Which Sulfur Dioxide Stimulates the Atmospheric Corrosion of Metals," *Zaschita Metallov*, Vol. 21, No. 2, 1985, p. 214.

[28] Kolthoff, I. M. and Miller, C. S., "The Reduction of Sulfurous Acid (Sulfur Dioxide) at the Dropping Mercury Electrode," *Journal of the American Chemical Society*, Vol. 63, 1941, p. 2818.

[*29*] Jacobsen, E. and Sawyer, D. T., "Electrochemical Reduction of Sulfur Dioxide at a Mercury Electrode," *Journal of Electroanalytical Chemistry*, Vol. 15, 1967, p. 181.
[*30*] Chawla, S. K. and Payer, J. H., "Thermodynamic Perspective of Indoor Atmospheric Corrosion," *Proceedings*, CORROSION/90, NACE, Houston, Texas, 1990, Paper No. 226.
[*31*] Cook, W. R., "The Copper-Sulfur Phase Diagram," Ph.D. dissertation, CWRU, 1971.

Keith Goodson[1] *and Robert Cormia*[2]

The Effect of Conversion Coated and Plated Components on the Corrosion of Cobalt Alloy Magnetic Disks

REFERENCE: Goodson, K. and Cormia, R., "**The Effect of Conversion Coated and Plated Components on the Corrosion of Cobalt Alloy Magnetic Disks,**" *Corrosion of Electronic and Magnetic Materials, ASTM STP 1148,* P. J. Peterson, Ed., American Society for Testing and Materials, Philadelphia, 1992, pp. 36–45.

ABSTRACT: Common disk drive components with chromate conversion coatings or electroless nickel platings were analyzed by ion chromatography for residual levels of Cl^-, F^-, SO_4^{2-}, and NO_3^-. Extraction with boiling DI water revealed levels up to several hundred ng/cm^2 for these anions. When these components were placed 2 mm under a suspended cobalt-nickel-phosphorous disk in an environmental chamber at 55°C/85% RH, corrosion of the cobalt disk occurred directly over the chromated component when the total level of anions was greater than 200 ng/cm^2. This accelerated corrosion did not occur in a 120-h test when the level was less than 50 ng/cm^2. The amount of corrosion was found to be dependent on the separation distance between the disk and the chromated component.

Surface analysis of the disk corrosion area exposed to a chromate conversion coating showed NiO, CoO, and an increased concentration of chlorine.

KEY WORDS: chromate conversion coatings, electroless nickel plating, cobalt magnetic disks, corrosion, corrosion analysis

The decade of the eighties witnessed a rapid increase in the density of magnetic storage for computer applications. This increase eventually necessitated the change from magnetic iron oxide particles to cobalt alloy metallic thin film disks. One disk requirement is that exposure to humidity, temperature, and environmental pollutants must not cause corrosion, which can lead to a loss in data integrity and mechanical reliability. The understanding of corrosion has helped the successful introduction of cobalt alloy media in many current applications. Particularly important are the 130, 95, and 65-mm-diameter disk drive applications which dominate the work station and personal computer markets.

Concern regarding corrosion reliability has lead to several papers and reviews [*1–2*]. Corrosion studies on cobalt thin film magnetic alloys include Co-P [*3–4*], Co-Ni-P [*5*], Co-Pt/Co-Ni-Pt [*6*], Co-Cr [*7–8*], and Co-Ni-M [*9*], where M is Zr, Cr, Mo, and Pt. In general, the above studies have verified the electrochemical nature of the cobalt corrosion process and have shown that corrosion properties depend on alloy composition, processing conditions, overcoat, and atmospheric contaminants.

In the electrochemical mechanism [*10*], water adsorbs on the already hydroxylated cobalt surface in microscopic stabilized droplets. Within these droplets corrosion occurs as localized oxidation-reduction reactions. While the electrochemistry of the aqueous microregions is

---

[1] Manager, Materials Analysis, Censtor Corporation, San Jose, CA 95152.

[2] Manager, Organic Analysis, Surface Science Laboratories, Mountain View, CA 94043.

complex, it is clear that adsorbed water, ionic contaminants, and surface morphology provide the basis for electrochemical attack.

Current high performance disk drives are recording at linear densities up to 1530 flux changes per millimetre [39 000 flux changes per inch (FCI)] and track densities up to 79 tracks per millimetre [2000 tracks per inch (TPI)], and within the next two years these densities may reach 80 000 FCI at 2500 TPI with emerging technologies such as contact vertical recording. A calculation for an *80 000 FCI*, 2500 TPI disk shows that the corrosion of less than 3 μm^2 of cobalt at a depth of 30 to 60 nm can result in the loss of 1 bit of information. Substantially smaller corrosion amounts will produce data loss in future systems. The increase in recorded information density has also made possible a decrease in the total size of disk drives. The current drives in use and under development can be less than 1 in. high and 2 or 3 in. in length and width. This size decrease has brought the cobalt alloy disk closer to the surfaces of drive components such as head arms, motor flanges, cases, and wiring harnesses. In addition, the ratio of drive void volume to surface area has decreased, potentially increasing the concentration of volatile contaminants or corrosion accelerators in the drive atmosphere.

A significant broadening of environmental temperature and humidity distribution can be expected in the next few years as large numbers of portable and lap top computers are placed into service. Computers will no longer reside in controlled office environments but will be exposed to varied ambient temperatures and humidities throughout the world.

Disk drives typically contain cast metal components (mainly Al alloys) which are surface modified with a conversion process such as chromating or plated electroless nickel. The objective of this work was to study the effect of residual ionic compounds left as a result of these processes on corrosion of cobalt alloy thin film magnetic disks.

Experimental

Multiple drives from five commercially available models were examined for conversion coated and plated components. These components were analyzed by SEM/EDX or X-ray fluorescence and grouped according to process and base metal as shown in Table 1.

In order to minimize differences caused by handling procedures, representative components from the drives were given a 15-s immersion in room temperature DI water. After immersion rinsing, the samples were refluxed in boiling DI water for 1 h. The water was analyzed with a Dionex 450I ion chromatograph for extracted levels of Cl^-, F^-, SO_4^{2-}, and NO_3^-. The eluent was a carbonate (1.7 m*M*) and sodium bicarbonate (1.8 m*M*) solution. Twenty-five μL of sample was injected at a flow rate of 2 mL/min. The column was an Ion Parc A54A.

TABLE 1—*Drive component anion content.*

		ANION CONTENT (FIRST EXTRACTION)				
		Number	Anion Range (ng/cm^2)			
Surface Treatment	Base Metal	of Samples	F^-	Cl^-	NO_3^-	SO_4^{2-}
Chromate	Aluminum	45	15–417	20–270	19–556	3–380
Nickel	Aluminum	9	0	20–86	0	12–89
Nickel	Magnesium	6	0	14–92	0	26–47
		ANION CONTENT (SECOND EXTRACTION) (NG/CM^2)				
Chromate	Aluminum	45	0–15	0–13	0–28	0–20
Nickel	Aluminum	6	0	0–4	0	0–5
Nickel	Magnesium	3	0	0–5	0	0–2

The levels of extracted anions were expressed as grams per square centimeter of component surface.

After the initial extraction with boiling DI water, the procedure was repeated with the same components. In all cases the second boiling water extraction level of anionic contaminants was less than 5% of the initial extraction concentrations (Table 1).

Multiple samples of components, some extracted with DI water and some not extracted, were placed 2 ± 1 mm under suspended cobalt-nickel-phosphorous (CoNiP) plated magnetic disks. The disk and components were set in a polycarbonate desiccator fitted with four filtered 12.5-mm openings and the entire apparatus placed in a temperature-humidity chamber at 55°C/85% RH. The disks had an overcoat of 35 ± 5 nm sputtered carbon and were lubricated with a perfluorinated polyether lubricant. The disks had previously been certified for magnetic recording defects. Error locations corresponding to a signal loss of 40% at recording densities of 15 000 FCI and 2000 TPI were noted.

The corrosion was monitored by measuring the change in intensity of scattered light from the disk for areas both directly over drive components and areas away from drive components. In previous descriptions of this technique [*11*], a sharp increase in slope was defined as the induction time and was used as a measure of corrosion resistance. In this study the reflected intensity from disk areas exposed to the drive components was divided by areas not exposed to components on the same disk. When the slope increased sharply, the drive component was causing corrosion on the disk surface.

The above procedure was repeated with chromated parts suspended at increasing spacings from the disk surface. This procedure was performed only on the chromated components with anion concentrations greater than 200 ng/cm^2.

The disks were recertified for magnetic recording defects at 24-h intervals during the temperature-humidity test. Control disks were placed in the same chamber and certified at the same intervals.

ESCA measurements were performed on disk surfaces exposed to chromated specimens which exhibited corrosion defect growth. The measurements were used to determine the surface composition of elements within the outer 40 to 50 Å of the disk. All ESCA measurements were performed on a Surface Science Instruments microbeam ESCA spectrometer. The composition data were calibrated using pure standards and interpolation. The approximate dimensions analyzed were 600 by 1000 μm (ellipse).

Microbeam Auger electron spectroscopy (AES) analyses were performed on corrosion nodules and adjacent noncorroded areas using a Perkin Elmer 590 system.

The AES and ESCA measurements were used to interpret the qualitative differences in surface chemistry of the corroded and noncorroded areas.

Results and Discussion

Chromate conversion processes depend on a reaction at the metal surface where hexavalent chromium is reduced to the trivalent form and precipitates as a complex chromium gel on the metal surface [*11*]. This coating contains both trivalent and hexavalent chromium compounds as well as anionic species listed in Table 1. The anionics stem from either the aluminum pretreatment process or the chromating process. Typical cleaning and chromating processes are defined in ASTM Practices for Preparation of Aluminum and Aluminum-Alloy Surfaces for Painting (D 1730-67a) and ASTM Practice for Chromate Treatments on Aluminum (B 449-67a).

Electroless nickel is plated from solutions containing sulfuric or hydrochloric acid. Large variations exist in formulations depending upon application and base metal. Preplating procedures for magnesium are covered in ASTM Practices for Preparation of Magnesium Alloy

Surfaces for Painting (D 1732-67) and show that multiple combinations of alkaline solutions and acid cleaners are used depending on alloy and intended use.

Table 1 shows the level of anions (ng/cm^2) extracted from chromated drive components and the levels removed during a second 1-h extraction at 100°C in DI water. Substantial differences were noted among the chromating processes. Table 1 also shows level of anions (ng/cm^2) for electroless nickel overcoats and the amount removed during a second 1-h extraction.

Figure 1 is a graph of reflected light intensity versus time for areas exposed to chromated drive components at 55°C/85% RH. For this study the components were placed 2 ± 1 mm under the disk surface. The chromating process with residual levels of anions greater than 200 ng/cm^2 caused increased corrosion at the 40 to 60-h time frame. The materials which were extracted to less than 50 ng/cm^2 of anions did not cause increased corrosion. Reflected light measurements from disks exposed to electroless nickel showed no evidence of increased corrosion. The error bar shown in Fig. 1 is the total range of data collected for three separate evaluations.

While the electroless nickel plated on both the aluminum and magnesium components did not cause accelerated corrosion in this evaluation, they also had significantly lower levels of the four anionic contaminants. Further studies are necessary where electroless nickel samples are prepared under controlled conditions at various levels of residual ionic contaminants.

The disks were tested for formation of new recording defects at approximate 24-h intervals. The increase in the number of defects on disks exposed to the chromated and nickel-plated parts is shown against control samples. Figure 2 shows a defect increase for the parts exposed to components with the higher level of anions. The curves were consistent with the reflected light tests. The shape of the curve depends on the size of magnetic defect which the certifier

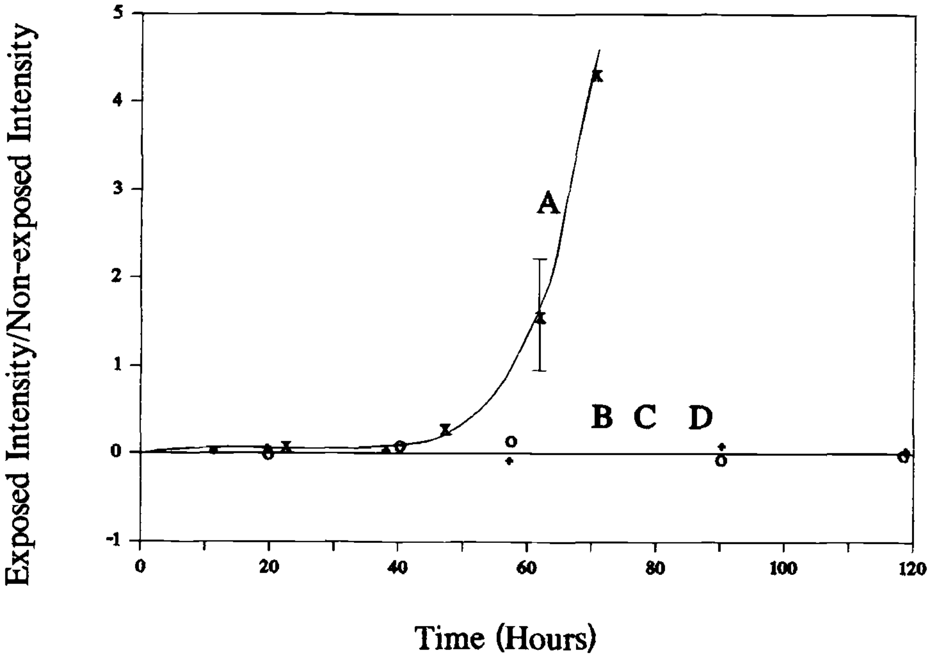

FIG. 1—*Scattered light intensity ratio 1/m area exposed divided by nonexposed area: (A) chromate, anions > 200 ng/cm^2; (B) electroless nickel; (C) control disk; (D) chromate after DI extraction, anions < 50 ng/cm^2.*

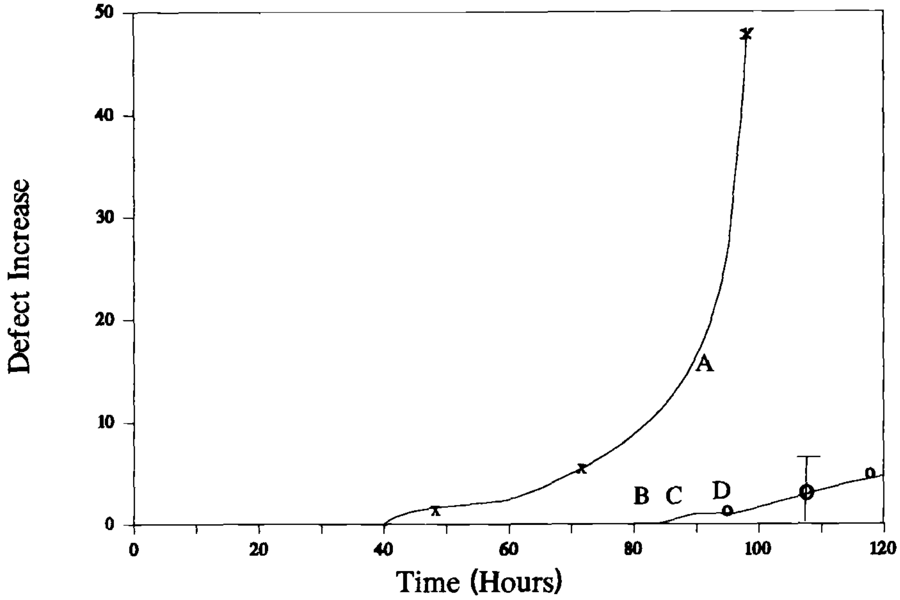

FIG. 2—*Defect increase versus time: (A) chromate exposed disk. Anion content > 200 ng/cm²; (B) electroless nickel; (C) control disk; (D) chromate after extraction, anions < 50 ng/cm².*

recognizes. The capability of varying recognizable size did not exist in this study. The error bar shown in Fig. 2 represents the total range of data for three separate trials.

Figure 3 shows a relationship between the separation distance of the chromated component and the degree of corrosion on the cobalt alloy media. It is clear that corrosion is increased as the component is brought closer to the disk. This would indicate that a higher concentration of pollutants near the disk surface as well as the efficiency of adsorption onto the disk are important in the corrosion acceleration mechanism. The analysis of the gas phase over the drive components was beyond the scope of this study. The error bars again indicate the range of data for three separate trials.

A disk area exposed to a chromate component for 40 h at 55°C/85% RH is shown in the upper SEM micrograph of Fig. 4. The lower micrograph of Fig. 4 is the same sample after 120 h of exposure. The corrosion products formed along polishing and texture lines in agreement with previous studies [*12*].

The AES analyses of the chromate-exposed coatings with increased corrosion rates revealed typical spectra for corroded cobalt alloy disks [*13*]. The surface nodules showed carbon, cobalt, nickel, chlorine, and oxygen. A surface spectra from a noncorroded area revealed only carbon and a trace of oxygen (Fig. 5).

The ESCA analyses from disk areas exposed to chromated drive components and disk areas not exposed to drive components are shown in Fig. 6. These data show that disk surfaces directly exposed to chromated components with anion contents greater than 250 ng/cm² exhibited significant amounts of cobalt and nickel in an oxidized form. Elevated levels of chlorine were detected and would appear to be a likely corrosion accelerator. In comparison, the control disk showed only trace amounts of cobalt (in an oxidized form), which is typical of carbon overcoated media with cobalt alloy magnetic films. No chlorine or nickel was detected.

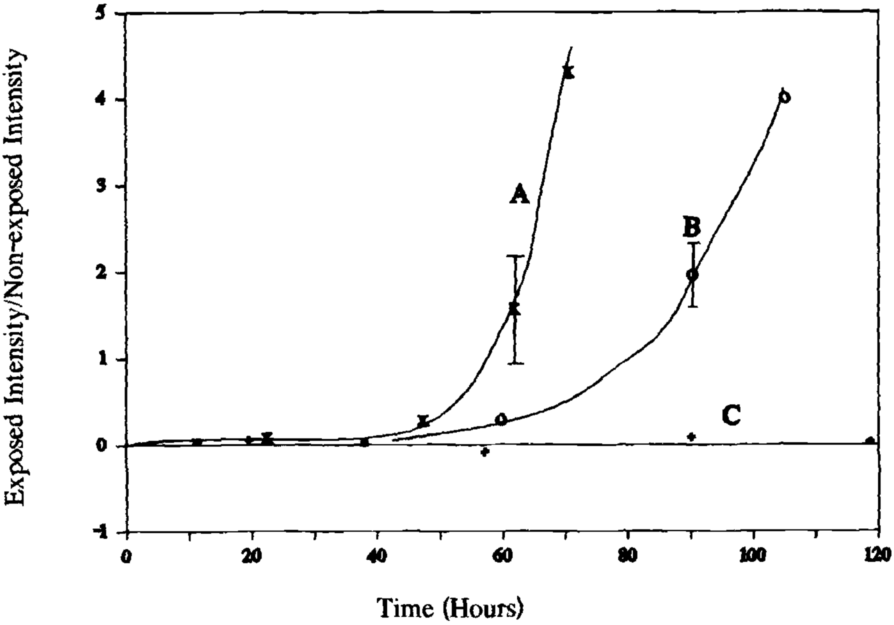

FIG. 3—*Scattered light intensity ratio versus distance from component: (A) 2 mm; (B) 4 mm; (C) 8 mm.*

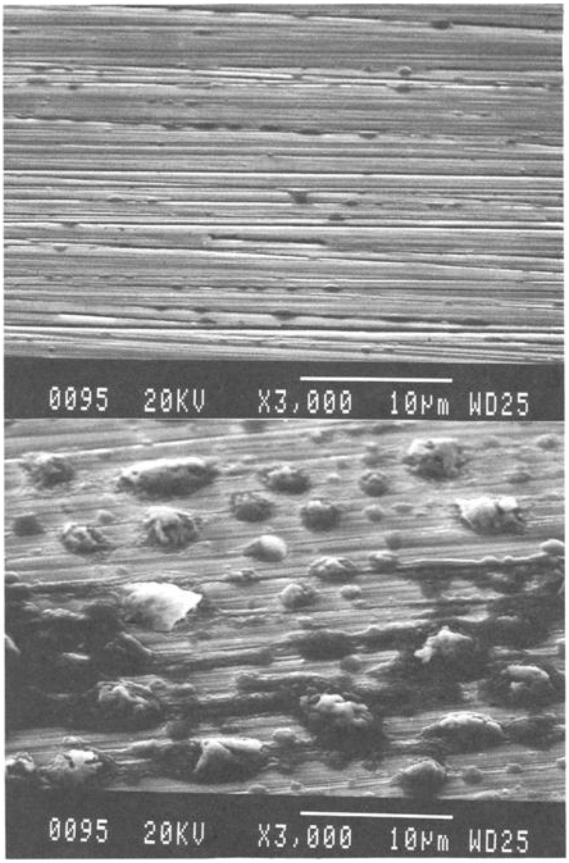

FIG. 4—*Upper SEM micrograph, chromate-exposed disk surface after 40 h at 55°C/85% RH. Lower*

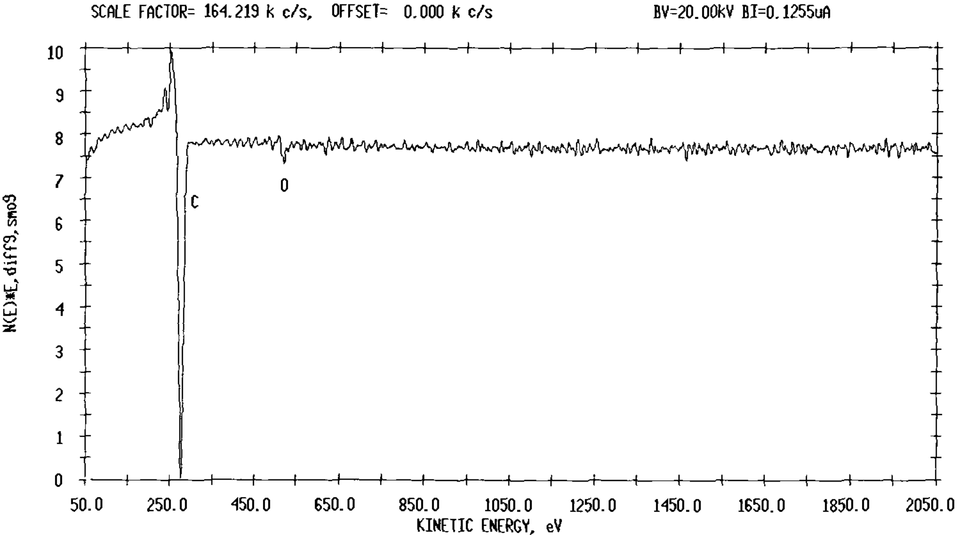

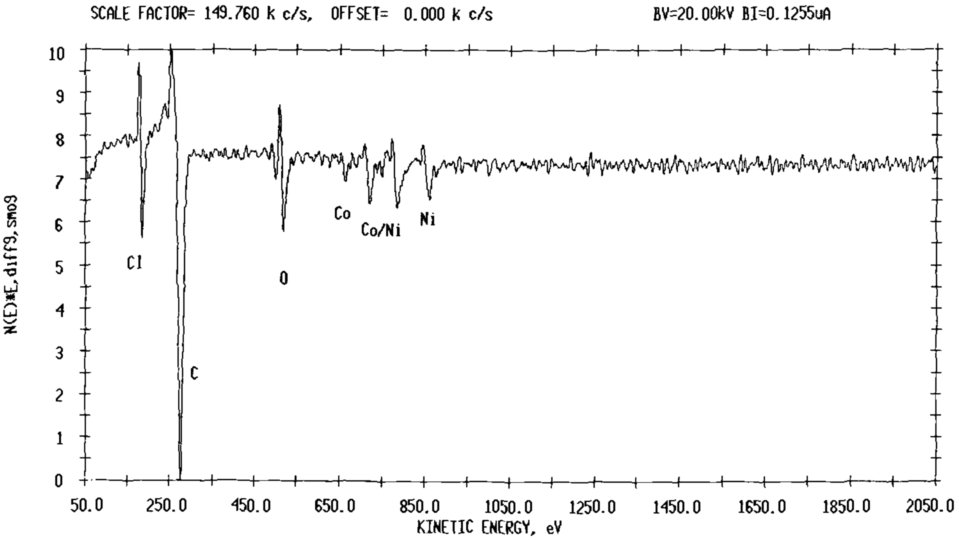

FIG. 5—*AES spectra: (top) noncorroded disk surface area; (bottom) corroded disk area (nodule).*

The AES and ESCA data confirm that significant corrosion products are formed at the surface of the carbon overcoat in disk areas directly exposed to chromated components with anion contents greater than 200 ng/cm^2 at 55°C/85% RH. The level of chlorine detected on the corroded disk surface indicates that a gas phase transfer of a chlorine-containing compound has taken place between the chromated component and the disk.

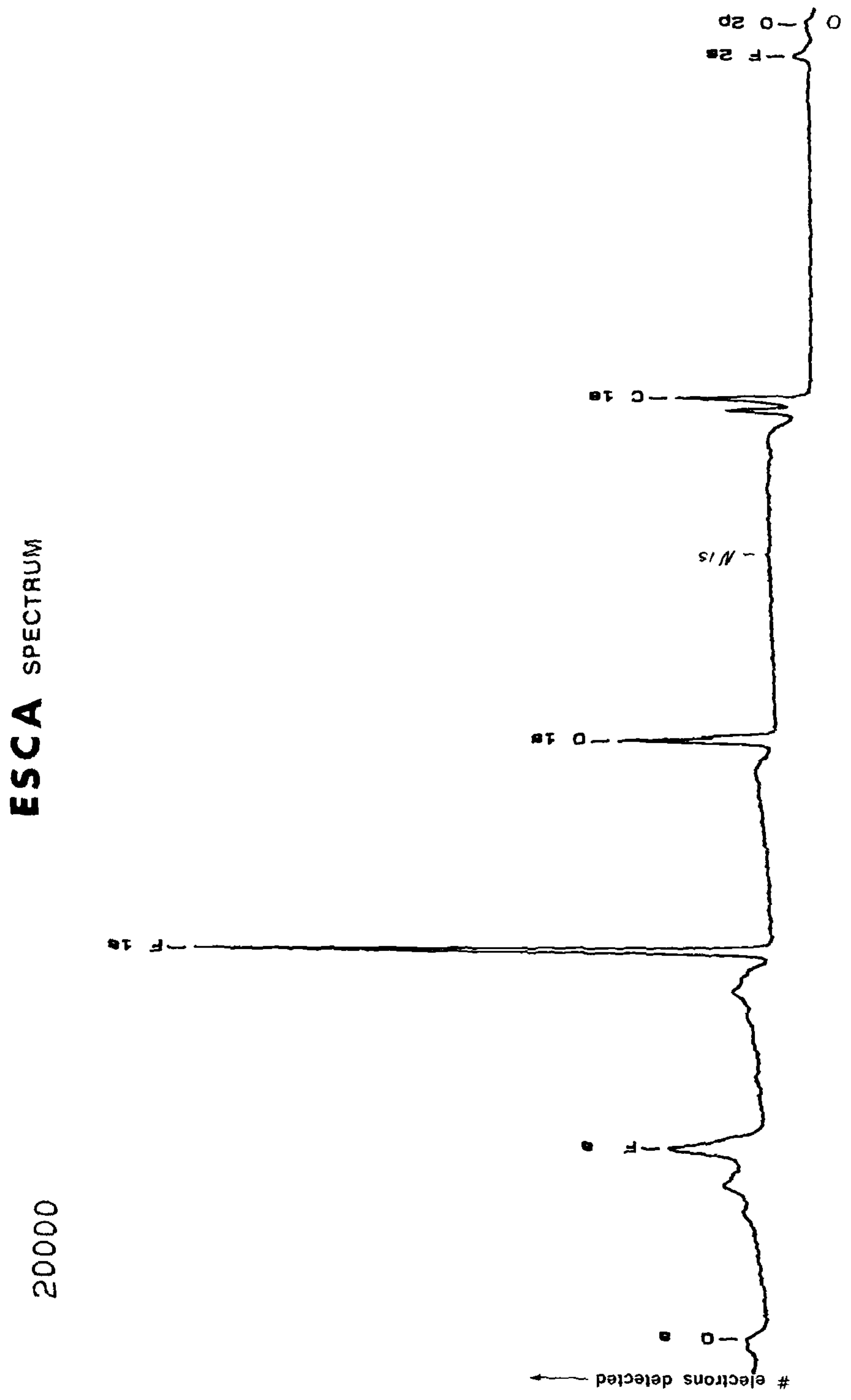

FIG. 6—*ESCA spectra: (top) noncorroded disk surface area; (bottom) corroded disk area (nodule).*

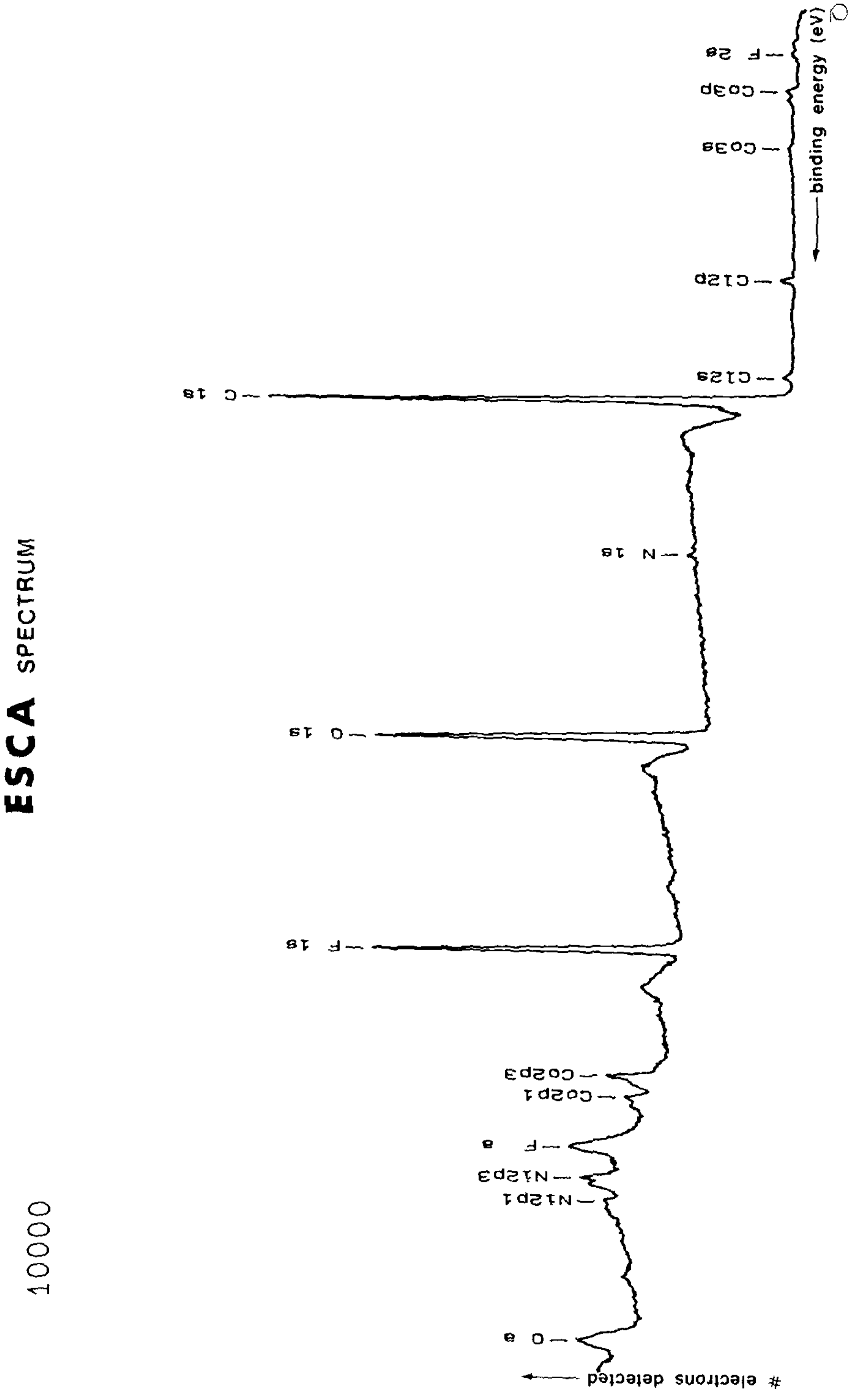

FIG. 6—*Continued*

Conclusion

Coatings such as electroless nickel and chromate conversion coatings have been used successfully in disk drives for protective and engineering purposes for a number of years. With the advent of cobalt alloy media, higher information density, and smaller drives, corrosion concerns will force continuing attention on the materials of construction and their effects on corrosion.

This study established that ionic materials left on metal drive components as a result of conversion coating processes, such as chromating, accelerate the corrosion of cobalt alloy media through a gas phase transfer process. The problem can be eliminated by monitoring and controlling the surface anionic content of the metal conversion process. The most likely corrosion catalyst is a chlorine-containing compound.

The relationship of corrosion acceleration to surface ion concentration on chromated parts adjacent to the disk emphasizes the need for quality control techniques such as ion chromatography. Sensitivity to corrosion will increase as drives become smaller and information density increases. Qualitative analysis of extractable contaminants will be necessary to ensure continued drive corrosion reliability.

References

[*1*] Fisher, R. D., "A Review of Corrosion Testing and Evaluation of Thin-Film Media," *Proceedings*, Institute for Information and Storage Technology (IIST) symposium, May 1986, WS#-B-2, pp. 1–25.

[*2*] Ju, J.-B. and Smyrl, W. H., "Corrosion Studies of Thin-Film Materials for Magnetic and Microelectronic Applications," *Proceedings*, 3rd ASM conference on electronic packaging, 1987, American Society for Metals, Metals Park, OH, pp. 119–130.

[*3*] Judge, J. S., Morrision, J. R., Speliotis, D. E., and Bate, G., *Journal of the Electrochemical Society*, Vol. 112, 1965, p. 681.

[*4*] Cormia, R. D., "Elevated Temperature/Humidity Corrosion of Cobalt Phosphide Plated Magnetic Media," *Proceedings*, Fourth Conference of NACE, April 1990.

[*5*] Garrison, M. C., *IEEE Transactions Magazine*, MAG-19, 1983, p. 1683.

[*6*] Yanagisawa, M., Shiota, M., Yamaguchi, H., and Suganuma, Y., *IEEE Transactions Magazine*, MAG-19, 1983, p. 1638.

[*7*] McIntire, G. L. and Brucker, C. F., *IEEE Transactions Magazine*, MAG-24, 1988, p. 2221.

[*8*] Dubin, R., Winn, K., Davis, L., and Cutler, R., *Journal of Applied Physics*, Vol. 53, 1982, p. 2579.

[*9*] Suzuki, H., Shiroishi, Y., Hishiyama, S., Ohno, T., Matsuda, Y., Matsunaga, F., and Tsumita, N., *IEEE Transactions Magazine*, MAG-23, 1987, p. 3411.

[*10*] Rice, D. W., Phipps, P. B. P., and Tremoureux, R., *Journal of the Electrochemical Society*, Vol. 126, 1979, p. 1459.

[*11*] Smallen, M., Mee, P. B., Ahmad, A., Freitag, W., and Nanis, L., *IEEE Transactions Magazine*, MAG-21, 1985, p. 1530.

[*12*] Lowenheim, F., *Electroplating, Fundamentals of Surface Finishing*, McGraw-Hill, New York, 1978, p. 442.

[*13*] Merchant, K., Smallen, M., Fisher, R., and Smith, S., *Journal of Applied Physics*, Vol. 67, 1990.

[*14*] Novotny, V., Itynre, G., Homola, A., and Franco, L., *IEEE Transactions Magazine*, MAG-23, 1987, p. 3645.

John Setchell[1]

Accelerated Environmental Testing of Magnetic Recording Disks

REFERENCE: Setchell, J., "**Accelerated Environmental Testing of Magnetic Recording Disks,**" *Corrosion of Electronic and Magnetic Materials, ASTM STP 1148,* P. J. Peterson, Ed., American Society for Testing and Materials, Philadelphia, 1992, pp. 46–52.

ABSTRACT: An accelerated test of the stability of images recorded on still video floppy disks was conducted by incubating disks at elevated temperatures. Small changes in the playback output were detected at 7 MHz, enabling prediction of storage life at ambient temperature by extrapolation. The test method revealed changes equivalent to a few nanometres in film thickness.

KEY WORDS: magnetic recording, image stability, Arrhenius testing, video recording, MP media, still video floppy, accelerated life testing

People who record images on photographic film or other media generally do so with the expectation that these images will be usable after some period of storage of the media. Extensive studies have been made of the stability of images recorded on photographic film with respect to storage conditions, but the keeping properties of magnetic media (disks and tapes) have been less studied. Several articles [*1–4*] provide recommendations for improving storage life but give no quantitative predictions.

The present study was undertaken to develop information on the properties of one magnetic recording format of particular interest: the still video floppy (SVF) disk. The technique used is applicable to other formats, and the sensitivity of the method to detect very small changes is of general interest.

Carrying out these experiments required state-of-the-art precision in magnetic recording measurement technology. The changes observed were very small, even under the aggressive conditions of high-temperature incubation used to accelerate aging. Arrhenius testing was used, based on the assumption that a logarithmic plot of the rate constant versus the reciprocal of the temperature results in a straight line.

Accelerated Life Testing

Life testing of many products is subject to a common problem: the expected service life is much longer than the time available to conduct a practical test. The usual approach to this problem is to attempt to accelerate the test by increasing the stress. Care must be taken to assure that inappropriate failure modes are not introduced by this process. This requirement implies a good understanding of the product and its probable failure mechanism.

For many products, the failure mechanism is related to chemical reactions between the environment and the materials of the product. Examples include the weathering of building construction materials and the corrosion of automobiles and electrical contacts. For metallic particle magnetic recording media, dimensional changes, polymer degradation, and particle

---

[1] Color systems engineer, Eastman Kodak Co., Rochester, NY 14653-3700.

corrosion could be expected after long-term storage. Tracking errors, head clogging, increased head-to-media spacing, and loss of magnetization would all be detected as a reduction in signal output or other changes in signal parameters.

There are two ways to accelerate chemical reactions: one is to increase the concentration of the reactants, and the other is to raise the temperature. Increasing the humidity is an example of the first approach.

Relating the failure rate under stress to the failure rate in normal service requires an understanding of the chemical reaction kinetics. For concentration stress, this can be a significant problem, not least because of the difficulty in determining the exact nature of the reactions and the appropriate concentrations. The situation for temperature stress is much easier: the dependence of the reaction rate on temperature can usually be represented by the empirical equation proposed by Arrhenius in 1889

$$k = Ae^{-E/RT}$$

where

A = an empirical constant,
E = the activation energy,
R = the gas constant, and
T = the absolute temperature [5].

Thus a plot of the logarithm of the rate constant k versus the reciprocal of the temperature would result in a straight line.

For the purposes of accelerated testing, this means that two or more measurements of life at elevated temperatures (where chemical reactions take place more quickly) may be extrapolated with some confidence to ambient temperature (provided that the nature of the reactions does not change).

Failure Mechanisms

Three possible failure mechanisms may be readily identified pertaining to magnetic recording materials: (1) degradation of the binder by ultraviolet light, (2) print through or erasure by magnetic fields, and (3) corrosion of the magnetic particles and degradation of the binder by chemical action of the atmosphere.

The SVF disk is essentially immune to effects of ultraviolet light since the magnetic materials are totally enclosed within a protective jacket. The shutter providing access for the record or playback head is opened only when the disk is inserted within a recorder or player.

The SVF disk is not subject to the kind of print through experienced with magnetic tape because the thickness of the jacket prevents close contact with other magnetic materials. The high coercivity of the SVF media (about 1300 Oe) also provides substantial protection against erasure by external fields.

This paper addresses the remaining concern, the ability of the SVF materials to withstand the corrosive effects of the environment. In studies at the Kodak Research Laboratories, temperature and humidity were found to be important contributors to the corrosion of magnetic particles used in disks of this type, and it remained to relate this effect to changes in recording performance.

Metallic Particle Materials

Traditional magnetic recording media are based on oxides of iron or chromium. These materials typically have coercivities in the range of 350 to 750 Oe and are quite stable in most environments. Applications requiring higher coercivity have adopted the use of metallic particle (MP) media. These materials are based on iron and alloys of iron in the zero valence state and have coercivities in the range of 700 to 2000 Oe. The particles are usually passivated to improve corrosion resistance. Applications for MP media include audio cassettes, 8-mm video tape, rotary digital audio tape (RDAT), and SVF disks.

Still Video Floppy Format

The SVF specification [*6*] was adopted by the 41-member Electronic Still Camera Conference to facilitate widespread acceptance of the format. The disk is 47 mm in diameter and rotates at 3600 rpm. Video signals are recorded using frequency modulation; the frequency corresponding to peak white, for example, is 7.5 MHz. Playback output at various frequencies is specified. The magnetic characteristics of the medium are not directly specified. Disks currently on the market, however, are MP type with a coercivity about 1300 Oe.

Testing of SVF Disks

For the Phase I experiment, signals were recorded on 50 disks using a Kodak SV7400 player. The disks were played back on the same player, and measurements were made of luminance and chrominance signal-to-noise ratio, SMPTE (Society of Motion Picture and Television Engineers) color bars, a multiburst pattern, and a dual-frequency (1.25 and 7 MHz) signal. In addition, images were evaluated visually on a high-quality monitor. Ten disks were retained as controls. Forty disks were incubated at elevated temperatures for times ranging from three to seventy days. Four temperatures were chosen: 38, 45, 52, and 60°C (95, 113, 126, and 140°F). Two relative humidities, 40 and 60%, were used at each temperature. All disks were remeasured after incubation and the results compared.

Phase I Test Results

With the exception of one disk, which suffered condensation on part of its recording surface, all the disks played back satisfactory signals after incubation. The only significant change in measured outputs was found in the chrominance signal-to-noise ratio, and this was determined to be due to an eccentricity problem unrelated to incubation. Since no failures or measurable degradation were observed, the data provide no basis for inferring lifetime at ambient temperature.

Phase II Testing

A new set of 50 disks was recorded as before, with the exception that the frequencies used in the dual-frequency test were 939 kHz and 7.015 MHz from the chrominance test on Track 6. Forty disks were then incubated at 60, 68, 77, and 85°C (140, 154, 171, and 185°F) at 60% RH. Early analysis revealed that 77°C is hot enough to warp the jackets slightly and increase the curl of the media. Disks incubated at 85°C showed severe distortion of disks and media. Usable signals could be obtained from portions of these disks, however, and showed a loss of 0.4 to 3.6 dB from the dual-frequency test. This loss in signal, which is an average for the track, can be attributed to dropouts due to loss of head-media contact for part of each revolution of the disk.

Incubation was continued at the lower temperatures, and some disks from Phase I 60°C 60% RH were reincubated. One of these disks suffered condensation and was unusable: useful data were obtained, however, out to 133 days. In general, there was very little change observed in the various measurements. The measurement of signal output at 7 MHz proved to be the most sensitive indicator: changes of a few tenths of a dB were fairly reliably determined.

Results

Figures 1 to 4 show the changes in 7-MHz output as a function of incubation time for temperatures of 85, 77, 68, and 60°C, all at 60% RH. The spread in the data was treated by delineating the high and low limits in addition to the best fit. An output change of − 1 dB was chosen as the failure criterion in order to have a criterion within the range of the data; such a change would ordinarily be visually undetectable. While the data at the higher temperatures are somewhat suspect in that they may be due to physical changes in the support, the lower temperatures give some ground for confidence that chemical changes are being observed similar to what would be found over very long times at room temperature. At 60°C, for example, only two of the eleven data points lie more than 0.3 dB from the best-fit line.

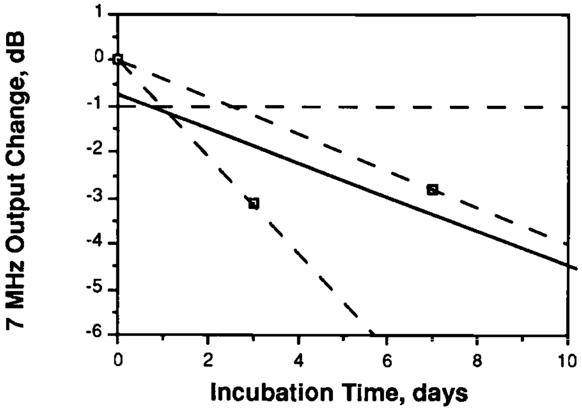

FIG. 1—*85°C incubation.*

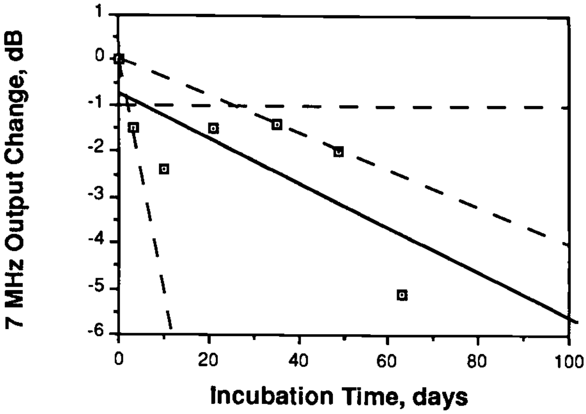

FIG. 2—*77°C incubation.*

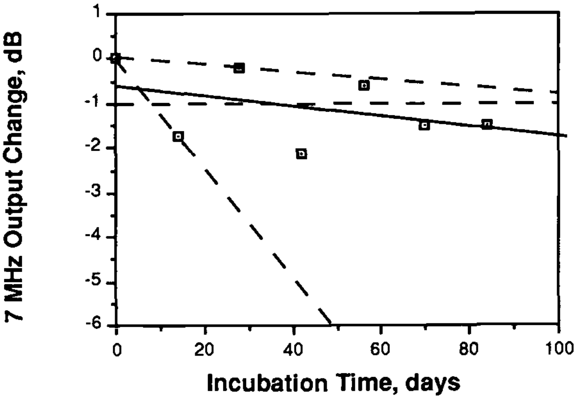

FIG. 3—*68°C incubation.*

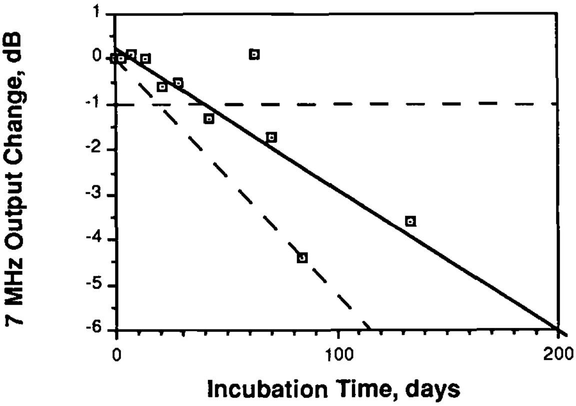

FIG. 4—*60°C incubation.*

Figure 5 results from plotting the high-limit, best-fit, and low-limit times from each temperature on a logarithmic scale as a function of reciprocal temperature. This is known as an Arrhenius plot and may be used to extrapolate to room temperature. The low-limit data extrapolate to 15 years, the best-fit data to 390 years, and the high-limit data to 275 000 years. It should be remembered that these times are estimates of storage time at room temperature and moderate humidity before a (visually undetectable) change of 1 dB at 7 MHz would be expected. Changes large enough to be visually noticeable would be expected to take several times as long.

Measurement Sensitivity

An appreciation for the sensitivity of this measurement technique can be derived from a consideration of the physical changes in the media sufficient to cause the observed signal output changes. Suppose all the change is due to an increase in the spacing between the media

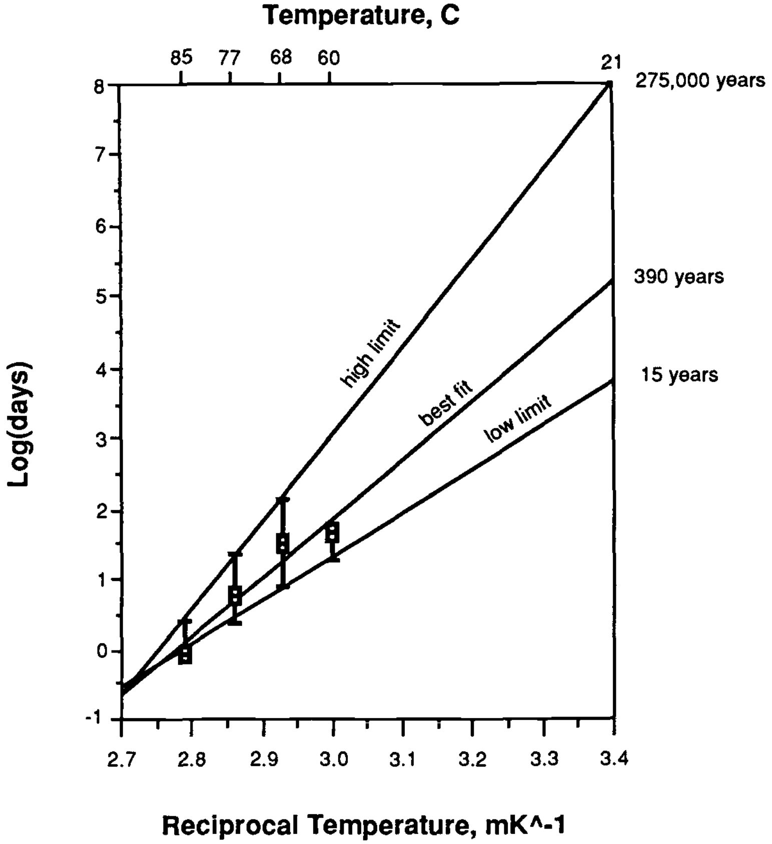

FIG. 5—*Arrhenius plot, 1 dB loss.*

and the playback head, such as could be caused by the growth of an oxide film on the magnetic particles. This change is given by the Wallace formula [7]

$$\text{spacing loss (dB)} = 54.6\ d/\lambda$$

where

d = the head-to-media spacing, and
λ = the recorded wavelength.

The wavelength for a signal recorded on tape or disk is found by dividing the linear speed of the medium by the frequency of the signal. For a 7-MHz signal recorded on SVF track six

$$\begin{aligned}\lambda &= (60\ \text{rev/s} \times 2\pi \times 19.5\ \text{mm})/(7 \times 10^6\ \text{cycles/s})\\ &= 0.001\ \text{mm}\end{aligned}$$

A loss of 1 dB therefore corresponds to 1/55 of 0.001 mm, which is a little less than 20 nm, or about 100 monolayers.

Acknowledgments

Thanks are due to David Kopperl of the Image Stability Technical Center for supervising the incubation of the disks and for consulting on experimental design and data interpretation; to James Elly of the Electronic Photography Division for the meticulous measurement of magnetic recording performance; and to K. Bradley Paxton for his encouragement to conduct this study.

References

[*1*] Welz, G., "Zur Problematik der Lagerung von Videomagnetbänden," *Fernseh- und Kino-technik,* Nr. 1/2, 1987, pp. 5–14.

[*2*] Wheeler, J., "Videotape Storage—How To Make Your Videotapes Last for Decades . . . or Centuries," *American Cinematographer,* Vol. 64, No. 1, January 1983, pp. 23–24.

[*3*] Wheeler, J., "Long-Term Storage of Videotape," *SMPTE (Society of Motion Picture and Television Engineers) Journal,* Vol. 92, No. 6, June 1983, pp. 650–654.

[*4*] Woodcock, R., "Video Life Spans," *Video,* June 1987, pp. 30–32.

[*5*] Alberty, R. A., *Physical Chemistry,* 6th ed., John Wiley & Sons, New York, 1983, p. 617.

[*6*] Video Technical Committee, "CPZ-250 Specification of Still Video Floppy Disc Systems," Electronic Industries Association of Japan, September 1987.

[*7*] Jorgensen, F., *The Complete Handbook of Magnetic Recording,* Tab Books, Blue Ridge Summit, PA, 1980, p. 82.

Allan S. Hadad[1] *and Patrick P. Pizzo*[2]

The Effect of Temperature, Humidity, and Silicon Content on the Oxidation of Fine Iron Particles

REFERENCE: Hadad, A. S. and Pizzo, P. P., **"The Effect of Temperature, Humidity, and Silicon Content on the Oxidation of Fine Iron Particles,"** *Corrosion of Electronic and Magnetic Materials, ASTM STP 1148,* P. J. Peterson, Ed., American Society for Testing and Materials, Philadelphia, 1992, pp. 53–67.

ABSTRACT: In this study, the oxidation and electrochemical corrosion of Fe-Si particles used in magnetic recording are investigated under controlled thermal and relative humidity conditions. The relative humidity, above a threshold value, dominates the oxidation behavior. Oxidation kinetics increase greatly above this threshold, and a portion of the exposed particle population becomes completely oxidized. X-ray diffraction data confirm the appearance of α-Fe_2O_3 in addition to the usual γ-Fe_2O_3 following exposure to high humidities. Greater silicon content increases the threshold humidity, above which rapid degradation in magnetic properties occurs.

KEY WORDS: oxidation, electrochemical corrosion, magnetic particles, iron particles, archival stability, relative humidity, silicon, magnetic moment, degradation kinetics, passivation

The most significant trend observed in the magnetic tape industry over the last 40 years has been the storage of more recorded information in less space through greater track densities (primarily mechanical improvements) and in more flux transitions per unit length due to improvements in magnetic particle and magnetic head technology. Originally, magnetic recording was done using γ-Fe_2O_3 particles that averaged 0.75 μm in length by 0.09 μm in diameter with a coercivity of 270 Oe. The specific magnetic moment, σ_s, for these particles is 73.5 EMU/g [electromagnetic units/g ($A \cdot m^2/kg$)] [*1*]. In order to achieve greater flux changes per unit length, magnetic particles have been made smaller (less than 0.25 μm in length and 0.04 μm in diameter). In order to improve the volumetric efficiency of the particles, a change was made from γ-Fe_2O_3 to pure iron (α-Fe phase), eliminating oxygen that had occupied much of the crystal volume. The coercivity of these fine iron particles is as high as 1500 Oe, and their magnetic moments are as high as 130 EMU/g.

Alpha iron particles used for magnetic recording are prepared through a series of dehydration and reduction steps of α-$Fe_2O_3 \cdot H_2O$, resulting in acicular, polycrystalline body centered cubic (bcc) α-Fe particles that are single magnetic domains. Since fine iron particles are pyrophoric by nature, stabilization processes had to be developed in order for iron particles to be considered as a viable recording medium for long-term archival (i.e., 25+ years) information storage. The primary means to establishing stability is through passivation or controlled oxidation of the iron particle's surface.

The usual technique of producing the protective layer is through reoxidation of the iron

---

[1] Manager, Formulation Development, Ampex Recording Media Corporation, Redwood City, CA 94063.

[2] Professor, Department of Materials Engineering, San Jose State University, San Jose, CA 95148.

particle's surface after synthesis starting with a mixture of 0.1% O_2 and 99.9% N_2. The oxygen content is slowly increased to 20% (the composition of air) so as to maintain the reaction at room temperature. This results in a particle that is stable in air provided it is not subjected to any form of: (1) mechanical abuse that could disturb the outer layer; or (2) source of heat that would initiate combustion. Figure 1 is a bright field transmission micrograph (TEM) of typical magnetic iron particles that shows the passive layer.

The nature of the passive layer on iron particles has been found to consist of either Fe_3O_4, γ-Fe_2O_3, or a mixture of the two [*2*]. Identification of which iron oxide is present by X-ray diffraction is difficult because the patterns of Fe_3O_4 and γ-Fe_2O_3 are very similar. The two oxides are actually the final products of a series of continuous solid solutions having the spinel structure with an increasing deficiency of iron ($Fe_3O_4 \rightarrow \gamma$-$Fe_2O_3$) [*3*]. The thickness of the passivation (or total) oxide layer is typically about 3.0 nm [*4*]. Mossbauer spectra of passivated iron particles does not show the characteristic lines of any of the possible oxide species present. The broad background of the passivated iron sample indicates the presence of the oxide in a magnetically or crystallographically ill-defined state [*5*]. The average valency of the iron in the passive layer was determined by Mossbauer to be 2.8 in a study by Makishima et al. [*5*], implying a mixture of Fe_3O_4 and γ-Fe_2O_3. The condition of passivity slows down the oxidation of iron, but the formation of the iron-oxide layer around metallic iron particles does not preclude further oxidation. The continued stability of iron particles is controlled by the integrity of the oxide layer and the kinetics of diffusion of iron ions through it. A pure iron particle with a surface oxide layer, if left long enough or exposed to elevated temperature, will continue to oxidize as iron ions migrate to the surface and react with ambient oxygen [*6*].

In a study by Lee et al. [*7*], iron particles stored at 50°C under nitrogen for one month began

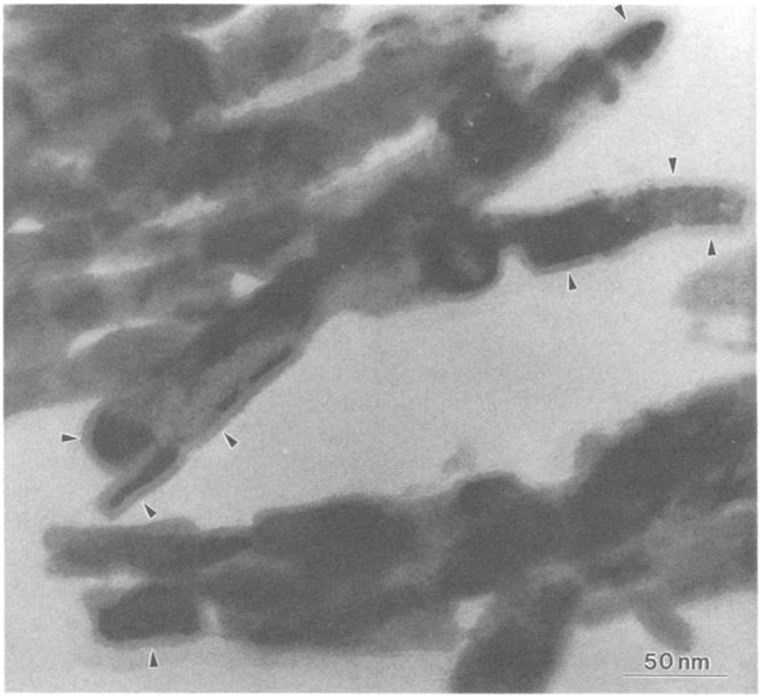

FIG. 1—*Bright-field TEM of magnetic iron particles.*

to burn almost instantly when exposed to air. Auger spectroscopy showed an increase in the surface iron concentration with time when particles were heated in a vacuum to 300°C.

Since iron particles used for magnetic recording are small, additional oxidation has a direct impact on performance, especially where archival storage of recorded information for long periods of time is important. Further stabilization chemistry/processes had to be developed to guarantee that iron particles could be considered as a viable long-term recording medium.

In an effort to retard the diffusion of iron ions through the oxide layer, other elements such as silicon, aluminum, and chromium have been added to the base iron to promote more dense scale formation or to alleviate some of the nonstoichiometric behavior of the oxide or both [*8*].

The effect of adding silicon to iron to decrease its high temperature oxidation rate has been well documented [*9,10*]. It has been shown that a silicon-rich oxide scale forms limiting subsequent diffusion of iron ions to the surface due to the fact that the diffusion coefficient of iron in SiO_2 is much lower than it is for iron through any of the iron oxides [*8*].

The presence of water vapor has been shown to disrupt the passive layer, subsequently increasing the oxidation rate of the iron [*8*]. The primary cause is through the establishment of electrochemical corrosion. The oxide shell is no longer protective; it is penetrated by moisture and electrolytic cells are formed. The oxygen-rich oxide layer will act as the cathode, and the iron will be the anode. This effect of electrochemical corrosion is much more devastating to the iron than chemical corrosion. Chemical corrosion can result in the formation of an adhered scale leading to the condition of passivity.

This paper presents the results of a study undertaken to examine the degradation in magnetic properties as a function of both temperature and humidity on silicon-containing iron particles between 50 to 120°C and 3 to 89% relative humidity [*11*]. The methodology to which experimental data was collected and analyzed leading to predictive capability is also presented.

Experiment

To study the effect of temperature and humidity on the stability of passivated iron particles as a function of silicon content, three particle batches were prepared through reduction of α-$Fe_2O_3 \cdot H_2O$ and repassivation. The silicon levels studied were 0.81, 0.95, and 1.12% by weight. The entire experimental procedure is described in Ref *11*.

The prepassivated particles were exposed to the various environmental conditions as shown in Table 1. The temperature/humidity conditions were maintained inside closed glass dessicatiors placed in an air circulation oven that could maintain temperature within ± 1°C. The dessicators contained either $CaCl_2$ or water to create a nearly dry environment or nearly saturated conditions, respectively. No condensation was observed. Intermediate humidity conditions were obtained using saturated solutions of NaBr or KI. Humidity was continuously monitored using an Abbeon hydrometer inside the treatment containers. Approximately 1 g of iron powder was placed in separate glass vials corresponding to the number of exposure times investigated per temperature/humidity condition. The vials were then placed into the exposure environment following a 24-h equilibration period. In this way each exposure time specimen could be removed with minimum influence on the other specimens, and each was small enough so that exposure within the specimen was uniform. After the particles were exposed, they were placed in a closed desiccator with $CaCl_2$ for 24 h at 20°C before magnetic measurements were made.

The magnetic properties of the specimens were determined using a vibrating sample magnetometer at an applied field of 7500 G. The coercivity (H_c), squareness ratio (B_r/B_s), and specific magnetic moment (σ_s) were measured.

Powder X-ray diffraction (XRD) was used to relate any changes observed in the magnetics

TABLE 1—*Environmental exposure conditions for silicon-containing iron particles.*

		Rate of Magnetic Moment Loss, EMU/g-s$^{0.5}$		
Temperature, °C	Humidity, % Relative	0.81%	0.95%	1.12% Si
50	18	...	−0.0110	−0.0071
50	52	−0.0627	−0.0385	−0.0038
50	66	−0.0439	−0.0452	−0.0082
50	89	−0.2640	−0.2111	−0.0103
70	7	−0.0094	−0.0128	−0.0133
70	47	−0.0308	−0.0281	−0.0110
70	59	−0.0537	−0.0342	−0.0100
70	74	−0.2432	−0.1952	−0.0286
80	7	...	−0.0203	...
80	77	...	−0.4111	...
90	9	−0.0184	−0.0313	−0.0240
90	74	−0.5694	−0.4715	−0.0492
105	4	−0.0320	...	−0.0387
120	3	−0.0503	...	−0.0635

of the samples (after exposure to various environmental conditions) to the nature of the oxide formed. A copper K_α X-ray source operated at 50 kV/22 mA was used with a monochromater to remove the effects of unwanted radiation.

A Zeiss EM10C/CR transmission electron microscope operated at 100 kV was employed in an attempt to resolve internal structure and determine if any morphology changes could be observed.

As stated earlier, the oxidation process of iron particles is diffusion controlled. The increase in oxide thickness is determined by how fast iron ions can migrate to the surface (passivation kinetics). It is assumed that the reduction in σ_s is proportional to the oxide thickness; therefore, Fick's second law of diffusion for concentration-dependent systems can be applied

$$Y^2 \cong D\,t$$

where

Y = diffusion distance in cm
D = diffusivity in cm^2/s, and
t = diffusion time in s.

For this analysis, the data are plotted as specific magnetic moment versus the square root of time. The resultant slope is therefore the rate of degradation expressed as EMU/g-s$^{0.5}$ for a given temperature and humidity condition.

Analysis of the interactive effects of temperature, humidity, and percent silicon on the degradation of magnetic properties of iron particles were determined using XSTAT, a statistical experimental design package run on an IBM AT compatible computer. The factor settings that were input into the computer were those found in Table 1. This represents a modified three-variable, three-level factorial experiment. The characteristic measured was the $\log_{10}$ of $\sigma_s/s^{0.5}$ (rate of degradation).

The procedure of data analysis consists of selecting an initial mathematical model (usually a quadratic equation to analyze interaction and curvature effects of the form $Y = C_0 + C_1X_1 + C_2X_2 \ldots + C_{12}X_1X_2 + C_{13}X_1X_3 \ldots. + C_{11}X_{12} + C_{22}X_{22} \ldots..$) where C_n is a constant and X_n is the level setting of the respective factor. The model is then used to "fit" the data.

Results and Discussion

Dry Conditions

Oxidation rate studies are generally done as a function of temperature without reference to humidity. It is assumed that the ambient humidity present is (1) either too low to have any effect, especially at the high temperatures usually studied, or (2) constant at all test conditions so that any change in oxidation rate is assumed to be only a function of the exposure temperature.

The first series of oxidation rate experiments were run at the "dry" conditions for the selected temperatures. Oxidation at various temperatures allowed generation of σ_s versus time curves for iron particles containing 0.81, 0.95, and 1.21% silicon. Figure 2 shows the change in specific magnetic moment with time for the 1.12% silicon sample at various temperatures. As temperature increased, the rate of degradation of σ_s also increased. Differences in the rate of degradation at a given temperature between the three samples studied containing different amounts of silicon are slight, indicating that the iron particles all behave the same at low humidity, independent of Si content or initial σ_s value [*14*]. If the hypothesis offered by Sherwood concerning the formation of the silicon oxide barrier limiting transport of Fe through the passive layer applied, greater differences should have been observed. Either the amount of silicon present at the scale-Fe interface is insufficient to form a continuous protective barrier, or the diffusion rate at the low temperatures studied is too slow for a barrier oxide of predominantly silicon oxide to form.

Activation energies for degradation of the 0.81, 0.95, and 1.12% silicon-in-iron powder samples were determined to be 0.383, 0.263, 0.333 eV, respectively, when the rates of degradation

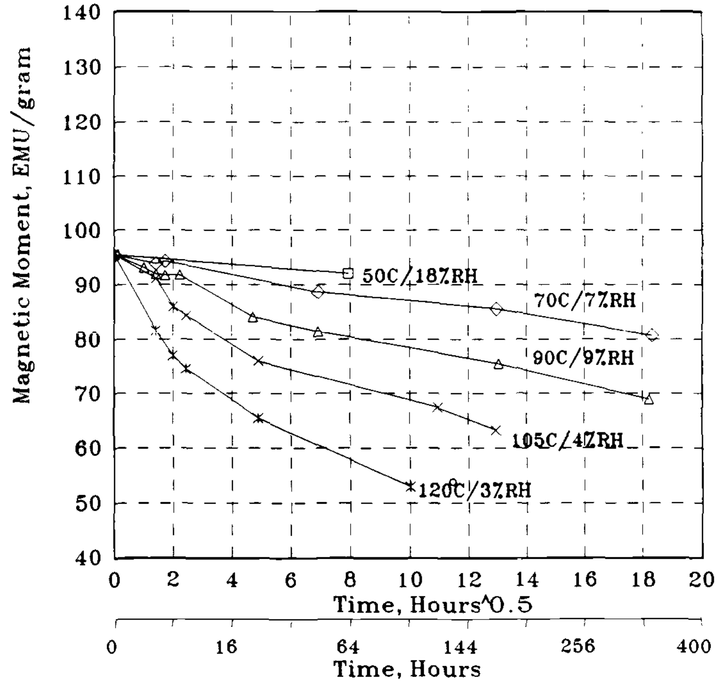

FIG. 2—*Magnetic moment versus time as a function of temperature at low humidity for 1.12% silicon in iron.*

were plotted against the absolute temperature (Arrhenius plot). Thus, the energy requirement to initiate the oxidation reaction for the various Si-contents is essentially the same, and all degrade at essentially the same rate as a function of temperature. However, these activation energies are only 10% of the value for diffusion of iron through any of the possible iron oxides [*12*]. The implication is that the primary mechanism for the loss in magnetic properties is not due to lattice diffusion but rather diffusion along some short circuit path such as linear or planer defects present in the oxide shell. The presence of considerable energy in the form of strain (i.e., atomic mismatch at the metal/oxide interface and grain boundaries, a high surface area to volume ratio, twinning, etc.) may be involved in the enhanced diffusion kinetics. A transition to grain-boundary diffusion is not a sufficient explanation for the loss in magnetic properties at temperatures between 50 and 120°C at low humidity. If grain boundary diffusion controlled the passivation kinetics, the activation energy would be expected to be half of the value for bulk diffusion.

Moisture Effects

Magnetic moment loss is shown as a function of humidity at constant temperature (70°C) for the 0.81, 0.95, and 1.12% silicon samples in Figs. 3, 4, and 5, respectively. As the humidity increases, the rate at which the magnetic moment degrades increases markedly with decreasing Si content. Degradation is most rapid for the 0.81% Si-containing iron particles. The sample containing 0.95% silicon is more resistant to degradation until the relative humidity is above 59% at 70°C. Finally, the sample containing 1.12% silicon is the most resistant to degradation,

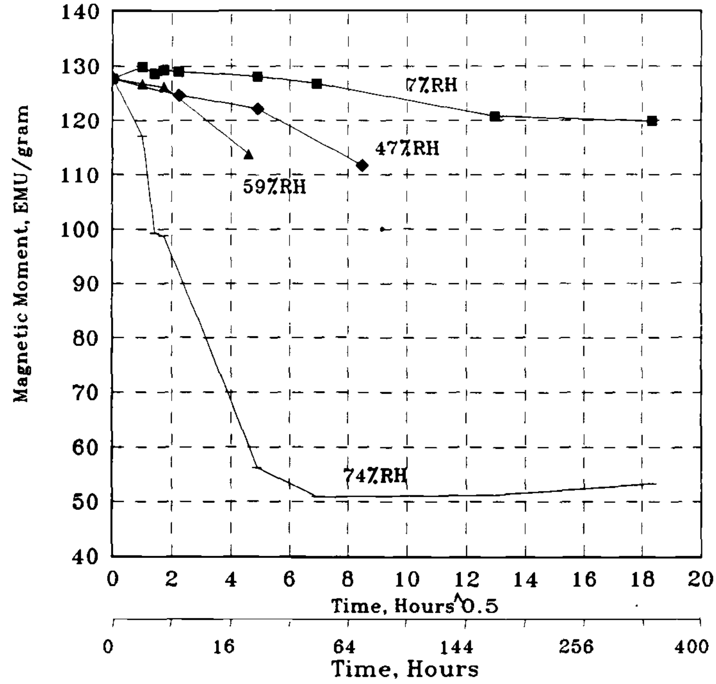

FIG. 3—*Magnetic moment versus time as a function of relative humidity for 0.81% silicon in iron at 70°.*

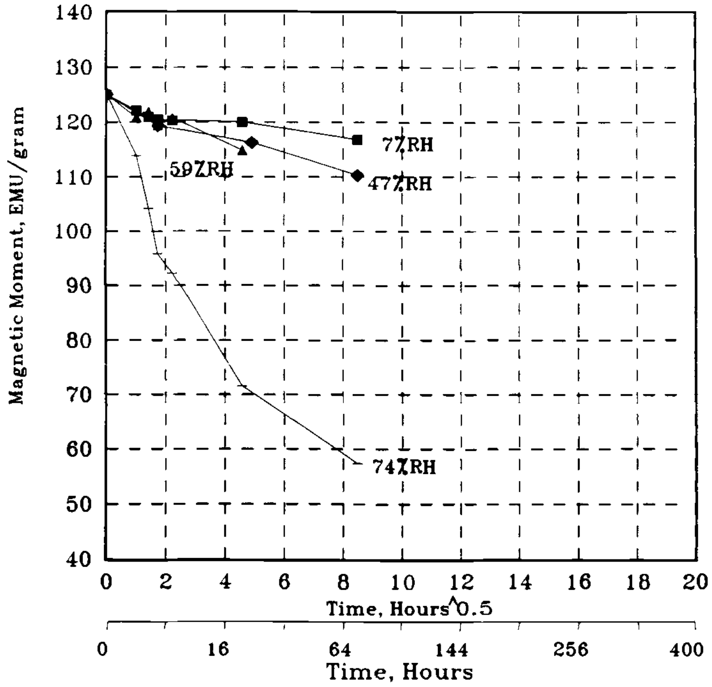

FIG. 4—*Magnetic moment versus time as a function of relative humidity for 0.95% silicon in iron at 70°C.*

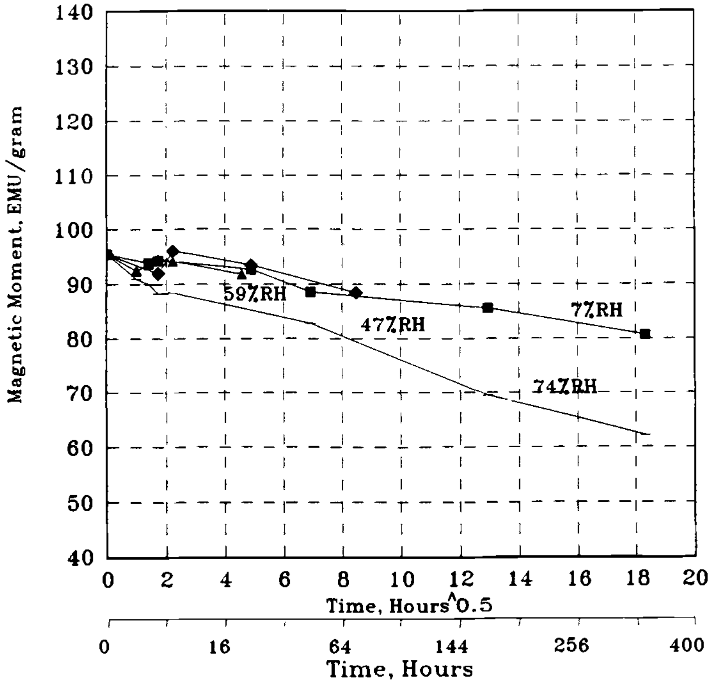

FIG. 5—*Magnetic moment versus time as a function of relative humidity for 1.12% silicon in iron at 70°C.*

exhibiting almost the same rate of loss at 7% relative humidity as it does at 74% relative humidity.

The apparent threshold value of humidity that is observed at the 0.95% silicon level and possibly the 1.12% level, above which the degradation rate increases very rapidly, is consistent with results by Uhlig [*13*], who reported that a critical humidity exists below which corrosion is negligible. For steel, copper, nickel, and zinc, the critical value is between 50 to 70% relative humidity. The time of exposure must also be considered in defining the moisture threshold.

As silicon content increases, the critical humidity (the humidity where rapid degradation occurs at a given temperature) also increases. However, the degradation ceases at a σ_s value of 50 to 60 EMU/g for the 0.81% silicon sample (Fig. 3). The trend appears to to the same (a saturation limit) for the 0.95 and 1.12% Si particles also. As indicated earlier, the σ_s value for γ-Fe_2O_3 is 73.5 EMU/g. A calculation done by Kishimoto [*4*] using the occupation value of iron particles with the surrounding iron oxide layer based on TEM micrographs established the σ_s of the oxide to be about 40 EMU/g. This calculation assumed the particles to be cylinders, ignored end effects, and assumed that the oxide phase was continuous. Based on the saturation limit of <50 EMU/g for the high humidity exposures of this study, a significant volume fraction of the iron particles must have been oxidized to a nonmagnetic form. TEM and XRD data will be presented which supports this hypothesis.

It is also obvious in Figs. 3, 4, and 5 that a difference exists in the initial magnetic moments for the iron particles. As silicon content is increased from 0.81 to 0.95% by weight, there is little change in the initial σ_s. However, when the silicon content has been increased to 1.12%, the decrease in the starting value of σ_s is much more pronounced. The effect of silicon on the magnetics appears to be greater than can be explained by simple dilution alone. An explanation for this phenomenon will be drawn from the X-ray data.

In an effort to study the nature of the passive layer, X-ray diffraction patterns (XRD) were obtained [*11*]. The diffraction patterns for the as-received powder samples are interpreted as a mixture of α-Fe and oxide of iron (either γ-Fe_2O_3 or Fe_3O_4 or both). Figure 6 is the XRD pattern of the as-received 0.81% silicon sample. The ratios between the oxide peaks and the α-Fe peaks for the 0.81 and 0.95% silicon-in-iron particles were seen to be the same, indicating essentially the same degree of oxidation for the as-received samples. However, the 1.12% silicon as-received sample was found to be oxidized (prepassivated) to a greater extent due to greater reactivity during the passivation step immediately following reduction from the precursor. This would explain the lower initial σ_s value for the high Si-content particles.

Following exposure to 90°C/9% relative humidity for 332 h, the intensity of the iron peaks [(110),(220)] decreased and the intensity of the oxide peaks increased for all three silicon contents. The identity of the mixed oxide remains the same as the as-received sample.

The XRD pattern (Fig. 7) of the 0.81% silicon exposed to 90°C/74% relative humidity for 332 h shows the presence of the same oxide phase found in the as-received sample (Fig. 6), only in much greater quantity. In addition, there is evidence of α-Fe_2O_3 and $FeSi_2$. The presence of these two nonmagnetic species offers an explanation as to why the specific magnetic moment value drops below the values for either γ-Fe_2O_3 or Fe_3O_4 magnetic oxides.

Reactions that occur with iron in the presence of both moisture and air (oxygen) are

$$2Fe + 2H_2O + O_2 \rightarrow 2Fe(OH)_2$$
$$2Fe(OH)_2 + H_2O + 1/2\ O_2 \rightarrow 2Fe(OH)_3$$

where $2Fe(OH)_3$ is also expressed as $Fe_2O_3 \cdot 3H_2O$ (hydrated, nonmagnetic alpha-hematite). The reason that the kinetics of degradation of the iron in the presence of moisture is so much faster than in air alone may be related to the fact that the additional partial pressure of water vapor is altering the defect concentration in the oxide layer, making it easier to transport iron

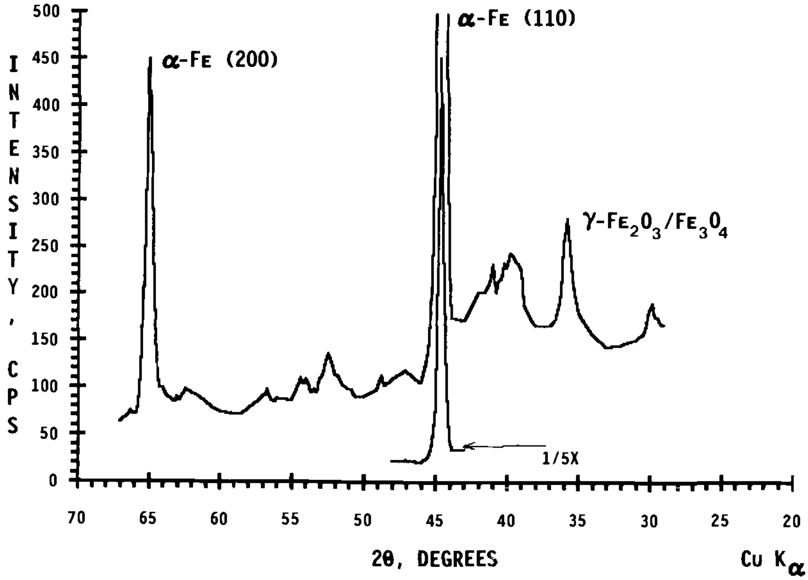

FIG. 6—*XRD pattern of as-received iron particles containing 0.81% silicon.*

ions to the surface. Additionally, the electric field present due to the formation of an electrical double layer at the surface as oxygen and water ionize may provide an additional driving force for the iron ions to migrate. This assumes that a continuous moisture layer exists which supports electrochemical reactions as suggested by Rice et al. [*14*].

Figure 8 is a X50 000 bright-field TEM micrograph of the specimen containing 0.81% sili-

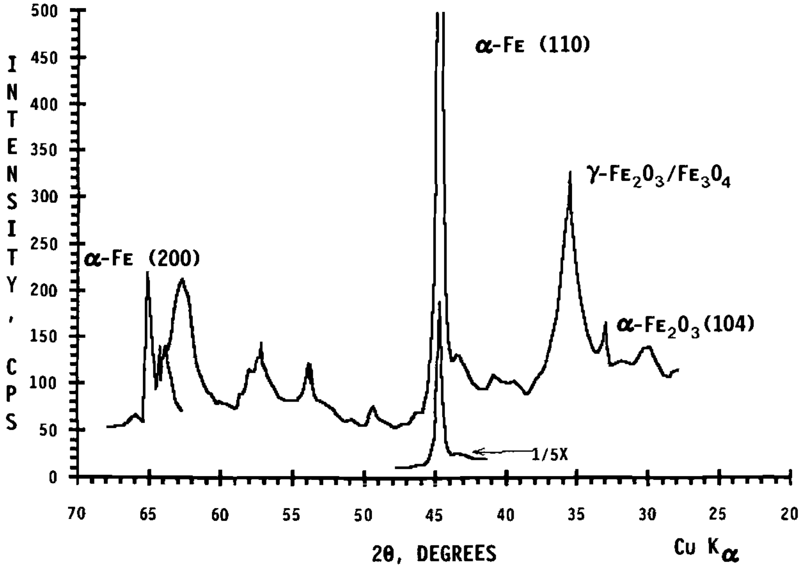

FIG. 7—*XRD pattern of iron particles containing 0.81% silicon exposed to 90°C/74% relative humidity/332 h.*

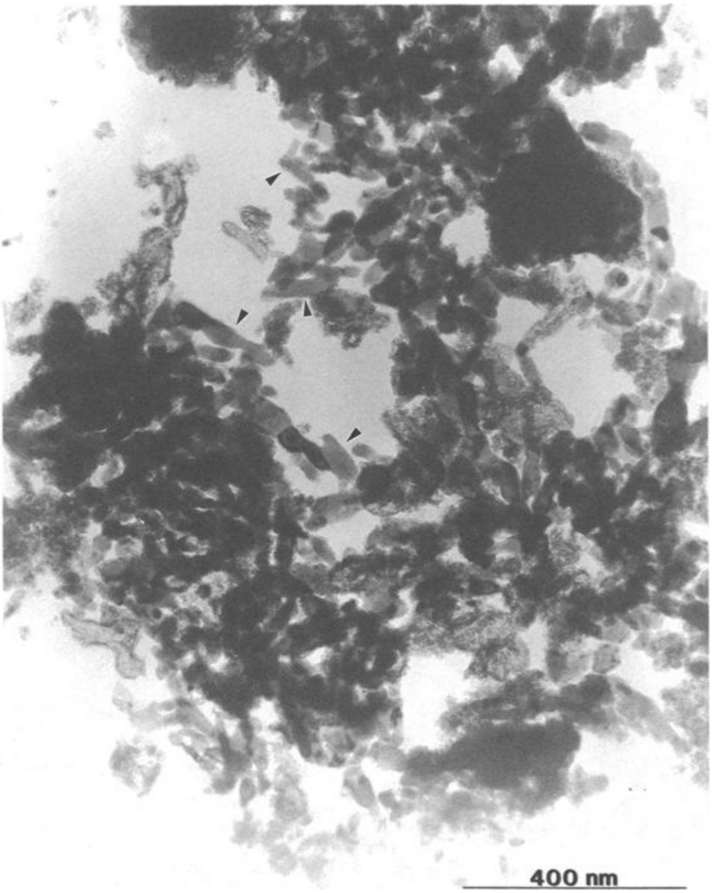

FIG. 8—*Bright-field TEM of iron particles containing 0.81% silicon after exposure to 90°C/74% relative humidity/5 h at X50 000.*

con and exposed to 90°C/74% relative humidity for 5 h. This corresponds to the point in Fig. 3 where the magnetic degradation has reached the saturation limit. Examination of the micrograph reveals a number of particles with constant, light contrast throughout, indicating complete oxidation of the central iron core. Other particles with a visible oxide shell and an iron core apparently are not affected by the exposure and account for higher coercivity values than would be observed if the conversion of all the particles to γ-Fe_2O_3 was complete.

Interaction of Temperature, Humidity, and Silicon

The three parameters of this study (temperature, percent relative humidity, and percent silicon content) interactively influence the degradation of the iron particles. Thus, statistical analysis was performed to quantify the contribution of each variable and present it in a manner that could be easily visualized. The measured characteristic was the $\log_{10}$ of the degradation rate in specific magnetic moment (EMU/g-$s^{0.5}$) as derived from the results of the experimental matrix shown in Table 1. The design predictor equation determined using XSTAT is as follows

$$\begin{aligned}\log_{10}(\text{rate}) = & -14.76 + 25.26(X_{\text{Si}}) + 0.04176(X_{\text{RH}}) \\ & + 0.00015(X_{\text{T}} \cdot X_{\text{RH}}) - 0.05963(X_{\text{Si}} \cdot X_{\text{RH}}) \\ & + 0.000068(X_{\text{T}})^2 - 12.49(X_{\text{Si}})^2 \\ & + 0.000219(X_{\text{RH}})^2\end{aligned}$$

where

X_{Si} = concentration of silicon in weight percent,
X_{T} = temperature in degrees Celsius, and
X_{RH} = percent relative humidity.

The percent variance explained (how well the regression equation predicts the data) was 96.03%, so the model can be considered as quite good. Solving the predictor equation via the computer produces two-dimensional contour plots of percent relative humidity versus temperature at constant silicon content. The values of constant degradation rate were transferred to a psychrometric chart (Figs. 9, 10, and 11) so the relationships between absolute humidity

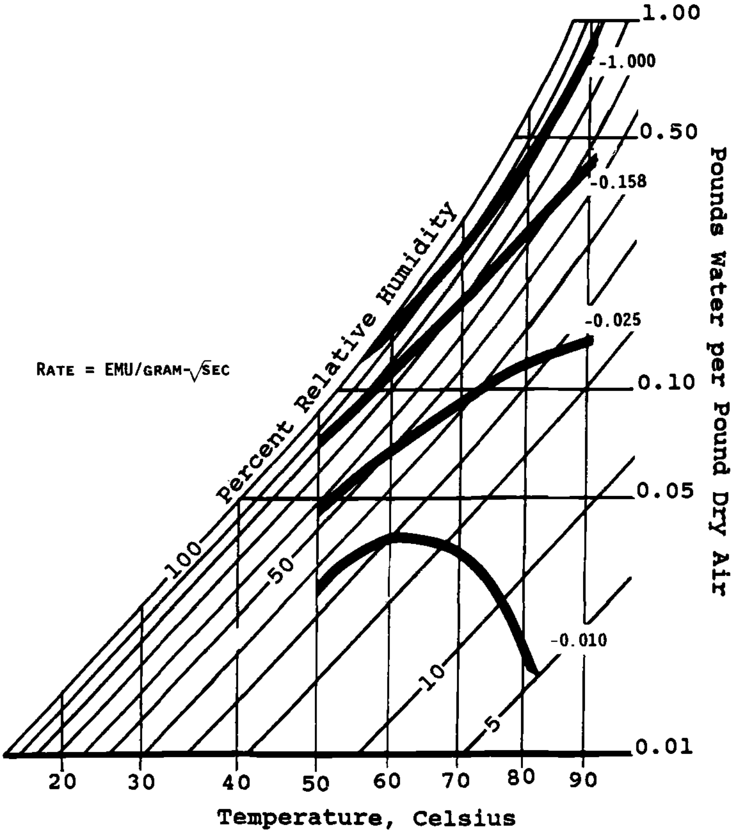

FIG. 9—*Contour plots of magnetic moment degradation rate as a function of temperature, humidity, and 0.81% silicon in iron particles.*

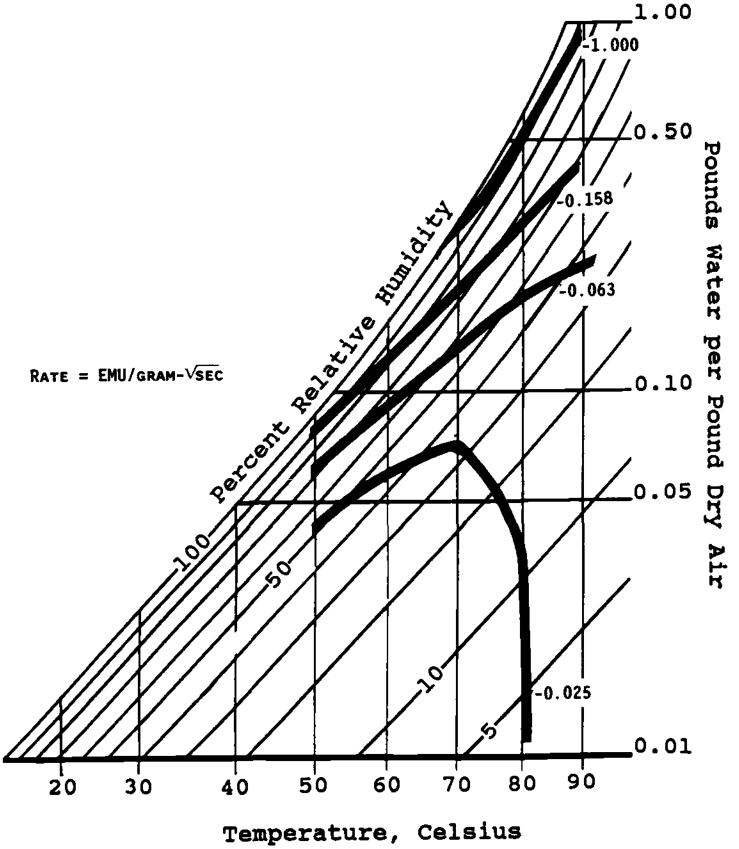

FIG. 10—*Contour plots of magnetic moment degradation rate as a function of temperature, humidity, and 0.95% silicon in iron particles.*

(expressed as pounds of water per pound of dry air), percent relative humidity, and temperature as a function of silicon content could be observed. The nonlinear degradation behavior becomes very obvious when presented in this manner. A rate value can be taken from the contour plots for a given temperature, humidity, and percent silicon content and be used to determine how long it would take for the magnetic moment to degrade to some predetermined value.

For a constant absolute humidity (above the critical value, depending on silicon content), increasing temperature will cause the degradation rate to decrease. It appears that relative humidity is the controlling factor. This is consistent with results presented by Rice et al. [*14*] where a correlation was made between corrosion rate and relative humidity of the form: Rate $= Ae^{(b\%\mathrm{RH})}$, where A and b are constants, for the atmospheric corrosion of cobalt. Rice concludes that the corrosion rate was actually proportional to the thickness of the adsorbed water layer on the surface of his specimens. The higher the relative humidity, the thicker the adsorbed layer, hence the faster the corrosion rate.

Incorporating Rice's equation with an expression for a thermally activated process yields an expression of the form

$$\text{Rate} = Ae^{(b\%\mathrm{RH})}e^{-(Q/RT)}$$

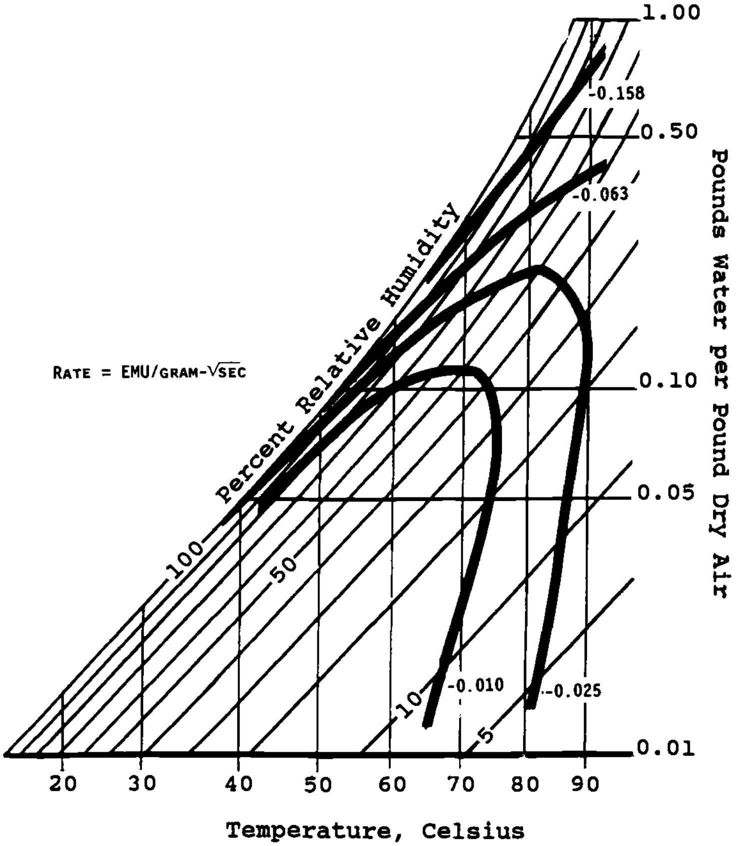

FIG. 11—*Contour plots of magnetic moment degradation rate as a function of temperature, humidity, and 1.12% silicon in iron particles.*

where

Q = the activation energy for diffusion,
R = the ideal gas constant, and
T = absolute temperature.

The behavior observed in the contour plots (Figs. 9–11) follows an expression of this form where at low humidity temperature is the controlling factor; then a transition occurs where humidity effects prevail. It would be expected that at low relative humidity the constant degradation rate contour lines seen in Figs. 9–11 should become vertical as is the case in Fig. 10. Figure 11 does not exhibit this behavior, probably due to the model not completely describing the degradation behavior. A better fit would be expected away from the experimental factor space boundaries (i.e., towards the center of the design). However, it is obvious that special precautions should be taken when attempting to predict long-term, low-temperature behavior based on high-temperature data with a system that is humidity sensitive. Actual archival stability could be less than expected unless humidity control is considered. The value of the statistical analysis to the interpretation of oxidation behavior is clearly evident.

Conclusions

This study has shown the effects of percent silicon content, temperature, and percent relative humidity on prepassivated fine iron particles used for magnetic recording. It was observed that silicon had very little effect on the specific magnetic moment of the as-received iron between 0.81 and 0.95% by weight. However, at 1.12% silicon content the magnetic moment was much lower than would be expected by dilution alone. X-ray diffraction revealed a greater degree of oxidation in the as-received powder sample, probably due to greater reactivity of the α-Fe during the prepassivation step. The nature of the oxide was determined by X-ray diffraction to be a mixture of magnetic γ-Fe_2O_3 and Fe_3O_4 oxides.

When the iron particles were exposed to various temperatures between 50 and 120°C at very low humidity, it was observed that the degradation rates were not affected by either the silicon content or the initial value of the magnetic moment. The mechanism of degradation was attributed to diffusion of iron ions through the oxide matrix via short circuit paths such as grain boundaries or other defects. The activation energy of this process was determined to be an order of magnitude less than that for normal lattice diffusion. X-ray diffraction indicated the oxide structure was the same as the as-received samples. TEM micrographs revealed that the oxide layer grew thicker, leading to a condition of passivity.

It was shown that for a given temperature there exists a critical relative humidity value above which the degradation rate of magnetic moment increases markedly. The presence of silicon appears to increase the critical humidity value at which rapid degradation occurs. When the magnetic moment degrades to 50 to 60 EMU/g, it remains constant for additional exposure time.

X-ray diffraction indicates the presence of α-Fe_2O_3 (nonmagnetic phase), which may explain magnetic moment values less than expected if the oxidation product was all γ-Fe_2O_3. The formation of the α-Fe_2O_3 phase is attributed to a change in mechanism from chemical oxidation to electrochemical corrosion for the higher relative humidity exposures. The electrochemical processes result in complete oxidation of some of the iron particles rather than a gradual growth of the oxide shell, while others remain relatively unaffected. This was revealed by TEM.

A parametric expression has been proposed to relate silicon content, temperature, and humidity to the initial rate of specific magnetic moment degradation for the iron particles used in this study.

Acknowledgments

The authors wish to thank the following from Ampex Recording Media Corporation: Irving Wolf for his valuable advice, Ashok Jhingan for the TEM work, and Jiri Petovsky for providing the samples that were studied.

References

[*1*] Marusak, L. A. Walker, P. L., Jr., and Mulay, L. N., "The Magneto-kinetics of Oxidation of Pyrite (FeS_2)," *IEEE Transactions on Magnetics,* Vol. MAG-12, No. 6, November 1976, p. 889.

[*2*] van Diepen, A. M., Vledder, H. J., and Langereis, C., "The Nature of the Passivating Oxide Layer on Iron Powder," *Applied Physics,* Vol. 15, 1977, pp. 163–166.

[*3*] Davies, D. E. and Evans, V. R., "The Identity of the Cubic Oxide Present in Films on Iron," *Journal of the Chemical Society,* 1956, p. 4373.

[*4*] Kishimoto, M., Kitahata, S., and Amemiya, M., "Morphology and Magnetic Properties of the Iron Oxide Layer Formed on Iron Acicular Particles," *IEEE Transactions on Magnetics,* Vol. MAG-22, No. 5, September 1986, pp. 732–734.

[*5*] Makishima, A., Yamamoto, Y., and Watanabe, K., "Characterization of the Surface Oxide Layer

on Iron Particles for Magnetic Recording by Mossbauer Spectroscopy," *Bulletin of the Chemical Society of Japan,* Vol. 63, January 1990, p. 150.

[*6*] Kaito, C., Fujita, K., and Naiki, T., "Electron Microscopic Observation of Fine Iron Smoke Particles," *Japan Journal of Applied Physics,* Vol. 9, 1970, p. 151.

[*7*] Lee, T.-H. D., Hu, S., and Madulid, N., "Stability Studies of Iron Particle," *IEEE Transactions on Magnetics,* Vol. MAG-23, No. 5, September 1987, p. 2881.

[*8*] Sherwood, W. J., Jr., "The Effect of Water Vapor on the Oxidation Behavior of Dilute Iron-Silicon Alloys," Ph.D. thesis, Rensselaer Polytechnic Institute, Troy, NY, December 1986.

[*9*] Svedung, I. and Vannerberg, N.-G., "The Influence of Silicon on the Oxidation Properties of Iron," *Corrosion Science,* Vol. 14, 1974, p. 391.

[*10*] Ban, T., Bohnenkamp, K., and Engell, H.-J., "The Formation of Protective Films on Iron Silicon Alloys," *Corrosion Science,* Vol. 19, 1979, p. 283.

[*11*] Hadad, A. S., "The Effect of Temperature, Humidity and Silicon Content on the Oxidation of Fine Iron Particles," master's thesis, San Jose State University, San Jose, CA, May 1990.

[*12*] Porter, D. A. and Easterling, K. E., *Phase Transformations in Metals and Alloys,* Van Nostrand Reinhold, U.K., 1981, p. 78.

[*13*] Uhlig, H. H., *Corrosion and Corrosion Control,* 3rd ed., John Wiley and Sons, Inc., New York, p. 173.

[*14*] Rice, D. W., Phipps, P. B. P., and Tremoureux, R., "Atmospheric Corrosion of Cobalt," *Journal of the Electrochemical Society,* Vol. 126, No. 9, September 1979, pp. 1459–1466.

Andrew S. Kim,[1] *Floyd E. Camp,*[1] *and Steve Constantinides*[2]

Corrosion Mechanism of Nd-Fe-B Magnets in Humid Environments

REFERENCE: Kim, A. S., Camp, F. E., and Constantinides, S., "**Corrosion Mechanism of Nd-Fe-B Magnets in Humid Environments,**" *Corrosion of Electronic and Magnetic Materials, ASTM STP 1148,* P. J. Peterson, Ed., American Society for Testing and Materials, Philadelphia, 1992, pp. 68–79.

ABSTRACT: Although Nd-Fe-B magnets exhibit outstanding magnetic properties, they have suffered from poor corrosion resistance in humid air. Because of this, various problems occur such as degradation of magnetic properties and/or contamination of the magnetic circuits. The corrosion rate of Nd-Fe-B magnets was found to vary with O, C, and N contents and to reach its minimum when these elements are within the range of: O = 0.6 to 1.2%; C = 0.05 to 0.15%; and N = 0.05 to 0.10%. To understand the corrosion mechanism of Nd-Fe-B magnets and the effects of these elements on corrosion resistance, various Nd-Fe-B magnets were metallographically examined. The corrosion resistance of Nd-Fe-B magnets is closely related to the microstructure, which is determined by controlling the minor elements such as O, C, and N. When the oxygen or the carbon content is low, the alloy forms a thick Nd-rich phase (α-Nd or α-Nd and Nd-oxide) on the grain boundaries. As oxygen and carbon contents increase, the Nd-rich phase at the grain boundaries becomes thinner and agglomerates into the triple junction. As oxygen content increases, the α-Nd changes to the Nd-oxide. This microstructural change may be responsible for improving the corrosion resistance. A small increase in N content further improves corrosion resistance.

KEY WORDS: Nd-Fe-B magnet, corrosion, corrosion resistance, corrosion mechanism, humid environment, autoclave test, Nd-rich phase, α-Nd, NdO_x, Nd_2O_3, grain boundary, stabilization, carbon, nitrogen, oxygen, coating

Since rare earth permanent magnets were introduced in 1965, there has been significant improvement in magnetic properties by modification of alloy compositions and processes. Among these materials, Nd-Fe-B magnets have assumed an important position due to their outstanding magnetic properties [*1,2*]. However, corrosion has been a problem with Nd-Fe-B magnets because the phases rich in rare earth elements are easily oxidized in the air, especially in humid air [*3,4*]. Corrosion of Nd-Fe-B magnets in service can degrade their magnetic properties and also produce contaminants that can be detrimental to the magnetic circuits in which the magnets are used. Therefore, much effort has been made to improve the corrosion resistance of the Nd-Fe-B magnets. As a result, substantial improvements have been made. Although coating techniques and surface treatments have improved corrosion resistance to a certain degree, the corrosion problems of Nd-Fe-B magnets still remain. This is because the Nd-Fe-B magnet which serves as substrate for coating is prone to react with moisture. The coating or plating may be imperfect and allow the permeation of reacting species such as mois-

---

[1] Manager, Magnetics Section, and research engineer, respectively, Crucible Research Center, Division of Crucible Materials Corp., P.O. Box 88, Pittsburgh, PA 15230.

[2] Manager, Technology, Crucible Magnetics, Division of Crucible Materials Corp., 101 Magnet Drive, Elizabethtown, KY 42701.

ture. Nd-Fe-B magnets are protected from corrosion only when three conditions are satisfied: (1) a dense and protective coating and/or plating has been applied to the surface of the magnet; (2) a protective layer has been formed on the surface or the reactive Nd-rich phases have been otherwise removed from the surface by proper surface treatment; and (3) an improvement has been made to the intrinsic corrosion resistance of the substrate magnet. Consequently, consideration was given to the improvement of the intrinsic corrosion resistance of the uncoated magnets.

Narasimhan et al. [*5*] reported that raising the oxygen content to between 0.6 to 3.5% in Nd-Fe-B magnets significantly improved the corrosion resistance by reducing the disintegration of magnets in hot and humid environments. Kim and Jacobson [*3*] reported that the addition of Al and Dy or dysprosium oxide (Dy_2O_3) in Nd-Fe-B alloys improved the corrosion resistance in humid air. Sagawa et al. [*6*] reported that the addition of Co and Al improved the corrosion resistance of the Nd-Fe-B magnets. Nakamura et al. [*7*] reported that the substitution of Fe with Co and Zr improved the corrosion resistance of the Nd-Fe-B magnet by stabilizing the Nd-rich grain boundary. Sagawa et al. [*8*] and Hirosawa et al. [*9*] reported that the addition of V or Mo improved corrosion resistance by preventing formation of corrosion-prone $NdFe_4B_4$ phase. Although the corrosion resistance is improved by the alloy modifications mentioned above, the corrosion rate is still substantially affected by undefined factors. The factors affecting the corrosion rate and the microstructures of uncoated Nd-Fe-B magnets will be addressed in this study. The factors include the effect of the addition of O, C, and N.

Experimental Procedure

The Nd-Fe-B magnets used in this study were prepared by the conventional powder metallurgical sintering process. The content of oxygen or nitrogen in the alloy was controlled by introducing controlled amounts of air or nitrogen during the jet milling process. The carbon content was controlled by making carbon additions during the melting process. The prepared alloys were hydrided and jet milled to powders with average particle sizes of 1 to 4 μm by Fischer subsieve size (FSSS) measurement. The milled powder was magnetically aligned and isostatically pressed. The compacts were sintered under the vacuum atmosphere at 1030°C for 1 h. The sintered magnets were ground and sliced into cylindrical specimens.

Since previous studies [*4*] showed autoclave testing to be a viable accelerated method for predicting the long-term corrosion resistance of rare earth transition metal magnets in humid room temperature environments, this study used the autoclave test to measure the corrosion rate of the magnets. For comparison, a corrosion test of the magnet in the air at room temperature was also conducted.

The tested magnets were ground about 2 mm deep from the reacted surface and polished with diamond paste. The polished specimens were examined in the scanning electron microscope (SEM) with energy dispersive X-ray spectroscopy (EDX). The phases of the corrosion products were analyzed by X-ray diffractometer.

Results and Discussion

Effect of the O, C, and N Contents on the Corrosion Rate of Nd-Fe-B Magnets in an Autoclave Environment

The Nd-Fe-B magnets with various C, O, and N contents were made and ground into cylindrical specimens. Those specimens were tested in an autoclave at 5 to 10 psig (35 to 69 kPa) of steam pressure at 110 to 115°C for 40 and 96 h. After autoclave testing, the weight loss of the specimen was measured with a balance after brushing off the corrosion products from the specimen. The weight loss per unit area of the specimen was plotted as a function of the content of O, C, and N. Since the weight loss of the magnet was measured per unit area of the specimen during the autoclave test, the weight loss may be used as a measurement of the corrosion rate of the magnet in autoclave environments. The corrosion rate is found to be significantly effected by the C, N, and O contents of the magnet.

As shown in Fig. 1, the weight loss of Fe-33.9Nd-1.15B-0.33O-0.024N magnet after 40-h exposure in an autoclave decreases rapidly as the carbon content increases from 0.06 to 0.09%, and then reaches its lowest value when the carbon content is between 0.09 and 0.11%. Further increases in the carbon content increase the weight loss. The weight loss of the same alloy with increased oxygen (0.5%) and nitrogen (0.05 to 0.09%) contents shows behavior similar to that of the alloy with low oxygen and nitrogen contents. The overall corrosion rate of the alloy, however, is reduced with increased oxygen and nitrogen contents. It is noted that as carbon content increases from 0.06 to 0.1%, the corrosion rate decreases less dramatically for the high O and N containing alloy. However, when the oxygen content is greater than 0.6%, the corrosion rate is much less sensitive to the carbon content in the range of 0.06 to 0.15%. As shown in Fig. 2, the corrosion rate of magnets with oxygen contents greater than 0.6% decreases rapidly as carbon content increases up to about 0.05% and then reaches the minimum at about 0.06 to 0.14% of carbon. If the oxygen content is about 0.7% and the carbon content exceeds 0.15%, the corrosion rate starts to increase. If the oxygen content is greater than 0.8%, then the minimum corrosion rate is maintained until the carbon content reaches about 0.2%. Therefore, when the oxygen content is greater than 0.6%, the proper range of carbon for the minimum corrosion rate is between 0.06 and 0.14%.

Since the corrosion rate reaches its lowest value when the carbon content is about 0.1%, an alloy, Fe-33.5Nd-1.1B-0.1C, was made and the corrosion rate measured as a function of O and N contents. Figures 3 and 4 show the weight loss of a Nd-Fe-B magnet after exposure in an autoclave at 5 to 10 psig (35 to 69 kPa) (110 to 115°C) for 96 h, as a function of oxygen content. As shown in Fig. 3, the corrosion rate of a Fe-33.5Nd-1.1B-0.1C-(0.05 to 0.15)N magnet decreases rapidly as the oxygen content increases from 0.2 to about 0.6% and then reaches the minimum when the oxygen content is between 0.6 and 1.0%. The minimum corrosion rate produced a weight loss of less than 1 mg/cm^2 and corrosion products that are hardly observable on the surface of the magnet.

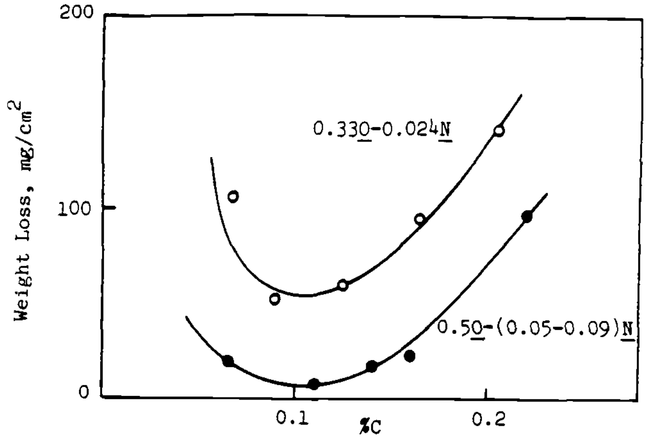

FIG. 1—*Weight loss of Fe-33.9Nd-1l.15B magnets after exposure in autoclave at 5 to 10 psig (35 to 69 kPa) for 40 h as a function of C, O, and N contents.*

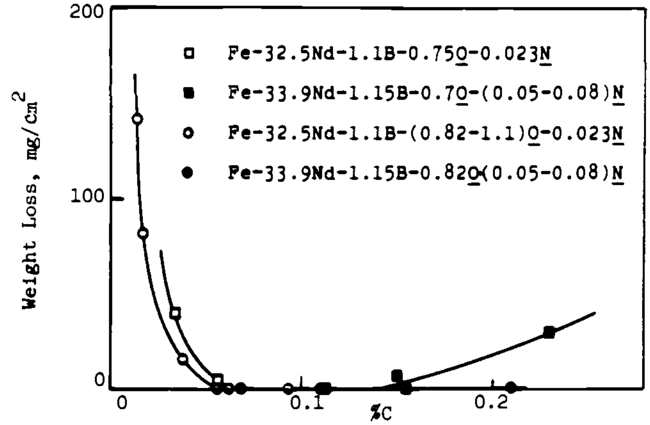

FIG. 2—*Weight loss of Nd-Fe-B magnets after exposure in autoclave at 5 to 10 psig (35 to 69 kPa) for 96 h as a function of C content.*

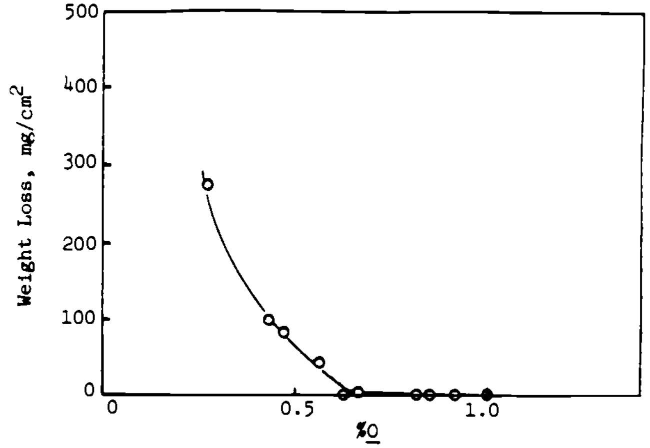

FIG. 3—*Weight loss of Fe-33.5Nd-1.1B-0.1C-(0.05 to 0.15) N magnets after exposure in autoclave at 5 to 10 psig (35 to 69 kPa) for 96 h as a function of O content.*

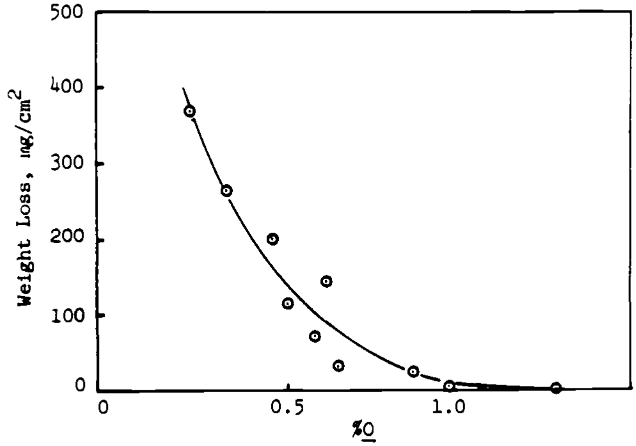

FIG. 4—*Weight loss of Fe-33.5Nd-1.1B-0.1C-0.02N magnets after exposure in autoclave at 5 to 10 psig (35 to 69 kPa) for 96 h as a function of O content.*

The oxygen content for the minimum corrosion rate varies depending upon the N content, although the corrosion rate decreases rapidly as the oxygen content increases up to about 0.6%. As shown in Fig. 4, the corrosion rate of the low N Fe-33.5Nd-1.1B-0.1C-0.02N magnets also decreases rapidly with increasing oxygen content from 0.2 to 0.6%, but does not reach the minimum when oxygen content is between 0.6 and 1.0%. Instead, it reaches the minimum at 1.2% oxygen content. From these results, it is noted that the corrosion rate decreases as nitrogen content increases from 0.02 to 0.05 to 0.15% at the given oxygen and carbon (0.1%) contents. This indicates that a certain range of nitrogen is beneficial in improving the corrosion resistance and shifts oxygen contents to a lower range for the minimum corrosion rate.

When the carbon content is relatively low ($\leq$0.06%), the effect of nitrogen content on the corrosion rate is adverse. As shown in Fig. 5, the corrosion rate of low carbon alloys increases slowly up to 0.1% N and then increases rapidly with a further increase in N content. Therefore, a nitrogen content exceeding 0.1% is detrimental to the corrosion resistance of low carbon Nd-Fe-B alloys, although somewhat higher nitrogen contents (0.05 to 0.15%) are beneficial to the corrosion resistance for high carbon Nd-Fe-B alloys. The proper nitrogen content for the minimum corrosion rate, therefore, ranges from 0.05 to 0.10% depending on the C and O contents.

These results indicate that the corrosion rate reaches a minimum when the nitrogen content is within the range of 0.05 to 0.10%, the carbon content is between 0.06 and 0.14%, and the oxygen content is between 0.6 and 1.2%.

Microstructural Study

The Nd-Fe-B magnets tested in autoclave were selected as shown in Tables 1 and 2. These were ground about 2 mm deep from the reacted surface and polished with diamond paste. The polished specimens were examined in the SEM with EDX.

Figure 6 shows the backscattered images of SEM micrographs of Specimens A (0.014%C-0.865%O) and B (0.055%C-0.815%O) at X1000 magnification. As shown in this figure, both Magnets A and B exhibit Nd-rich phases as mainly flat white phases with some raised white phases. EDX analyses on both flat and raised white phases of both Specimens A and B exhibit very high O and high Nd peaks. The raised white phases exhibit higher O and lower Nd peaks

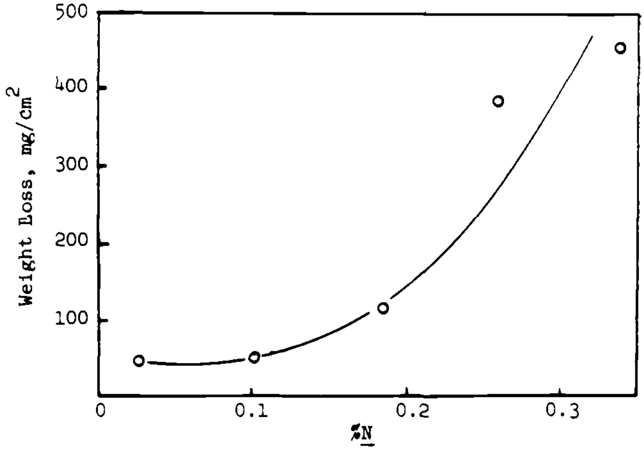

FIG. 5—*Weight loss of Fe-34.2Nd-1.13B-0.55O-0.06C magnets after 40 h exposure in autoclave at 5 to 10 psig (35 to 69 kPa) as a function of N content.*

TABLE 1—*Chemical compositions of the alloys examined in this study.*

Alloy No.	Chemical Composition (wt.%)					
	Fe	Nd	B	O	N	C
A	Bal	32.5	1.1	0.865	0.021	0.014
B	Bal	32.5	1.1	0.815	0.024	0.055
C	Bal	33.5	1.1	0.245	0.015	0.10
D	Bal	33.5	1.1	0.920	0.014	0.10
E	Bal	33.5	1.1	0.820	0.110	0.10

NOTE: Bal = balance.

than the flat white phases. This indicates that both white phases are Nd-rich phases containing oxygen or Nd-oxides [presumably, the flat white phases are NdO_x and the raised white phases are neodymium oxide (Nd_2O_3)]. From this result, it is noted that the α-Nd becomes Nd-oxide or a Nd-rich phase containing oxygen when the oxygen content is increased in a Nd-Fe-B magnet. The SEM micrographs show that both magnets exhibit similar microstructures, although the low carbon alloy (A) exhibited flat white phase both at triple junctions and at the grain boundaries, while the higher carbon alloy (B) exhibited the flat oxide mainly at the triple junctions. The agglomeration of flat white phase at the triple junctions may lead to thinning of the Nd-rich phase in the grain boundary. It is therefore believed that the increase in carbon content in a Nd-Fe-B magnet may cause the Nd-rich phase to agglomerate in the triple junctions and/or to stabilize the grain boundary Nd-rich phase against moisture attack. The distribution of the carbon in the magnet could not be determined due to equipment analytical limitations.

After microstructural examination, both Specimens A and B were removed from the SEM and exposed in the air at room temperature for 100 days. These specimens were again examined in the SEM.

Figure 7 shows the backscattered image of Specimens A and B after 100 days exposure in the air at room temperature. Magnet A exhibits a greatly increased number of raised corrosion products on the surface, while Magnet B exhibits few new raised corrosion products. It is rather similar to the microstructure of the freshly polished magnet (B) shown in Fig. 6. X-ray diffraction analyses of the corrosion products exhibit mainly $Nd(OH)_3$ phase and $Nd_2Fe_{14}B$ phase peaks. It is therefore assumed that the Nd-rich phases in the grain boundary and at the triple junctions react with moisture to form the neodymium hydroxide [$Nd(OH)_3$] phase, which may be accompanied by a volume expansion of the Nd-rich phase at the triple junctions and grain boundaries and with grain boundary weakening. The simultaneous reaction of the grain

TABLE 2—*Weight loss of various Nd-Fe-B magnets after exposure in autoclave at 5 to 10 psig (35 to 69 kPa) (110 to 115°C) for 40 and 96 h, respectively.*

Alloy No.	Weight loss, mg/cm²	
	40 h	96 h
A	31.8	142.0
B	1.0	0.5
C	93.0	368.0
D	0.4	6.9
E	0.3	0.4

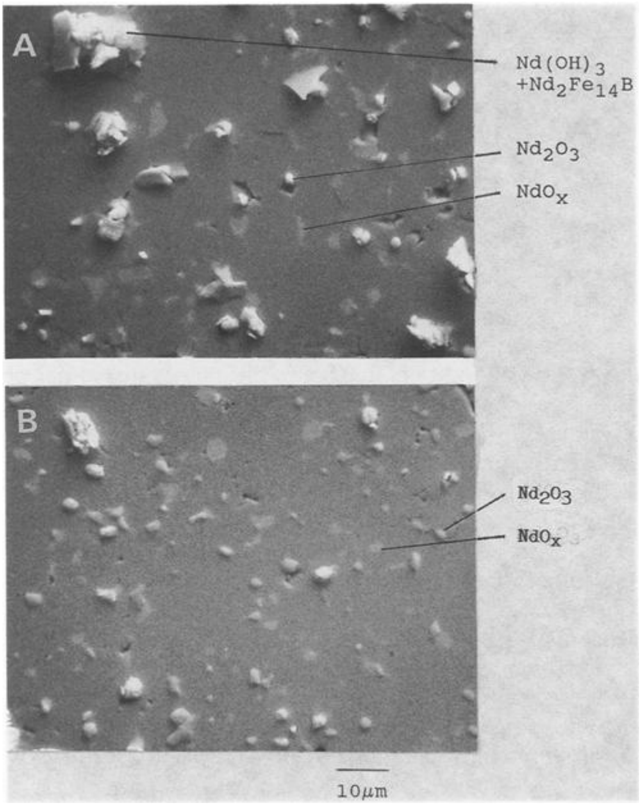

FIG. 6—*SEM micrographs of Specimens A and B after polishing, back-scattered image (BSI), X1000.*

boundary weakening and volume expansion of Nd-rich phase may separate a $Nd_2Fe_{14}B$ grain from the other grains and push it to the surface of the magnet.

These results indicate that carbon plays a very important role in improving the corrosion resistance of the Nd-Fe-B magnet in the ambient environment as well as in the accelerated corrosion environment of the autoclave.

Figure 8 shows the backscattered images of SEM micrographs of Specimens C (0.1%C-0.24%O-0.015%N), D (0.1%C-0.92%O-0.014%N), and E (0.1%C-0.82%O-0.11%N). Magnet C (low oxygen and low nitrogen) exhibits mainly flat white phases at the grain boundary and triple junctions and a few raised white phases near the triple junctions. The EDX analysis shows that this flat white phase exhibits only Nd peaks without oxygen peaks and that the raised white phase exhibits high O and Nd peaks. This indicates that the flat white phase of this magnet is the α-Nd phase and the raised phase is Nd-oxide (presumably Nd_2O_3). These results indicate that the magnet with low O, low N, and high C contents formed mainly α-Nd on the grain boundaries and triple junctions and some Nd-oxide near the triple junctions.

Magnet D (high oxygen and low nitrogen) exhibits mainly flat white phases at the triple junctions and some raised white phases near the triple junctions. The EDX analysis on both flat and raised white phases exhibit high O and Nd peaks. The raised phase exhibits an oxygen peak higher and a Nd peak lower than those of the flat white phase. This indicates that both

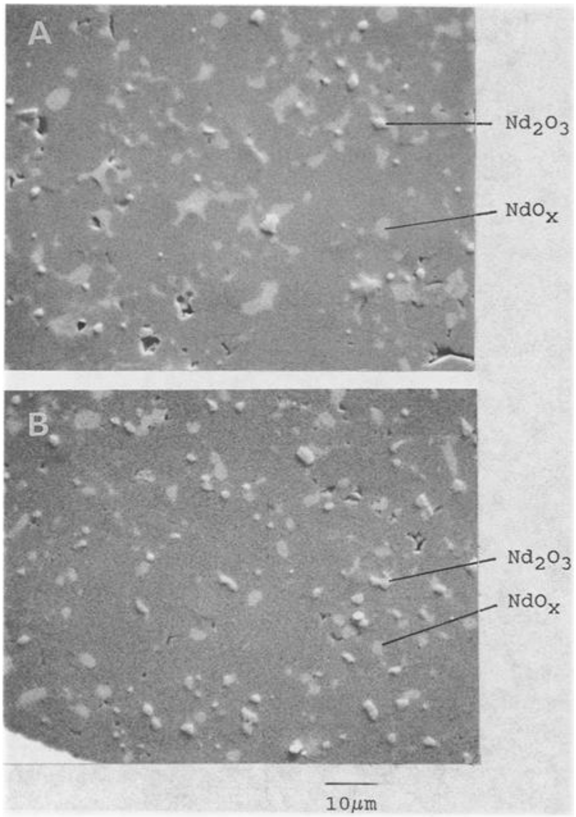

FIG. 7—*SEM micrographs of Specimens A and B after 100-h exposure in air at room temperature, BSI, X1000.*

flat and raised white phases of this magnet are Nd-oxides (presumably the flat phase is NdO_x and the raised phase is Nd_2O_3). These results indicate that the magnet with high O, low N, and high C formed Nd-rich phase as NdO_x mainly at the triple junctions and raised oxides (presumably Nd_2O_3) near the triple junctions.

Magnet E (high O, high N, and high C) exhibits mainly raised white phases and a few flat white phases near the triple junctions. The EDX analyses show that both raised and flat white phases exhibit high O and Nd peaks. The raised white phase exhibit an oxygen peak higher and an Nd peak lower than those of the flat white phase. This indicates that the magnet with high O, high N, and high C formed mainly raised oxides (presumably Nd_2O_3) near the triple junctions and a few flat oxides (presumably NdO_x) at the triple junctions.

From these results, it is found that the magnet with low O and low N contents forms mainly α-Nd as a Nd-rich phase both at grain boundaries and triple junctions. If only the oxygen content is increased in that alloy, the α-Nd is converted to an Nd-rich phase containing oxygen (presumably NdO_x) and the Nd-rich phase moves from the grain boundaries to the triple junctions. When both oxygen and nitrogen contents are high in the magnet, most of the flat Nd-oxide (presumably NdO_x) converts to the raised Nd-oxide (presumably Nd_2O_3). This indicates that small amounts of nitrogen addition helps to convert unstable Nd-oxide (presumably

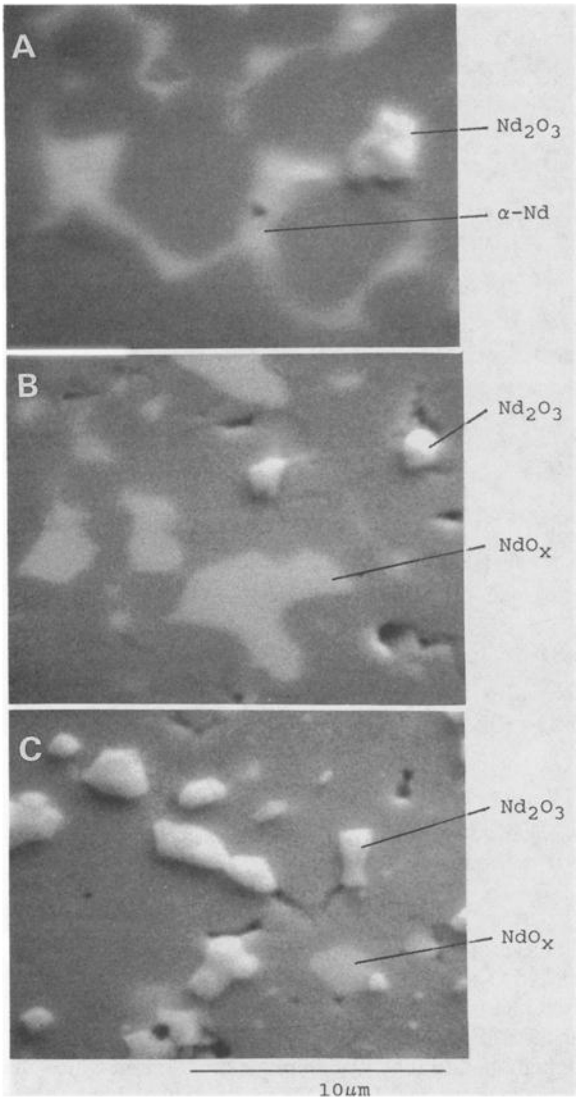

FIG. 8—*SEM micrographs of Specimens C, D, and E, BSI, X5000.*

NdO_x) to stable Nd-oxide (presumably Nd_2O_3). It is believed, therefore, that the change in microstructure is responsible for improving the corrosion resistance of the Nd-Fe-B magnets.

Based on the present study, the model for corrosion mechanism of Nd-Fe-B magnets can be suggested as follows: Since the Nd-rich phase (α-Nd or NdO_x) is much more reactive than the matrix $Nd_2Fe_{14}B$ phase, there will be a preferential corrosion reaction of the Nd-rich phase when there is enough moisture in the air. The reaction may initiate from the Nd-rich phase as follows:

$$Nd + 3/2\ H_2O + 3/4\ O_2 \rightarrow Nd(OH)_3$$

or

$$NdO_x + 3/2\ H_2O + y\ O_2 \rightarrow Nd(OH)_3$$

where $y = 3/4 - X/2$.

When the grain boundary is coated with an Nd-rich phase of sufficient thickness and is exposed to moist air (Fig. 9A), then the corrosion reaction of the Nd-rich phase may proceed continuously along the grain boundary with an accompanying volume expansion of corrosion products as shown in Fig. 9C. The volume expansion of the corrosion products may lead to intergranular fracture or displacement of the grain, thus providing a path of moisturized air to the next Nd-rich boundary phase; thus the corrosion reaction may proceed continuously. The simultaneous corrosion reaction of the Nd-rich phase and volume expansion of corrosion products may lead to continuous corrosion. On the other hand, if the Nd-rich phase at the grain boundary is very thin or located only at the triple junctions (Fig. 9B), the continuous corrosion reaction may be confined to the triple junctions at the surface and, therefore, may not be self-propagating as shown in Fig. 9D. When the Nd-rich phase is stabilized against moisture by reducing its reactivity by the addition of effective elements such as O, C, and N, the corrosion reaction will be further restricted. The corrosion rate of the magnet is a function of the microstructure of the magnet, the reactivity of the Nd-rich phase (alloying composition), the humidity level at the interface between metal and environment, and temperature.

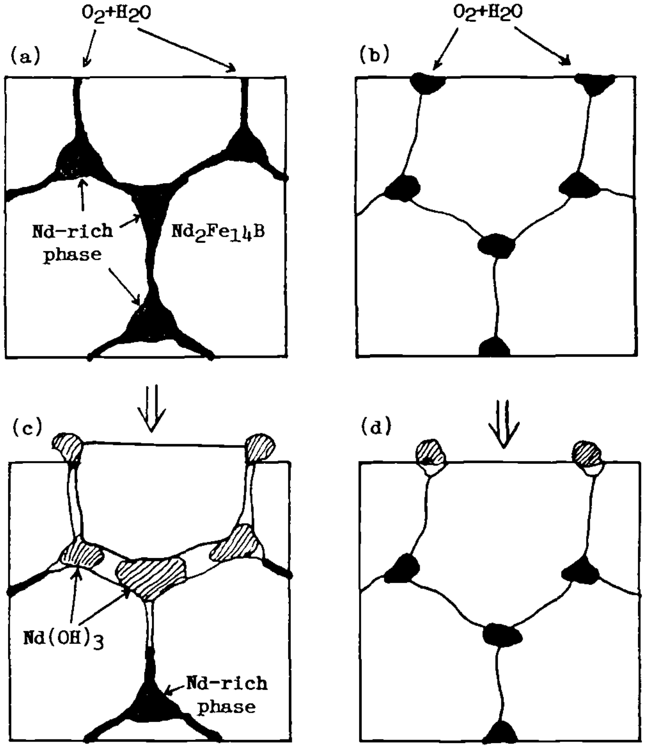

FIG. 9—*Model for corrosion mechanism of Nd-Fe-B magnets in humid air:* (a) *Nd-Fe-B magnet with thick grain boundaries;* (b) *magnet with thin grain boundaries;* (c) *magnet* (a) *after exposure in humid air, and* (d) *magnet* (b) *after exposure in humid air.*

Therefore, the corrosion resistance of the Nd-Fe-B magnet can be improved by modifying the microstructure, stabilizing the Nd-rich phase against humid air, and by reducing the moisture level at the metal-gas interface by forming a protective layer on the surface or by applying a dense and protective coating/plating layer on the surface of the magnet.

Summary

The corrosion resistance of the Nd-Fe-B magnets can be improved when three conditions are satisfied: (1) a protective coating has been applied to the surface of the magnet; (2) a protective layer has been formed on the surface and/or the reactive Nd-rich phases have been otherwise removed from the surface; and (3) an improvement has been made to the intrinsic corrosion resistance of the substrate magnet. The intrinsic corrosion resistance of the uncoated magnet is significantly affected by the O, C, and N contents of the alloy.

The corrosion rate rapidly decreases with increasing oxygen content and reaches the minimum when the oxygen content is between 0.6 and 1.2%. The corrosion rate rapidly decreases as the carbon content increases up to about 0.06% and then gradually decreases as the carbon content increases up to about 0.1%. A further increase in the carbon content up to about 0.15% slowly increases the corrosion rate and then increases the rate substantially with further carbon increase (>0.15%). Therefore, the proper carbon content for the low corrosion rate is 0.10 ± 0.04%. The effect of carbon content on the corrosion rate becomes smaller at higher oxygen contents in the alloy. The effect of nitrogen content on the corrosion rate is less dramatic when it is less than 0.1%, i.e., the corrosion rate decreases with increasing nitrogen content up to 0.10% when oxygen and carbon contents are properly high. The corrosion rate increases slowly with a nitrogen content increase when the carbon and oxygen contents are low. If the nitrogen content exceeds 0.1% in a low C and O alloy, the corrosion rate increases dramatically. The results of this investigation indicate that the corrosion rate reaches the minimum when: O = 0.6 to 1.2%; C = 0.06 to 0.14%; and N = 0.05 to 0.10%.

The corrosion resistance of the Nd-Fe-B magnet is closely related to the microstructure, which is determined by controlling the minor elements such as O, C, and N. When the oxygen or carbon content is low, the alloy forms a thick Nd-rich phase (α-Nd and/or Nd-oxide) on both grain boundaries and triple junctions of the grain boundary. As the oxygen and carbon contents increase, the Nd-rich coating on the boundaries becomes thinner and agglomerates into the triple junctions. As oxygen content increases, the α-Nd changes to the Nd-oxide. This microstructural change may be responsible for improving the corrosion resistance. A small increase in N further improves the corrosion resistance.

Acknowledgment

The authors wish to thank E. J. Dulis and J. J. DuPlessis for their interest in this work and F. S. Snyder, S. M. Rendziniak, and T. L. Tressler for specimen preparation and SEM work.

References

[*1*] Sagawa, M., Fujimura, S., Togawa, N., Yamamoto, H., and Matsuura, Y., "New Material for Permanent Magnets on a Basis of Nd and Fe," *Journal of Applied Physics,* Vol. 55, 1984, p. 2083.

[*2*] Croat, J., Herbst, J., Lee, T., and Pinkerton, F., "Pr-Fe and Nd-Fe-Based Materials: A New Class of High-Performance Permanent Magnets," *Journal of Applied Physics,* Vol. 55, 1984, p. 2078.

[*3*] Kim, A. and Jacobson, J., "Oxidation and Oxidation Protection of Nd-Fe-B Magnets," *IEEE Transactions on Magnetics,* Vol. 23, No. 5, 1987, p. 2509.

[4] Kim, A., "Corrosion and Corrosion Protection of RE-Fe-B Magnets," *Journal of Materials Engineering,* Vol. 11, No. 1, 1989, p. 95.

[5] Narasimhan, K., Willman, C., and Dulis, E., Oxygen Containing Permanent Magnet Alloy, U.S. Patent No. 4588439, 1986.

[6] Sagawa, M., Fujimura, S., Yamamoto, H., and Hirosawa, S., Corrosion Resistant Rare Earth Magnet Material, Japanese Patent No. 63–38555, 1988.

[7] Nakamura, H., Fukuro, A., and Yoneyama, T., "Corrosion Resistance of Nd-Fe-B Base Magnet Alloys," Proceedings of the Tenth International Workshop on Rare Earth Magnets and Their Applications, Kyoto, Japan, 1989, p. 315.

[8] Tenaud, P., Vial, E., and Sagawa, M., "Improved Corrosion and Temperature Behavior of Modified Nd-Fe-B Magnets," *IEEE Transactions on Magnetics,* Vol. 36, No. 5, 1990, p. 1730.

[9] Hirosawa, S., Tomizawa, H., Mino, S., and Hamamura, A., "High-Coercivity Nd-Fe-B Type Permanent Magnets with Less Dysprosium," *IEEE Transactions on Magnetics,* Vol. 26, No. 5, 1990, p. 1960.

Terry A. DeBold,[1] *Millard S. Masteller,*[1] *and Thomas N. Werley*[1]

Corrosion of Soft Magnetic, Controlled Expansion, and Glass Sealing Alloys

---

REFERENCE: DeBold, T. A., Masteller, M. S., and Werley, T. N., "**Corrosion of Soft Magnetic, Controlled Expansion, and Glass Sealing Alloys,**" *Corrosion of Electronic and Magnetic Materials, ASTM STP 1148,* P. J. Peterson, Ed., American Society for Testing and Materials, Philadelphia, 1992, pp. 80–89.

ABSTRACT: There is relatively little data available on the corrosion resistance of soft magnetic, controlled expansion, and glass sealing alloys. This has been due in part to the relatively innocuous traditional service environments. The primary purpose of this paper is to provide corrosion data on a wide variety of iron-base, nickel-base, and cobalt-base alloys typically used for magnetic, controlled expansion, and glass sealing applications. The data presented systematically characterize the corrosion resistance of these alloys using humidity and salt spray testing and provide a database for the selection of materials as well as the development of new test procedures.

KEY WORDS: rusting, stress corrosion, corrosion tests, humidity, ferritic stainless steels, magnetic materials, invar

There is relatively little data available on the corrosion resistance of soft magnetic, controlled expansion, and glass sealing alloys. This has been due in part to the relatively innocuous traditional service environments. Typically, if corrosion resistance is of concern, protective coatings such as nickel plating are used. However, new opportunities for these alloys, especially in the automotive industry as well as the general industry trend towards higher reliability and reduced manufacturing cost, have prompted increasing interest in the corrosion resistance of these alloys. Carpenter Technology Corp. is one of the world's principal producers of such alloys.[2] Although some corrosion testing of these alloys has been performed over the years in response to a particular production or customer problem, a synoptic view has been lacking. In response to the increasing number of inquiries, a general survey of the corrosion resistance of these alloys was undertaken. Clearly, it is impossible to anticipate all possible service environments to which these alloys might be subjected. However, it is improbable that they would be subjected to severe environments such as boiling concentrated acids, etc., as has been the focus of some studies [*1,2*]. Therefore, we have concentrated on two basic, well-recognized types of corrosion tests: (1) humidity testing due to the omnipresent nature of humidity; and (2) neutral salt spray testing, which is of particular interest to the automotive industry.

The purpose of this paper is to summarize available data on the corrosion resistance of commercially available soft magnetic, glass sealing, and controlled expansion alloys, hereafter referred to as special alloys. The principal alloys in each of these product groups have been examined with the intent to provide a baseline comparison. In addition, a more detailed exam-

[1] Carpenter Technology Corp., Reading, PA 19612.

[2] Carpenter Temperature Compensator "30", Carpenter Invar "36", Carpenter Low Expansion "42", Carpenter High Permeability "49", Carpenter HyMu "80", Hiperco, and Kovar are registered trademarks of Carpenter Technology Corp., Reading, PA.

ination of the corrosion of nickel-iron alloys, which are the basis for many of these special alloys, is included. The design of soft magnetic alloys with improved corrosion resistance will be discussed. The paper concludes with a brief summary of results on stress corrosion cracking of controlled expansion alloys used in thermostat metals. It is hoped that the data presented here will aid in design choices and suggest areas for further study.

Experimental Procedure

The primary study to be reported in this paper is a study of the corrosion resistance of special alloys using both humidity and neutral salt spray testing. The alloys examined are listed in Table 1, along with the ASTM specifications and UNS designations (where such exist), nominal composition, and test specimen condition. The characteristics of these alloys are as follows:

1. *Electrical Iron*—high-purity iron which has been used primarily in the production of solenoid cores and relay components.
2. *Super Invar 32-5*—nickel-iron controlled expansion alloy with the lowest thermal expansivity of any metallic alloy.
3. *Invar "36"*—nickel-iron alloy which is the most commonly used low expansion alloy. The largest use has been as the low expansion side of thermostat metal.
4. *High Permeability "49"*—high-permeability nickel-iron magnetic alloy which has been used primarily in high-quality, low-noise signal and control transformers. It has also been used for magnetic shielding and sensitive relays and solenoids.
5. *High Permeability 49-FM*—free machining version of high-permeability "49" alloy which has been used primarily in solenoids and relay components.
6. *HyMu "80"*—very high magnetic permeability nickel-iron alloy which has been used in transformers, magnetic shields, and magnetic flux detection devices.
7. *Nickel Alloy 201*—essentially pure nickel which has been used in the production of thermostat metal. It is the most common form of pure nickel.
8. *Stainless 430 FR Solenoid Quality*—free machining, controlled chemistry ferritic stainless steel which has been used in the production of corrosion-resistant solenoid cores and relay components.
9. *Hiperco 50A*—iron-cobalt alloy which has the highest saturation flux density of any material. Hiperco 50A has been primarily used in the production of aircraft motor and generator laminations where weight is the primary concern.
10. *Hiperco 27*—iron-cobalt alloy with similar applications as Hiperco 50A. It is more malleable but has higher core losses than Hiperco 50A.
11. *Vicalloy 1*—iron-cobalt-vanadium semihard or hard magnetic alloy depending on heat treatment. It has been used primarily in signaling devices and sensors.
12. *High Expansion 22-3 alloy*—nickel-chromium-iron alloy which has high thermal expansion and which has been used for the high expansion side of thermostat metals.
13. *Kovar Alloy*—nickel-iron-cobalt controlled expansion alloy whose thermal expansivity closely matches silica glass and certain ceramics and which has been used for sealing electronic devices.
14. *Silicon Core Iron B*—general purpose 2.5% silicon iron alloy which has been used in the production of relays and solenoids.
15. *Silicon Core Iron B-FM*—free machining version of Silicon Core Iron B with similar uses.
16. *High Expansion 72*—manganese base alloy which has highest thermal expansivity of any metallic alloy and has been used as the high expansion side of thermostat metals.

TABLE 1—*Alloys studied in the humidity and salt spray test program.*

Name	ASTM Designation	UNS Designation	Nominal Composition	Anneal
Electrical iron	A848-T1	None	>98.5% Fe	843°C (1550°F)-1h-wet H_2
Super Invar 32-5	None	None	32% Ni-5% Co-Fe	871°C (1600°F)-1h-dry H_2
Invar "36"	B753-T36	K93600	36% Ni-Fe	871°C (1600°F)-1h-dry H_2
High Permeability "49"	A753-T2	None	48% Ni-Fe	1177°C (2150°F)-4h-dry H_2
High Permeability 49-FM	None	None	48% Ni-0.1% Se-Fe	1177°C (2150°F)-4h-dry H_2
HYMU "80"	A753-T4	None	80% Ni-4.3% Mo-Fe	1177°C (2150°F)-4h-dry H_2
Nickel Alloy 201	B753-T99	N02201	>99.5% Ni	704°C (1300°F)-1h-dry H_2
Stainless 430 FR, Solenoid Quality	A838-T2	None	18% Cr-1% Si-0.3% S-Fe	843°C (1550°F)-2h-dry H_2
Hiperco 50A	A801-T1	R30005	49% Co-2% V-Fe	865°C (1590°F)-4h-dry H_2
Hiperco 27	A801-T2	None	27% Co-Fe	865°C (1590°F)-4h-dry H_2
Vicalloy 1	None	None	52% Co-10% V-Fe	600°C (1112°F)-2h-argon
High Expansion Alloy 22-3	B753-T22	K92510	22% Ni-3% Cr-Fe	871°C (1600°F)-1h-dry H_2
Kovar Alloy	F15	K94610	29% Ni-17% Co-Fe	1099°C (2010°F)-1h-dry H_2
Silicon Core Iron B-FM	A867-T2F	None	2.5% Si-0.2% P-Fe	843°C (1550°F)-2h-wet H_2
Silicon Core Iron B	A867-T2	None	2.5% Si-Fe	843°C (1550°F)-2h-wet H_2
High Expansion 72	B753-T10	M27200	72% Mn-18% Cu-Ni	788°C (1450°F)-1h-dry H_2

All specimens were in the form of nominal 50-mm (2-in.)-long by 25-mm (1-in.)-wide by 1.5-mm (0.060-in.)-thick cold rolled strip heat treated as indicated in the table. The faces of the test coupons were not mechanically finished prior to testing, nor were the specimens passivated. Minor longitudinally oriented lines (apparently not significant to corrosion resistance) were present on the as-received surface of the HyMu 80 alloy and the Type 430 FR Solenoid Quality strip. All specimens were ultrasonically cleaned with alkaline detergent, rinsed with alcohol, and immediately dried.

The heat treatments used were chosen to represent the normal practices used with the particular alloy and correspond to ASTM specification requirements or recommendations wherever possible. After heat treating, most specimens exhibited a dull metallic gray finish. The exceptions were the High Expansion 72 (green finish) and Vicalloy 1 (dark gray finish) specimens. Humidity testing was conducted at 35°C (95°F) and 95% relative humidity for a duration of 200 h. Neutral salt spray testing was conducted per ASTM Method of Salt Spray (Fog) Testing (B 117) using a 5% NaCl spray at 35°C (95°F) and a duration of 24 h. Duplicate specimens were tested in each case.

Results and Discussion

The results of the humidity test are shown in Fig. 1, which represents the worst of the duplicate test coupons, although the duplicates were generally similar. As might be expected, alloys with high iron content tended to be more susceptible to rusting with two exceptions. The specimens of electrical iron, a very high-purity form of iron, show significantly less rusting than the silicon core irons. This may be due to the formation of a more adherent or more corrosion-resistant film on the electrical iron. The second exception is the 430 FR Solenoid Quality stainless alloy which, on account of its high chromium content (18% Cr), is not expected to be susceptible to rusting. The staining that did occur may be due to free iron contamination, i.e., microscopic particles of iron often found on the surface of stainless steel which has not been passivated. The nickel-iron and cobalt-iron alloys are expected to show increased amounts of rusting as the iron content increases. Thus alloys such as Invar 36 and Super Invar 32-5 are more likely to rust than higher nickel content alloys such as HyMu 80. Similarly, it would be expected that Hiperco 27 (27% cobalt-iron) is more likely to rust than Hiperco 50A (50% cobalt-iron). On a practical level, however, nearly all of the alloys studied will exhibit rusting given sufficient time. This can be a problem when semifinished material is stored in a general warehouse environment awaiting use. It is common practice to use desiccated containers or oil coatings during the production and storage of these alloys for more critical applications.

The results of the salt spray testing are shown in Fig. 2, which, again, shows the worst of the duplicate test coupons. Good reproducibility was obtained for duplicate specimens. Clearly, with the exception of Nickel 201 and High Expansion 72 alloy, all of the remaining alloys exhibit varying degrees of rusting. Even the ferritic stainless steel exhibits some rusting. This is in general agreement with experience and may be related to free iron remaining on the unpassivated surface.

Longitudinal streaks of rust occurred on several specimens (e.g., High Permeability 49) due to corrosion products running down the specimen from the attack side. Such areas of active corrosion are often separated by cathodic areas where attack is less likely.

The Vicalloy 1 alloy is significantly attacked, although this is not readily seen in the figure. It is interesting to note that the High Expansion 72 alloy did not exhibit significant attack. This can be explained by the fact that heat treatment of the alloy, even in dry hydrogen, results in an oxide film that confers some corrosion resistance. If the surfaces are abraded and tested, severe attack results. Such oxide films are often not useful as a corrosion prevention mecha-

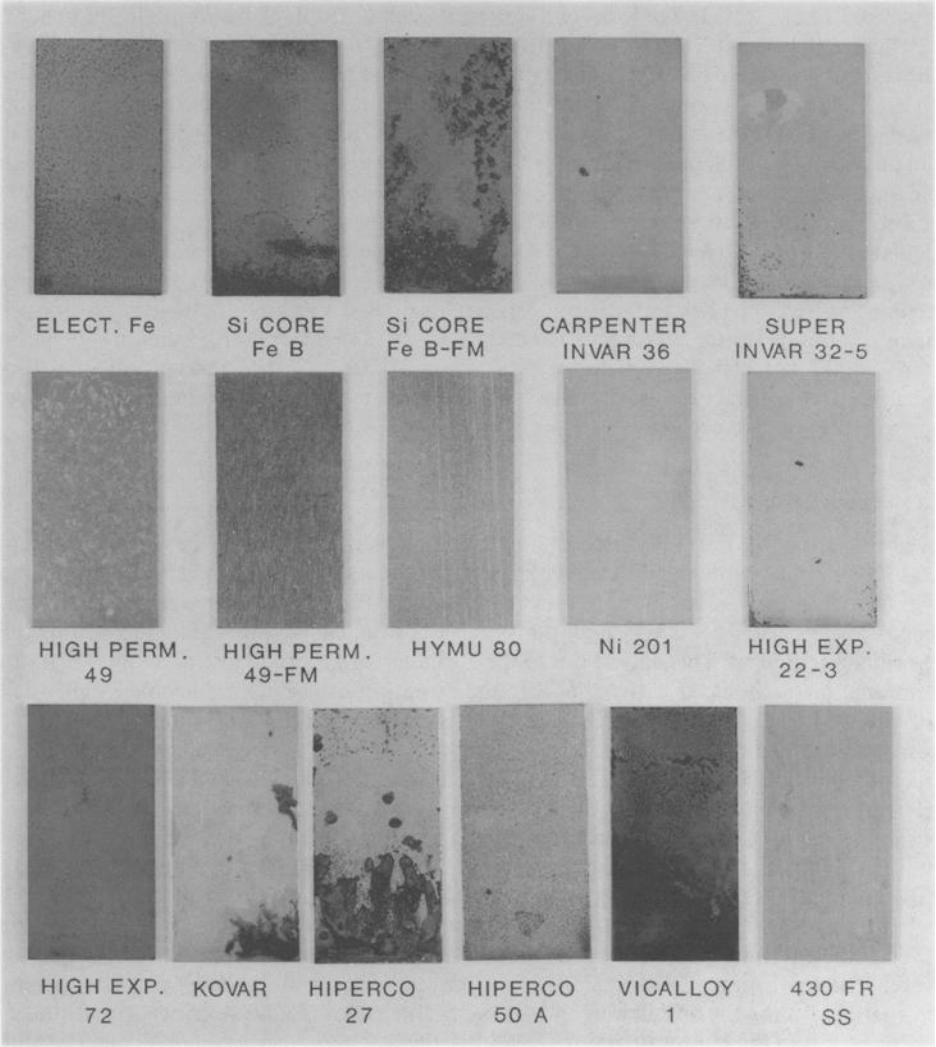

FIG. 1—*Humidity test results on various special alloys: 95% relative humidity at 35°C (200-h duration). Worst of duplicate specimens.*

nism in the presence of halides since penetration of the film can result in a loss of protection as can be clearly seen in the salt spray results for the Vicalloy alloy.

Several of the alloys studied are free machining alloys. This involves use of free machining additives such as phosphorus, sulfur, and selenium to the alloy. In the case of sulfur and selenium additions, which are used in the production of free machining nickel-iron and ferritic stainless steels, sulfide and selenide inclusions are formed which may act as sites for pitting corrosion. It can be observed from Figs. 1 and 2 that there is little difference in corrosion behavior between Silicon Core Iron B and its free machining variant Silicon Core Iron B-FM. Both are attacked in both test environments. Similarly, there is little difference evident

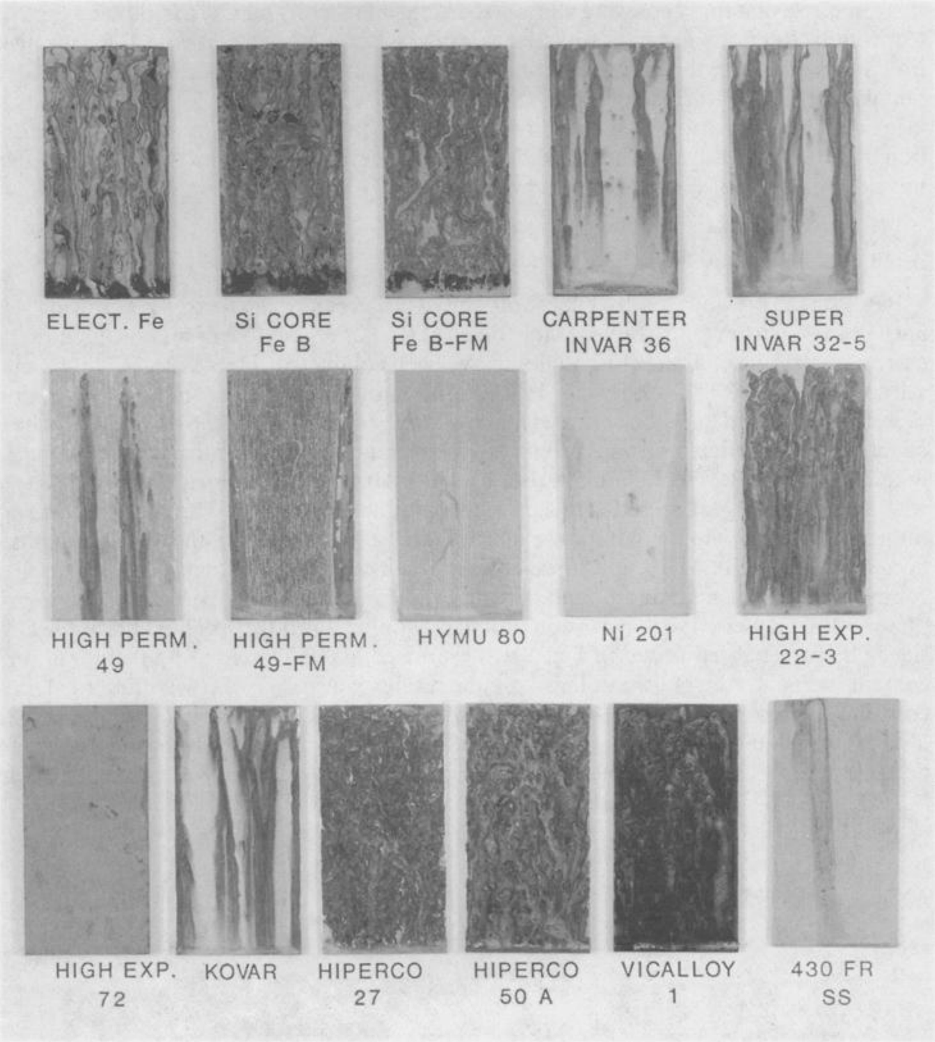

FIG. 2—*Salt spray (fog) test results on various special alloys: 5% neutral salt spray at 35°C according to ASTM B 117, 24-h duration. Worst of duplicate specimens.*

between High Permeability "49" and its free machining variant, High Permeability 49-FM alloy. It can be stated that given the generally poor corrosion resistance of this group of alloys, that free machining additives are not particularly detrimental to the corrosion resistance in most environments. For the more corrosion-resistant stainless steels, it has been observed that free machining grades are more prone to attack than their nonfree machining counterparts. Thus the slight attack noted for the 430FR Solenoid Quality alloy in the salt spray test is expected, especially given the unpassivated condition.

The salt spray environment is a very severe test environment for this group of alloys and is thus not a particularly discriminating form of corrosion testing for these materials. However, this test is relevant for very severe service environments such as marine atmosphere exposure. Conversely, humidity testing is a relatively benign form of testing, particularly for the nickel-iron alloys that form the basis for most of the special alloys produced. Both test methods are popular methods of corrosion testing and together provide end points for a wide range of service exposures. Increasing the duration of exposure in humidity testing or decreasing the duration of the salt spray test can help to differentiate the corrosion behavior of the various alloys, but clearly a more discriminating test method would be desirable.

Additional Results for Nickel-Iron Alloy

Based on the previous results it does appear that nickel can confer increased corrosion resistance in the environments studied. More detailed studies on the role of nickel content on the corrosion resistance of nickel-iron alloys have been conducted. The results of 200-h neutral salt spray [ASTM B 117—5% NaCl, 35°C (95°F)] testing of a series of commercially produced nickel-iron alloys in both the annealed and cold-rolled condition are shown in Fig. 3. The test coupons used are circular disks, 32 mm (1.3 in.) in diameter, punched from thin strip, ranging in thickness from 0.24 to 1.0 mm (0.01 to 0.04 in.). All specimens were ultrasonically cleaned with alkaline detergent, rinsed with alcohol, and immediately dried. The coupons were positioned at a 45° angle in the salt spray cabinet. Starting with pure iron, the nickel contents are nominally 30, 36, 40, 47, 50, and 80 wt% nickel. It can be clearly seen that increasing the nickel content results in decreasing amounts of rust. As in Fig. 2, longitudinal streaks of rust occurred on several specimens due to corrosion products running down the specimen from the attack side. The percent area rusted in Fig. 3 was estimated and is plotted as a function of nickel content in Fig. 4. Also shown in Fig. 4 are the results of a study by Schwerdtfeger [3] on the corrosion rates of binary nickel-iron alloys immersed for 210 days in room temperature (3% NaCl). Overall, the data show a sharp decrease in corrosion resistance as the nickel content is decreased below about 50%. There is some evidence that the cold-worked material exhibits a

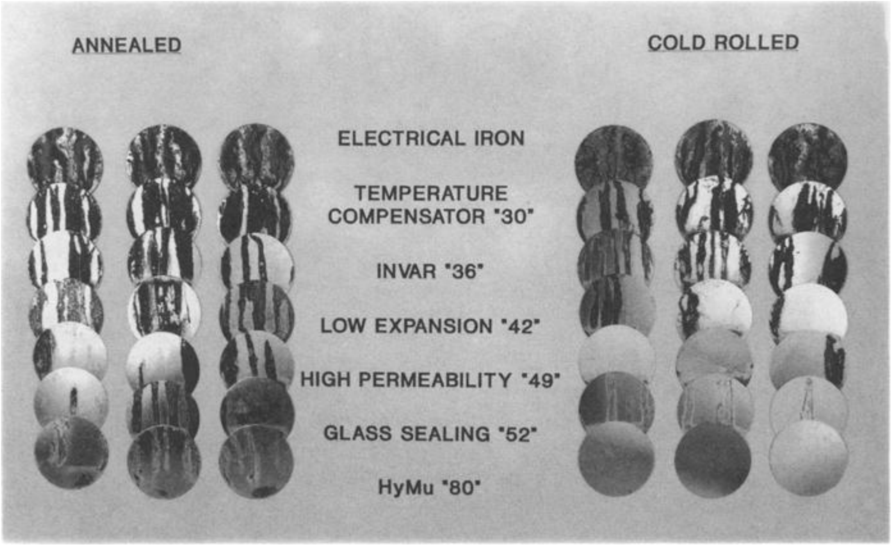

FIG. 3—*Salt spray (fog) test results on various nickel-iron alloys in both the annealed and cold-rolled condition: 5% neutral salt spray at 35°C (200-h duration). Triplicate specimens.*

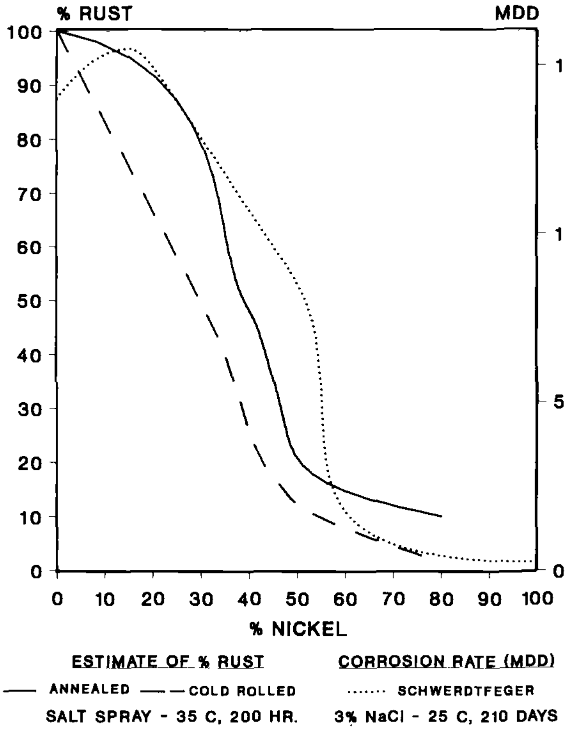

FIG. 4—*Dependence of percent of surface rusted and corrosion rate on nickel content using two different test methods. Note the sharp change in behavior at about 50% nickel.*

slightly lower rate of corrosion in the neutral salt spray test. The reason for this is unknown, although it may be the result of the intense deformation at the cold-rolled strip surface, which could minimize the number of corrosion initiation sites. Since many of the nickel-iron special alloys contain less than 50% nickel, the results clearly show the susceptibility of these alloys to general corrosion.

Improving the Corrosion Resistance of Special Alloys

It would be desirable to improve the intrinsic corrosion resistance of special alloys rather than relying on protective coatings, etc. Unfortunately, the options are rather limited since many of the characteristic properties of these alloys are rather unique and strongly composition dependent. Improving the overall cleanliness of these alloys is not a viable option since many are already vacuum melted using high-purity constituents. The only other recourse is to add chromium. This can be done in certain circumstances.

Many of the characteristic properties of nickel-iron alloys such as very high magnetic permeability or very low thermal expansivity are quite sensitive to alloy modification, and in most instances addition of large amounts of chromium render the alloy unsuitable for the application at hand. For example, the addition of 8% chromium to Invar "36" alloy (nominal 36% nickel) requires rebalancing the chemistry to a slightly higher nickel content (about 37% Ni) to achieve minimum thermal expansivity. However, the minimum expansivity attainable is more than three times higher than found in the binary alloy [*4*]. Such an increase is detrimental to many applications. Small amounts of chromium (1 to 3%) can be added, however, to some alloys without undue sacrifice in properties while gaining additional corrosion resistance to relatively mild environments. The addition of up to 12% chromium to nominal 50% nickel-iron high permeability alloy has been reported by Eriksson and Salwen [5]. Although a very substantial decline in saturation flux density was observed, the addition of 12% Cr resulted in considerable resistance to salt spray, and even small amounts of chromium are likely to confer increased resistance to more benign environments. Finally, it should be noted that it is possible to substitute chromium for vanadium in iron-cobalt high-saturation alloys and chromium for molybdenum in high-permeability 80% nickel-iron type alloys. Although the amounts of chromium permissible are small (<5%), some additional improvements in corrosion resistance are possible. Therefore, in mildly corrosive environments including normal atmospheric conditions, it may be possible to make small alloy compositional changes to improve the corrosion resistance to the point where protective coatings can be eliminated.

Stress-Corrosion Cracking

Stress-corrosion cracking can be a significant problem in both the manufacturing and use of thermostat alloys. Over the past 20 years the stress-corrosion cracking resistance of controlled expansion alloys has been evaluated in several test programs. Bolted U-bends have been used to produce stresses more severe than generally present in service applications. This provides an accelerated test except for those applications in which the material is similarly bent and restrained. Unless otherwise noted, all U-bends were bent to about 25 mm (1 in.) diameter using 2.5 to 3.8-mm (0.10 to 0.15-in.)-thick annealed material. This small variation in thickness did not appear important because all samples were plastically deformed and restrained. The as-machined U-bend specimens were typically about 98 mm (3.875 in.) long and were similar to sample blanks described in ASTM Practice for Making and Using U-Bend Stress Corrosion Test Specimens (G 30-90), Fig. 2, Example b. Test environments varied from distilled water to the severe 5 or 20% salt spray test. Tested specimens were evaluated using a X20 binocular microscope, and metallographic techniques were used as necessary to confirm the presence of cracks.

High Expansion 72 alloy has the highest thermal expansivity of any known metallic alloy and is widely used for the high expansion side of thermostat metals. It also can be highly prone to stress corrosion cracking as well as general corrosion. Surface ground U-bends of the alloy crack readily in room temperature tap water. Slightly improved resistance was observed in distilled water at room temperature, although transgranular stress corrosion cracking did occur. Tests have also been conducted in 95% humidity at 35°C (95°F) (no chloride) using material which had been reduced 50% by cold rolling. U-bends displayed improved resistance to stress-corrosion cracking (but not immunity) when coated with a mineral-based rolling oil. Despite this sensitivity, High Expansion 72 alloy has been fabricated and provided satisfactory service in a variety of applications without degradation due to stress-corrosion cracking. Apparently stresses encountered in fabrication and service are typically lower than those provided by the U-bend sample. Protection from aqueous environments is, however, required for heavily strained material. Oils may provide some protection, at least temporarily, but long-term use requires such techniques as nickel plating.

High Expansion 22-3 alloy offers improved stress-corrosion cracking resistance as compared to High Expansion 72 alloy, although the thermal expansivity is lower. This alloy is also widely used for the high expansion side of thermostat metals, although the flexivity of the bimetal is less due to the lower thermal expansivity of the High Expansion 22-3 alloy as compared to the High Expansion 72 alloy. The High Expansion 22-3 alloy resisted cracking in humidity and tap water, but was susceptible in the presence of chlorides and in an industrial environment unless the material was annealed after bending. This material has useful resistance, although protection from the environment or freedom from cold work is required for more severe applications.

Limited stress corrosion testing has also been conducted on nickel-iron low-expansion and glass sealing grades such as Invar "36", Low Expansion "42", and Glass Sealing 52 alloys (about 36, 40, and 50 wt% nickel, respectively). Based on work with Fe-Ni-Cr wires, increasing nickel from about 8% to about 45% eliminates cracking in boiling 42% magnesium chloride [*6*].

U-bends were produced from a 1.5-mm (0.058-in.)-thick cold-rolled strip of Invar "36" alloy and exposed to 20% salt spray at 35°C (95°F). Rusting and very shallow cracking occurred in as little as ten days. When similar material was annealed (furnace cooled) and exposed unstressed, no cracking was seen after 210 days. Additional Invar "36" alloy U-bends were immersed in 5% sodium chloride solution and in distilled water at 22°C (72°F) with and without oxygen sparging. The behavior of the oxygen-sparged sodium chloride solution was similar to that in salt spray. In the salt water test without sparging and in all distilled water tests, no cracking occurred. U-bends of Low Expansion "42" alloy annealed strip were exposed to 5% salt spray at 35°C (95°F). Stress corrosion cracking occurred between 100 and 700 h.

U-bends were produced from mill-annealed Glass Sealing 52 alloy by bending over a 19-mm (¾-in.)-diameter mandrel. When the specimens were exposed to 5% salt spray at 35°C (95°F), cracking occurred in less than 500 h. Similar U-bends were exposed for about six and one-half months in an outdoor steel mill environment with no cracking. The mill environment was apparently less severe than the salt spray test environment.

In summary, stressed nickel-iron alloys such as Invar "36", Low Expansion "42", and Glass Sealing 52 alloys are susceptible to stress-corrosion cracking when exposed to chlorides (and oxygen). Despite this, stress corrosion cracking is apparently not very common during actual use, presumably because the operating stresses are lower and the environments are less severe than those used in the laboratory.

Summary and Conclusions

The purpose of this work was to draw together information on the corrosion of magnetic, controlled expansion, and glass sealing alloys in an attempt to present a coherent picture of the corrosion resistance of these alloys. Most of these alloys do not exhibit significant resistance to even room temperature humidity. However, through proper alloy selection some current corrosion problems may be abated.

References

[*1*] Marsh, J. S., *The Alloys of Iron and Nickel, Vol. I—Special Purpose Alloys*, McGraw-Hill, New York, 1938, pp. 491–501.

[*2*] Boll, R., *Soft Magnetic Alloys*, Heyden & Sons, Ltd., London, 1979, pp. 316–317.

[*3*] Schwerdtfeger, W. T., *Journal of Research of the NBS*, Vol. 70C, No. 3, 1966, pp. 187–194.

[*4*] Saito, H. in *Physics and Applications of Invar Alloys*, H. Saito, Ed., Maruzen Co. Ltd., Tokyo, 1978, Chapter 22, pp. 514–519.

[*5*] Eriksson, H. and Salwen, A., *IEEE Transactions on Magnetics*, Vol. MAG-13, No. 5, September 1977, pp. 1451–1453.

[*6*] Copson, H.R., *Physical Metallurgy of Stress-Corrosion Fracture*," T. N. Rhodin, Ed., New York, Interscience Publishers, Inc., 1959, p. 256.

Sze-Shing Walter Yee[1] *and S. A. Bradford*[1]

The Influence of a Magnetic Field on Corrosion of Steel

REFERENCE: Yee, S.-S. W. and Bradford, S. A., "**The Influence of a Magnetic Field on Corrosion of Steel,**" *Corrosion of Electronic and Magnetic Materials, ASTM STP 1148,* P. J. Peterson, Ed., American Society for Testing and Materials, Philadelphia, 1992, pp. 90–101.

ABSTRACT: Magnetic influence has been suspected or reported as a contributing factor in many cases of metallic corrosion near magnetic sources. This study has examined the corrosion behavior of a plain-carbon steel in a 3% sodium chloride (NaCl) solution within and without magnetic fields up to 0.245 T at room temperature. Anode and cathode corrosion half-cells were separated so that the magnetic effect on each electrode reaction could be studied by itself. Direction of the field with respect to the electrode surfaces was also varied.

Cathodic polarization of steel is not affected by a magnetic field; neither is anodic polarization up to a current density of approximately 10 mA/cm^2. It was also found by cyclic polarization that a magnetic field does not affect the susceptibility of the steel to localized attack in a 3% NaCl solution. However, at extreme corrosion rates (more than 24 cm/year), an applied magnetic field of 0.245 T causes a maximum change of 2.7% in the anodic dissolution rate.

KEY WORDS: electrochemical corrosion, carbon steels, magnetic fields, anodes, cathodes, reaction kinetics, electrolytic cells, pitting

In many engineering applications, metals are used within magnetic fields of various strengths and are exposed to a corrosive environment at the same time. Research results going back well over a century proved to be contradictory and often inconclusive in regard to the existence of an influence exerted by a magnetic field on electrochemical reactions involving metals. Most recent studies agree that there can be some influence, primarily due to changes in the mass transfer of reactant or reaction product [*1,2*]. Changes in mass transport arise as a result of solution flow induced by magnetohydrodynamics, the interaction of the electric current in the solution and the applied magnetic field [*3–10*].

On the other hand, the possibilities of direct effects by the magnetic field have not been ruled out. Such effects include altering the Gibbs energy of reaction, ΔG, to give different products or different yields [*11,12*], or changing the mechanism path so that the activation energy, ΔG^*, is affected.

It is still uncertain whether enhancement [*3–10*], retardation [*13*], or both [*14*] are the result of magnetic electrochemical interactions. The significance of magnetic field directions [*15–17*] has not been clearly decided. Most importantly, few of the investigations conducted have examined the magnetic effect on metal corrosion from an electrode kinetics point of view.

This study separates the anodic and cathodic reactions so that only one of the half reactions is subjected to a magnetic field at any one time. The direction of the applied field relative to the electrode surface is considered to establish the significance of field direction. Only the effects of a stable magnetic field are studied in the present work.

---

[1] Former graduate student and professor of metallurgy, respectively, Department of Mining, Metallurgical and Petroleum Engineering, University of Alberta, Edmonton, Alberta T6G 2G6, Canada.

Experimental

Magnet

The magnet employed in this study was a water-cooled 7500-W electromagnet. Poles were tapered from the core diameter of 10 cm (4 in.) to a 5-cm (2-in.) diameter at the pole tips with a pole gap of 10.8 cm (4.25 in.) to accommodate the corrosion cell containing the specimen. The magnet was calibrated with a gaussmeter to show a linear change in magnetic field strength with d-c coil current, both at the pole faces and at the center between the poles up to 0.26 T.

Corrosion Cells

Two identical corrosion cells contained the working and counter electrodes separately in the experiment. The cells were designed in such a way that the working electrode (specimen) was always positioned in the middle between the two magnetic poles. This was the case regardless of the orientation of the cell relative to the magnetic poles. The two half-cells were electrolytically connected by a 60-cm (24-in.)-long salt bridge having an equivalent current-carrying capacity of approximately 55 mA.

The half-cell containing the counter electrode was shielded from any stray field from the electromagnet by a steel plate. The magnetic shield was a 0.63-cm (0.25-in.)-thick, low-carbon steel plate with a width and height of 40 cm (16 in.). There was a slot in the middle of the shield for the salt bridge connecting the two half-cells to pass through.

Electrodes and Electrolyte—The specimen used was a 1.3-cm (0.5 in.)-thick, low-carbon steel disk with a diameter of 5 cm (2 in.) cut from a cold-rolled bar, which had been fully annealed to give the most homogeneous and the best magnetic properties. A chemical analysis of the steel was performed and the results are given in Table 1. The specimen was mounted in an epoxy resin holder exposing only one of the flat surfaces. During the experiment, only a circular area of approximately 1 cm^2 in the middle of the specimen was exposed to the electrolyte while the rest of the flat surface was covered with an acid-resistant lacquer. The large specimen was used to eliminate edge effects of the magnetic field and thus to ensure a uniform magnetic field strength near the corroding area of the steel.

TABLE 1—*Chemical analysis of the steel sample.*

Element	Weight, %
Aluminum	0.012
Carbon	0.14
Chromium	0.11
Cobalt	0.005
Columbium	0.000
Copper	0.24
Lead	0.004
Magnesium	0.04
Manganese	0.72
Molybdenum	0.012
Nickel	0.07
Silicon	0.18
Sulfur	0.023
Tin	0.010
Titanium	0.000
Zirconium	0.011
Iron	Balance

The counter electrode was a 50-cm (20-in.)-long platinum wire, coiled 20 times for compactness and ease of handling.

The reference electrode used was a saturated calomel electrode (SCE) in a Luggin probe which allowed electrical contact between the reference electrode and the corrosion cell electrolyte without the danger of contaminating the SCE.

A 3% sodium chloride (NaCl) solution, pH 6.68, made with ACS analytical grade salt and doubly distilled water, was used as the electrolyte in this experiment. The solution was chosen for the ease of making and handling of the solution and the relative simplicity of the system. Deaeration of the solution in both electrode compartments was accomplished by purging with 99.93% nitrogen gas for at least 75 min prior to and during each experiment. The N_2 was not analyzed but typically contained 10 to 20 ppm O_2 according to the supplier.

Sample Preparation

To ensure good reproducibility of the experiment, the same specimen was prepared exactly the same way prior to each run. The specimen was first hand-ground on a series of four successively finer silicon carbide (SiC) abrasive strips of 240, 320, 400, and 600 grits.

Upon completion of polishing, the specimen was subjected to an ultrasonic cleaning in 99% pure acetone for 10 min to remove any trace of foreign matter adhering to the surface.

The specimen was then removed and rinsed with 99.5% pure acetone. The dried specimen was then coated with lacquer.

Testing Procedures

After placing the specimen in its electrode compartment and complete deaeration of the solution, the rest potential of the steel was measured with the electrometer of the potentiostat. All tests were made at room temperature, 19 to 24°C (66 to 75°F).

Two methods of maintaining the solution oxygen free were used in the working electrode cell. The first one was by continuing the bubbling of nitrogen gas in the solution, which obviously had a stirring effect on the solution. The second method, which did not cause any solution turbulence, was done by maintaining a positive pressure of nitrogen gas in the cell above the liquid level. This kept air from entering the cell without disturbing the solution.

After the specimen rest potential had been obtained, a potentiostat with a function generator was used to change the applied potential on the working electrode. A standard scan rate of 10 mV/min was used to increase or decrease the potential applied while current measurements were taken as a function of the potential. A linear/logarithmic interface converted the current output signal to logarithmic signals for the plotter to obtain graphs of applied potential (SCE) versus the log of cell current.

In addition, current measurements were also taken directly from the potentiostat with a digital multimeter. These direct values of the cell current were used to calculate the current density at the working electrode surface.

For cathodic polarization, the applied potential to the working electrode was decreased from the rest potential to a value of -1000 mV (SCE) at the standard rate. For anodic polarization the applied potential was increased until it reached -450 mV where the corresponding cell current density was approximately 10 mA/cm^2.

The susceptibility of the specimen to localized corrosion attacks was determined by cyclic polarization involving the gradual decrease of the applied potential at the end of an anodic polarization run. This technique determines the characteristic potentials marking the potential range within which a metal is susceptible to localized attacks. The nucleation potential or pitting potential, E_{np}, is the potential above which pits nucleate and develop. E_{pp} is the protection potential, the potential below which no pitting can occur and above which existing pits can maintain growth. Therefore, the range in potential between E_{np} and E_{pp} gives an indication of the susceptibility of the specimen to localized attacks. E_{np} is marked by the sudden increase in current density in the forward branch of the anodic polarization curve while E_{pp} is the potential at which the return portion crosses the forward portion of the cyclic curve. For this experiment, when the cell potential reached -450 mV, the potential was decreased at the same rate of 10 mV/min to obtain the return portion of the cyclic potentiodynamic measurements.

When the effects of an applied magnetic field were studied, the entire half-cell containing the working electrode was placed between the poles of the electromagnet. Four directions were examined, and they were achieved by accordingly orientating the half-cell between the magnetic poles or reversing the current direction in the magnetic coils of the magnet. For convenience, these field directions were each assigned a number so that they could be referenced in the text. Figure 1 shows the designated numbers corresponding to the field directions. Regardless of the relative field direction, the specimen was always positioned exactly in the middle

Description	Diagram	Designated No
Into the surface	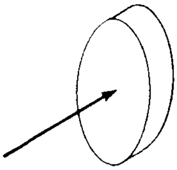	1
Out of the surface	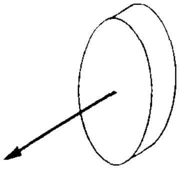	2
Parallel to the surface, From left to right	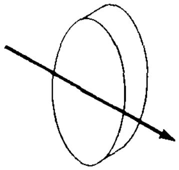	3
Parallel to the surface, From right to left	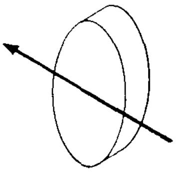	4

Magnetic field lines from N-pole to S-pole

FIG. 1—*Definition of magnetic field direction.*

between the poles. In addition to the no-field situation, magnetic field strengths of 0.037, 0.093, 0.141, and 0.245 T were used.

To determine the effect of a magnetic field at extreme corrosion rates, the steel specimen was anodically polarized for 1 h at a potential of −250 mV (SCE) to yield a high corrosion current density (more than 20 mA/cm^2). The effects of the magnetic field on such severe corrosion were examined by applying a magnetic field in different directions and at various strengths.

Results and Discussion

Potentiodynamic Cathodic Polarization

The shape of the polarization curves (Figs. 2–4) indicates that there is no concentration polarization for the cathodic reaction under the experimental conditions. This is expected because the solution was constantly stirred by the bubbling action of the nitrogen used to keep the solution oxygen free. In addition, in the absence of oxygen, the cathodic reaction is primarily the decomposition of water

$$2H_2O + 2e^- \rightarrow H_2 + 2OH^-$$

Obviously, the diffusion of H_2O molecules in the aqueous solution is not a concern here.

Figure 2 shows the results obtained for the same experiment with application of a magnetic field to the cathode half-cell at three different strengths compared with one of the runs without a magnetic field. The magnetic field lines were going in a left-to-right direction parallel to the specimen surface (Direction 3). Figure 3 examines the effect of field orientation at a field strength of 0.037 T. As shown in the two figures, there is no significant variation in the results. The values obtained for the Tafel slope of cathodic polarization of the steel in the test solution deaerated by nitrogen gas bubbling are shown in Table 2. The Tafel slopes ranged from

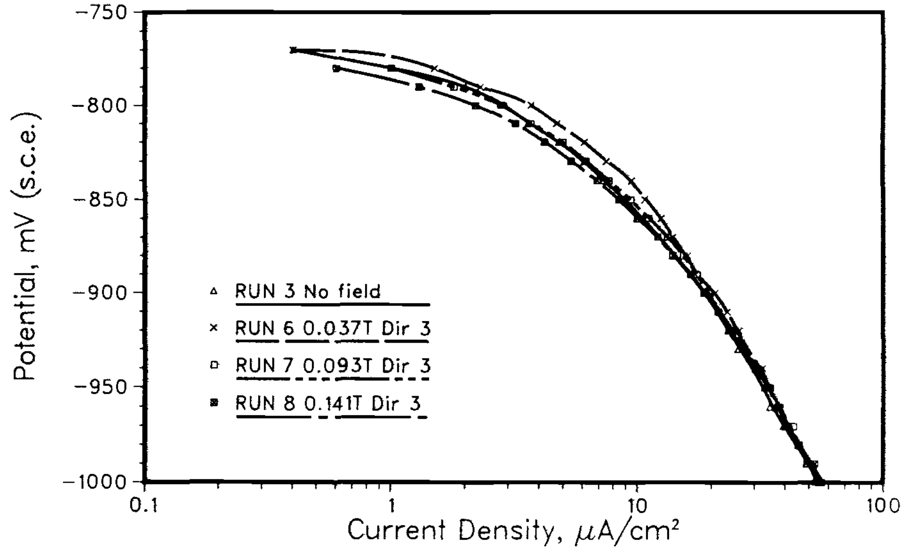

FIG. 2—*Potentiodynamic cathodic polarization at 10 mV/min for steel in deaerated 3% NaCl solution with stirring in magnetic fields of different strengths.*

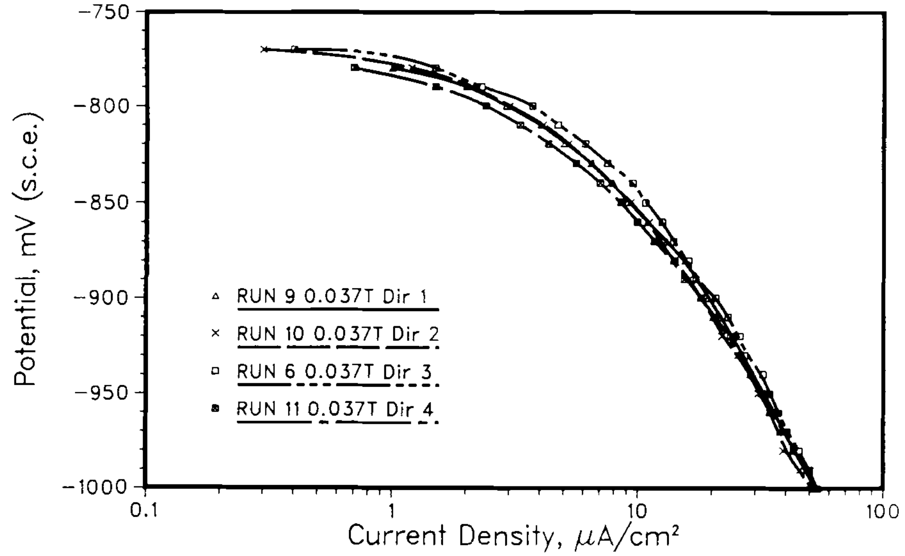

FIG. 3—*Potentiodynamic cathodic polarization at 10 mV/min for steel in deaerated 3% NaCl solution with stirring in magnetic fields of different directions.*

−0.166 to −0.153 V without a magnetic field and from −0.167 to −0.148 V when a magnetic field was applied. The Tafel slope values are therefore shown to be close between the cases without and with a magnetic field. Most importantly, no trend can be observed from the results that may suggest the presence of an influence by the magnetic field on the cathodic reaction kinetics. Therefore it is evident that the effect of the magnetic field, if any, is not detectable by

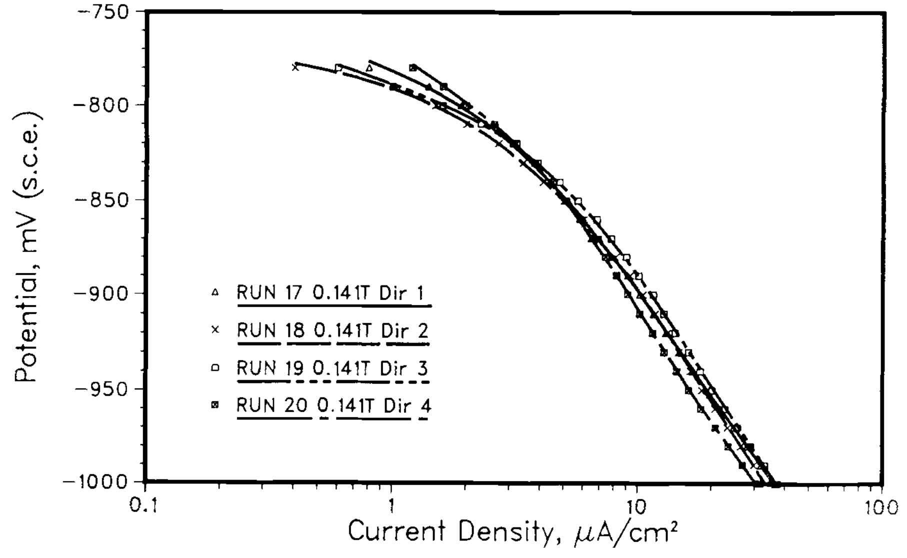

FIG. 4—*Potentiodynamic cathodic polarization at 10 mV/min for steel in deaerated 3% NaCl solution with no stirring in magnetic fields of different directions.*

TABLE 2—*Tafel slope values from potentiodynamic cathodic polarization of steel in deaerated 3% NaCl solution.*

	Magnetic Field		
Run Number	Strength, T	Direction	Tafel Slope, V per Decade
	WITH NITROGEN BUBBLING		
1	0.000	. . .	−0.153
2	0.000	. . .	−0.163
3	0.000	. . .	−0.153
4	0.000	. . .	−0.166
5	0.000	. . .	−0.159
6	0.037	3	−0.167
7	0.093	3	−0.155
8	0.141	3	−0.148
9	0.037	1	−0.154
10	0.037	2	−0.165
11	0.037	4	−0.157
	WITH NITROGEN BLANKET		
12	0.000	. . .	−0.169
13	0.000	. . .	−0.142
14	0.000	. . .	−0.162
15	0.037	1	−0.153
16	0.093	1	−0.160
17	0.141	1	−0.164
18	0.141	2	−0.165
19	0.141	3	−0.163
20	0.141	4	−0.187

this technique. These results show that the electrode kinetics of the cathodic reaction on steel in the test solution is not measurably affected by the presence of a magnetic field of strength up to 0.141 T.

Figure 4 compares the result of cathodic polarization in stagnant solution under zero magnetic field with those with different field directions at the same field intensity. It indicates that a magnetic effect is not detectable in the cathodic polarization of steel in stagnant deaerated solution. The Tafel slope values obtained in this group of experiments are shown in Table 2 as well. When no magnetic field was applied, the slope values ranged from −0.169 to −0.142 V, while with an applied field they ranged from −0.165 to −0.153 V. This demonstrates that no significant effect on the cathodic electrode kinetics could be detected as a result of the applied magnetic field. As discussed, the reaction in this case is entirely activation controlled, and consequently it can be concluded that there is no influence exerted by the magnetic field on the reaction mechanism in the decomposition of water on the steel surface.

Potentiodynamic Anodic Polarization

The results of three runs of anodic polarization with no applied magnetic field are shown in Fig. 5. The three curves generally show good agreement, indicating good experimental reproducibility. The curves all show passivation of the steel specimen between −630 and −550 mV. The degree of passivation is small (less than 2.5 times in current density reduction) and therefore implies a weakly protective corrosion film. The more widely spread current densities

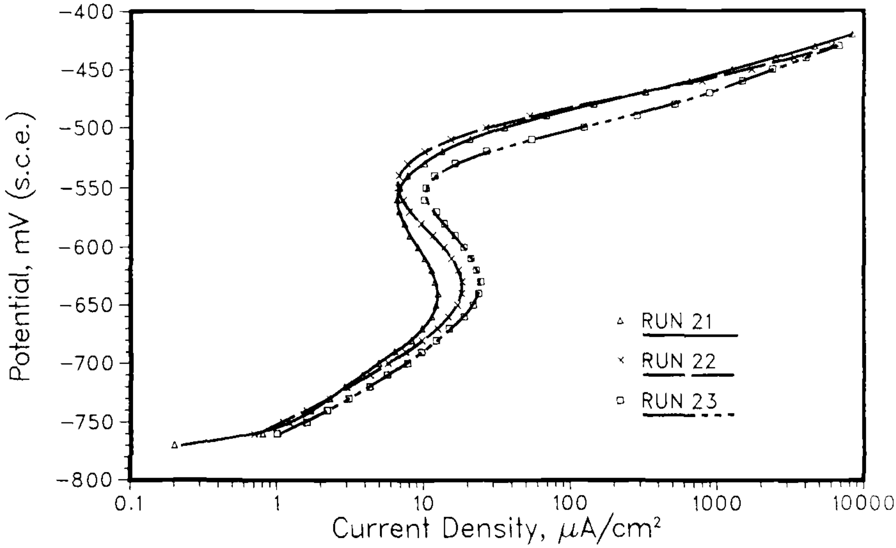

FIG. 5—*Potentiodynamic anodic polarization at 10 mV/min for steel in deaerated 3% NaCl solution with stirring and no magnetic field.*

in this potential range among the three runs are primarily due to the fact that the passivation film is unstable. In fact, in most potentiodynamic polarization tests the current densities in any passive range of the sample all show a higher degree of scatter. An examination of the iron-water Pourbaix diagram [*18*] shows that the film is probably Fe_3O_4, which is not very protective. Also, formation of iron oxide (Fe_3O_4) is more likely than $FeO \cdot (OH)$ or $Fe_2O_3 \cdot H_2O$ because of the limited oxygen supply.

The results of application of a magnetic field at three different strengths in the same direction and in four different directions on the anodic polarization of the specimen are graphically represented in Figs. 6 and 7, respectively. The shapes of the curves are essentially identical. The larger variations in current densities in the passivation potential range are also similar to the no-field situation. As shown in Table 3, the values of the Tafel slope of anodic polarization of the specimen varied from 0.088 to 0.084 V without a magnetic field and from 0.086 to 0.077 V when a field was applied. This shows no appreciable difference in the corrosion kinetics due to the presence of the field. It is then evident that the anodic reaction rate of steel in the test solution is not significantly affected by the presence of a magnetic field. In addition, the passivation of the metal, though only slight, is also unchanged or changed to an undetectable extent by the magnetic field.

Cyclic Polarization

Results of cyclic polarization are listed in Table 4. The protection potential, E_{pp}, showed a maximum variation of 40 mV, which is relatively minimal in a test of this nature. The relatively low protection potential (less than 100 mV above the rest potential) suggests that localized attacks can be maintained easily on steel in the solution. This is quite apparent as chloride ions can readily dissolve any corrosion product film on steel.

Most importantly, no difference in the value of the protection potential was obtained as a result of the presence of the applied magnetic field.

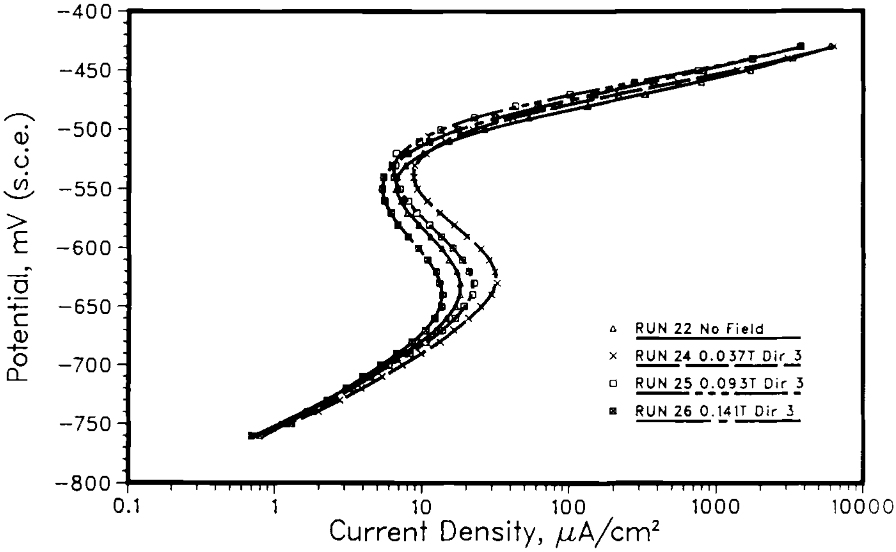

FIG. 6—*Potentiodynamic anodic polarization at 10 mV/min for steel in deaerated 3% NaCl solution with stirring in magnetic fields of different strengths.*

Magnetic Effects on Severe Corrosion

At a potential of −250 mV, the corresponding anodic current density of steel in aerated 3% NaCl solution is approximately 22 to 23 mA/cm^2, which equals a penetration rate of more than 24 cm/year, assuming uniform attack with oxidation of the metal to Fe^{2+}. Table 5 shows that at such high corrosion rates a magnetic field has a very small (2.7% maximum) but detect-

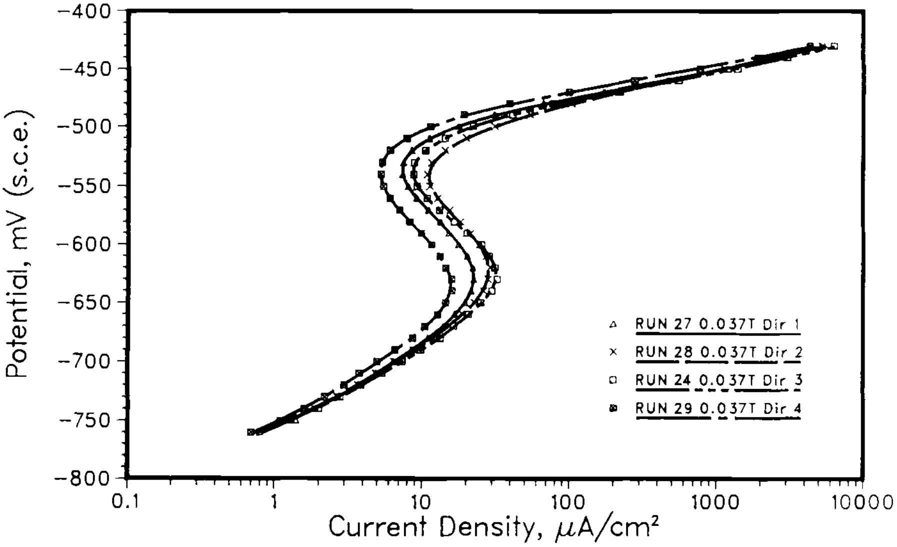

FIG. 7—*Potentiodynamic anodic polarization at 10 mV/min for steel in deaerated 3% NaCl solution with stirring in magnetic fields of different directions.*

TABLE 3—*Tafel slope values from potentiodynamic anodic polarization of steel in deaerated 3% NaCl solution.*

Run Number	Magnetic Field Strength, T	Magnetic Field Direction	Tafel Slope, V per Decade
21	0.000	. . .	0.088
22	0.000	. . .	0.084
23	0.000	. . .	0.085
24	0.037	3	0.077
25	0.093	3	0.080
26	0.141	3	0.084
27	0.037	1	0.086
28	0.037	2	0.085
29	0.037	4	0.086

TABLE 4—*Cyclic potentiodynamic polarization results of steel in deaerated 3% NaCl solution.*

Run Number	Nucleation Potential, mV	Protection Potential, mV
21	−550	−700
22	−550	−730
23	−550	−740
24	−560	−720
25	−560	−730
26	−550	−690
27	−560	−710
28	−560	−720
29	−560	−740

TABLE 5—*Effect of a magnetic field on severe corrosion.*[a]

Run	Magnetic Field Strength, T	Magnetic Field Direction	Current Density, mA/cm² No Field	Current Density, mA/cm² With Field	Current Density, mA/cm² % Difference
6	0.245	Specimen back to S-pole	22.98	22.42	−2.4%
7	0.245	Specimen back to S-pole	22.87	22.51	−1.6%
8	0.245	Specimen back to S-pole	22.13	21.53	−2.7%
9	0.141	Specimen front to S-pole	22.23	22.33	+0.4%
10	0.141	Specimen front to S-pole	22.76	22.93	+0.7%
12	0.141	Specimen front to S-pole	22.91	23.16	+1.1%
13	0.141	3	22.81	22.83	Negligible
14	0.141	3	22.62	22.61	Negligible
15	0.141	4	23.03	23.00	−0.1%
16	0.141	4	22.84	22.86	Negligible

[a] Anodic potential: −250 mV (SCE); solution temperature: 22 to 23°C (72 to 73°F).

able effect on reaction rate. Also, the orientations of the field relative to the corroding surface show definite effects.

At a field strength of 0.245 T with the anode positioned in such a way that the field is attracting magnetic substance towards the electrode surface (Runs 6 to 8), a decrease of up to approximately 2.7% in the current density is obtained. A slow stirring of the electrolyte was also observed during the experiment. On the other hand, the current density is slightly increased (by 1.1%) when the field is attracting magnetic substances away from the electrode surface (Runs 9 to 12). The influence by a transverse magnetic field (Runs 13 to 16) is somewhat unclear.

This experiment then verifies that direct magnetic attraction can alter the anodic reaction rate of steel to a measurable but extremely small extent. From an engineering point of view, a 2.7% difference at a corrosion rate of over 24 cm/year can definitely be regarded as less than significant. Also, the direction of the applied field can determine the direction of the minute, but detectable, change in the rate of corrosion under the experimental conditions.

Conclusions

A survey of literature available on electrochemical reactions involving metals indicates that reaction rate enhancement is primarily due to electromagnetic-induced solution flow. Solution motion increases the mass transfer of reacting species and thus reduces concentration polarization of the electrode surface. Previous work has been unable to prove or to disprove the possibility of direct magnetic effects on the reaction mechanism in metal electrochemical reactions.

The following conclusions are the main findings of the present work:

1. Cathodic polarization of a plain-carbon steel in deaerated 3% NaCl solution at room temperature is activation controlled and is not affected by the presence of a magnetic field up to 0.141 T applied in the four directions examined.
2. Anodic polarization of the steel up to −450 mV (SCE) with a corresponding current density of approximately 10 mA/cm^2 is not affected by an external magnetic field up to 0.141 T in the four directions tested.
3. The susceptibility of the steel to localized attacks in 3% NaCl solution is not affected by the presence of a magnetic field up to 0.141 T.
4. An applied magnetic field (up to 0.245 T) causes a maximum change of 2.7% in the anodic reaction rate of the steel in an aerated 3% NaCl solution at extreme corrosion rates (more than 24 cm/year).

Consequently, the corrosion of a plain-carbon steel in a 3% NaCl solution is not affected to any significant extent by magnetic fields of up to 0.245 T at room temperature.

References

[1] Sagawa, M., *Transactions,* Japan Institute of Metals, Vol. 23, No. 1, 1982, pp. 38–40.
[2] Ghabashy, M. A., *Corrosion Prevention and Control,* Vol. 35, No. 3, 1988, pp. 73–75.
[3] Mohanta, S. and Fahidy, T. Z., *Canadian Journal of Chemical Engineering,* Vol. 50, 1972, pp. 248–253.
[4] Fahidy, T. Z., *Electrochemica Acta,* Vol. 18, 1973, pp. 607–614.
[5] Mohanta, S. and Fahidy, T. Z., *Electrochemica Acta,* Vol. 19, 1974, pp. 771–775.
[6] Mohanta, S. and Fahidy, T. Z., *Electrochemica Acta,* Vol. 19, 1974, pp. 835–840.
[7] Mohanta, S. and Fahidy, T. Z., *Electrochemica Acta,* Vol. 19, 1974, pp. 149–152.
[8] Mohanta, S. and Fahidy, T. Z., *Journal of Applied Electrochemistry,* Vol. 6, 1976, pp. 211–220.

[9] Mohanta, S. and Fahidy, T. Z., *Journal of Applied Electrochemistry,* Vol. 8, 1978, pp. 5–10.
[10] Iwakura, C., Edamota, T., and Tamura, H., *Denki Kagaku oyubi Butsuri Kagaku,* Vol. 52, No. 10, 1984, pp. 654–658.
[11] Parson, A. L., *Nature,* Vol. 50, No. 3812, 1942, pp. 605-606.
[12] Peev, T., Mandjukova, B., and Mandjukova, I., *Corrosion,* Vol. 43, No. 12, 1987, pp. 739–742.
[13] Srivastava, K. and Nigam, N., *British Corrosion Journal,* Vol. 23, No. 3, 1988, pp. 172–175.
[14] Ghabashy, M. A., *Anti-Corrosion Methods and Materials,* Vol. 35, No. 1, 1988, pp. 12–13.
[15] Ogawa, Y., Hisamatsu, Y., and Moriya, A., *Nippon Kinzoku Gakkai-shi,* Vol. 16, 1952, pp. 194–198.
[16] Hanszen, K. J., *Zeitschrift für Naturforshung,* Vol. 9a, 1954, pp. 919–929.
[17] Feller, H. G. and Kesten, M., *Corrosion Science,* Vol. 9, 1969, pp. 43–51.
[18] Pourbaix, M., *Atlas of Electrochemical Equilibria in Aqueous Solutions,* National Association of Corrosion Engineers, Houston, 1974, p. 312.

Chuen H. Lee,[1] *David A. Stevenson,*[1] *Lichung C. Lee,*[2] *Richard D. Bunch,*[2] *Robert G. Walmsley,*[3] *Mark D. Juanitas,*[3] *Edward Murdock,*[3] *and James E. Opfer*[3]

Electrochemical and Structural Characterization of Permalloy

REFERENCE: Lee, C. H., Stevenson, D. A., Lee, L. C., Bunch, R. D., Walmsley, R. G., Juanitas, M. D., Murdock, E., and Opfer, J. E., "**Electrochemical and Structural Characterization of Permalloy,**" *Corrosion of Electronic and Magnetic Materials, ASTM STP 1148,* P. J. Peterson, Ed., American Society for Testing and Materials, Philadelphia, 1992, pp. 102–114.

ABSTRACT: The objective of this study is to characterize the passive behavior of electroplated permalloy films (EP) and bulk permalloy samples. The motivation for this work is the optimization of the magnetic properties of these films consistent with the required etching steps used in the fabrication of read/write thin film magnetic heads and the corrosion behavior of these heads in service conditions. The different samples of permalloy were evaluated with electrochemical potentiodynamic anodic polarization (PAP) at different scan rates in electrolytes with various pH and chloride content. The most significant difference in the passive behavior of the two types of samples was the predominantly active behavior of the EP samples, in contrast to a classic passive behavior of the bulk samples. The structure of EP permalloy was evaluated with EPM, XRD, and TEM in order to explain the difference in passive behavior. The most significant difference was the columnar grain structure with 20 to 30 nm in diameter by 100 nm in length and a (200) texture for the EP films.

KEY WORDS: thin films, permalloy, corrosion, potentiodynamic polarization, anisotropy, microstructure

The use of permalloy as a soft magnetic read/write element in recording heads has motivated a number of studies of the corrosion of thin films of nickel-iron (Ni/Fe) alloys with the permalloy composition (~80/20 at% Ni/Fe) [*1–10*]. The electrochemical passivity characteristics of this alloy provide a basis for predicting corrosion behavior as well as etching behavior of permalloy films, an essential step in the planar processing of "thin-film" heads. The present study concerns the electrochemical passive behavior of electroplated permalloy films, which is the form of the alloy typically used in recording heads. For comparison, the behavior of cast "bulk permalloy" samples was also studied. Potentiodynamic anodic polarization methods were used to establish the primary passive potentials, the passive current densities, and the pitting potentials, with their dependence on the pH and the chloride ion concentration. A major objective of the present study was to relate any differences in the passive behavior to the structure of the alloy and, to this end, we have characterized the surface morphology, the compositional homogeneity, and the crystallography of the relevant permalloy samples.

[1] Department of Materials Science and Engineering, Stanford University, Stanford, CA 94305.
[2] IBM/SSPD, 5600 Cottle Rd., San Jose, CA 95193.
[3] Hewlett Packard-HPL, Palo Alto, CA 94304.

Experimental Methods and Materials

The bulk cast samples were taken from a 12-in. (30.48 cm) permalloy sputtering target, and the electroplated permalloy thin films (EP) were prepared at International Business Machines, Storage Systems Product Division. The bulk samples were mechanically polished using a colloidal silica polishing solution (0.05 μm). Prior to the electrochemical testing, both specimens were degreased with electronic grade 1,1,1-trichloroethane and acetone in an ultrasonic cleaner, washed with isopropyl alcohol in an ultrasonic cleaner, and dried with a nitrogen jet.

For the electrochemical studies, a modified EG&G PAR Model K0235 flat cell was used. The test area of this cell is 1 cm^2. An EG&G PAR Model 342-2 SoftCorr corrosion measurement system, which contains Model 342C SoftCorr corrosion measurement software, a Model 273 potentiostat/galvanostat, National Instrument MCGPIB card, and an IBM PS/2 Model 55SX computer system with color monitor, was used to study etching, homogeneous corrosion, and pitting corrosion behavior.

The passive properties of the samples were established using potentiodynamic anodic polarization (PAP), and the following parameters were measured: corrosion potential, passive current density, and pitting potential. Three different scan rates were used to establish the influence of scan rate on the results: 1, 5, and 10 mV/s. The reported values are for a scan rate of 1 mV/s. This rather rapid scan rate was necessary in order to complete a scan before the film was etched through in spots. We have shown, however, that such scan rates produce results that correlate very well with corrosion rates that are obtained by long-term environmental testing [*10*]. The influence of the pH and the chloride ion concentration was established using the electrolytes described in Table 1, which were prepared from reagent grade chemicals and deionized water. To minimize the influence of dissolved oxygen, we followed the standard practice of removing most of the oxygen by bubbling purified nitrogen through the solution for 5 min prior to the experiment. The electrode potential was measured against a saturated calomel electrode (SCE).

The structure of the samples was characterized using X-ray diffraction (XRD), scanning electron microscopy, X-ray microanalysis, electron probe microanalysis (EPMA), and transmission electron microscopy (TEM). The crystal structure, lattice parameter, degree of texture, and grain size was obtained employing X-ray diffraction (XRD) using powder diffraction methods with a standard Bragg-Brentano method [*11*] using Cu-Kα radiation in an automated Huber diffractometer.

Scanning electron microscopy (SEM) was used to study the surface topography. The quantitative X-ray composition microanalysis was conducted by the wavelength-dispersive spectroscopy (WDS) mode with ZAF correction (Z-atomic number, A-absorption within the sample and detector, and F-X-ray induced fluorescence within the sample). SEM and WDS information was obtained from JEOL-733 EPMA (electron probe microanalysis).

TABLE 1—*Electrolytes used for this study.*

Electrolyte Compositions			pH
0.1 *M* K_2SO_4		. . .	5.90
0.1 *M* K_2SO_4	+	0.01 *M* KCl	5.91
0.1 *M* K_2SO_4	+	0.1 *M* KCl	5.93
0.1 *M* K_2SO_4	+	1.0 *M* KCl	6.09
0.1 *M* K_2SO_4	+	0.0001 *M* H_2SO_4	4.37
0.1 *M* K_2SO_4	+	0.0005 *M* H_2SO_4	3.54
0.1 *M* K_2SO_4	+	0.01 *M* H_2SO_4	2.36

Transmission electron diffraction was employed to establish whether there were any small amounts of phases that could not be detected by XRD. The bright field and dark field images were used to study the grain sizes and morphology. Cross-section samples were also studied to compare the crystal structure, the grain size, and the morphology of sputtered seed layer and electroplated layer. The TEM information was obtained with a Philips EM400 and EM430.

Results and Discussions

Effect of Scan Rate

The effect of scan rate on PAP behavior of both bulk permalloy and electroplated permalloy thin film displayed predictable behavior. The lower scan rates produce higher corrosion potentials, smaller passive current densities, and lower pitting potentials for both types of samples. The lower scan rates produce smaller passive current densities, since there is more time to form the passivating reaction, and lower pitting potentials, since there is more time for pit nucleation and growth. There are two possible explanations for higher corrosion potentials (i.e., the potential at zero net current) with lower scan rates. One explanation assumes the same cathodic behavior for different scan rates coupled with the smaller passive current densities of the lower scan rates, producing a higher corrosion potential. The other explanation concerns the passivating characteristics of the electrolyte 0.1 M potassium sulfate (K_2SO_4) (M = mol/litre = kmol/m^3 = 10^3 mol/m^3 in tables and figures)—that produce passive films that require a longer cathodic treatment or a higher activation potential to activate the permalloy surface.

Influence of Chloride Ion Concentration

Three different potassium chloride (KCl) concentrations have been superimposed on the 0.1 M K_2SO_4 electrolyte: 0.01 M KCl; 0.1 M KCl; and 1.0 M KCl. Figure 1 shows the PAP results of bulk permalloy and electroplated permalloy thin films. The higher chloride ion concentration develops lower pitting potentials (Table 2), which is consistent with the normally observed trends. However, the passive current densities are impressively low and do not depend on the presence of chloride ion in the electrolyte. These observations imply that a stable passive layer is formed in the presence of the chloride ions and that pitting corrosion is initiated at the respective pitting potentials.

Influence of pH

The influence of pH on the passive behavior was investigated using three electrolytes of pH (2.36, 3.54, and 4.37) prepared by mixing appropriate amounts of H_2SO_4 and 0.1 M K_2SO_4. Figure 2 and Table 3 show the PAP results for the electroplated and the bulk samples. For the bulk (cast) samples, the passive current densities increase with decreasing pH, and there are well-defined transitions from active to passive regimes. The onset of a transpassive regime increases for decreasing pH. The shift of the anodic polarization curves to more positive potentials and higher current densities with decreasing pH shows the influence of hydrogen and hydroxyl ions on both metal dissolution and on passive film formation. The passive film formation requires a combination of oxidation, nucleation of an hydroxide, and dehydration. The electroplated permalloy samples show similar anodic polarization behavior to bulk permalloy in the 0.1 M K_2SO_4 electrolyte and in the electrolytes of different chloride ion concentrations; however, its behavior is quite different in electrolytes with small amounts of H_2SO_4. The electroplated permalloy film shows only active behavior in electrolytes with small sulfuric

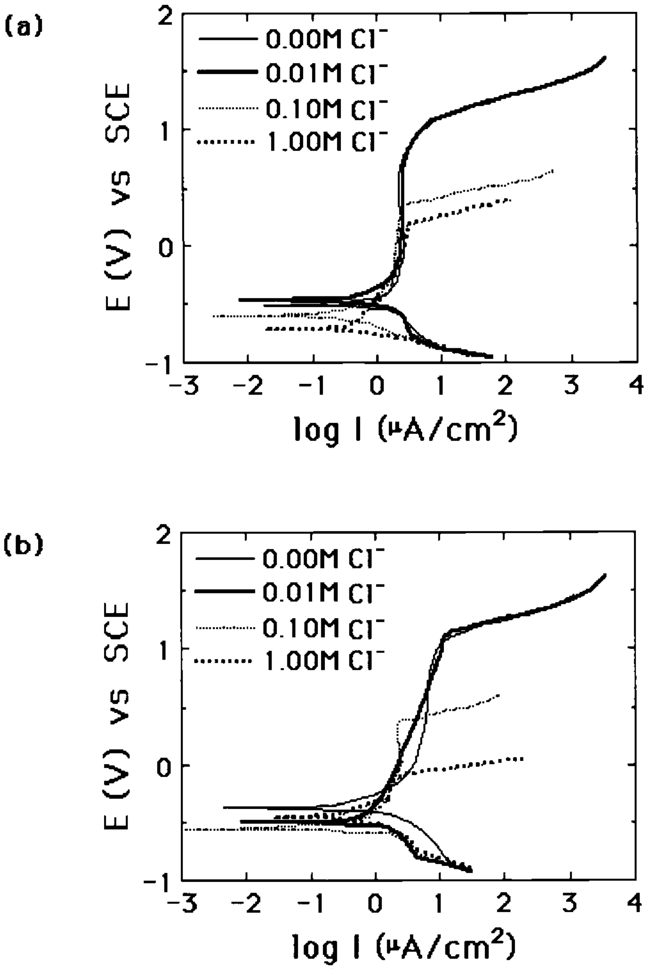

FIG. 1—*Effect of* [Cl^-] *on PAP of* (a) *bulk and* (b) *plated permalloys at 1 mV/s scan rate.*

TABLE 2—*Pitting potentials of bulk and plated permalloy in electrolytes with different* Cl^- *concentrations.*

[Cl^-], kmol/m^3	Pitting Potential Versus SCE, V	
	Bulk	Plated
0.00	1.025	1.125
0.01	1.025	1.150
0.10	0.363	0.362
1.00	0.175	−0.125

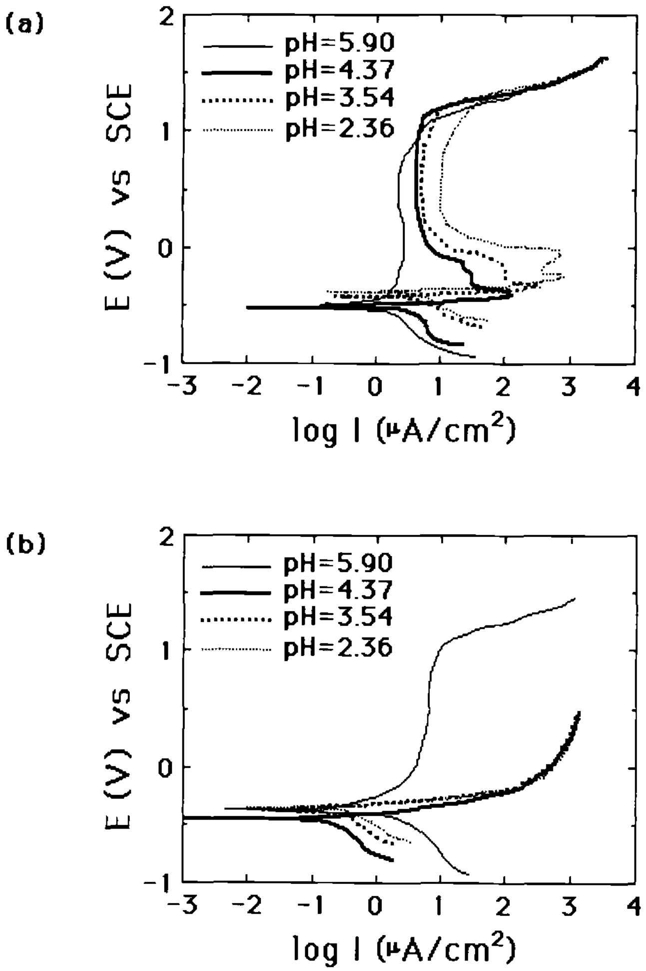

FIG. 2—*Effect of pH on PAP of* (a) *bulk and* (b) *plated permalloys at 1 mV/s scan rate.*

TABLE 3—*Passive current densities of bulk and plated permalloys in electrolytes with different pH values.*

	Passive Current Densities, μA/cm^2	
pH	Bulk	Plated
5.90	2.24	6.50
4.37	4.15	. . .[a]
3.54	5.10	. . .[a]
2.36	9.85	. . .[a]

[a] Active only, without any passive behavior.

acid additions. Similar differences between sputter-deposited and electroplated Fe-Ni films were reported in an earlier study [*10*].

Comparison of Bulk and Electroplated Permalloy

Figure 3 directly compares the polarization behavior of bulk permalloy and electroplated permalloy in seven different electrolytes. Bulk permalloy samples develop lower passive current densities in 0.1 *M* K_2SO_4 (Fig. 3*a*). Figures 3*b* to 3*d* show similar trends for both bulk permalloy and electroplated films in electrolytes with different chloride ion concentrations. Except for the highest concentrations, the chloride ion has a comparable influence on both types of samples. The pitting potential decreases with increasing chloride ion content, but the passive current density is not changed and is impressively low for both types of samples. For

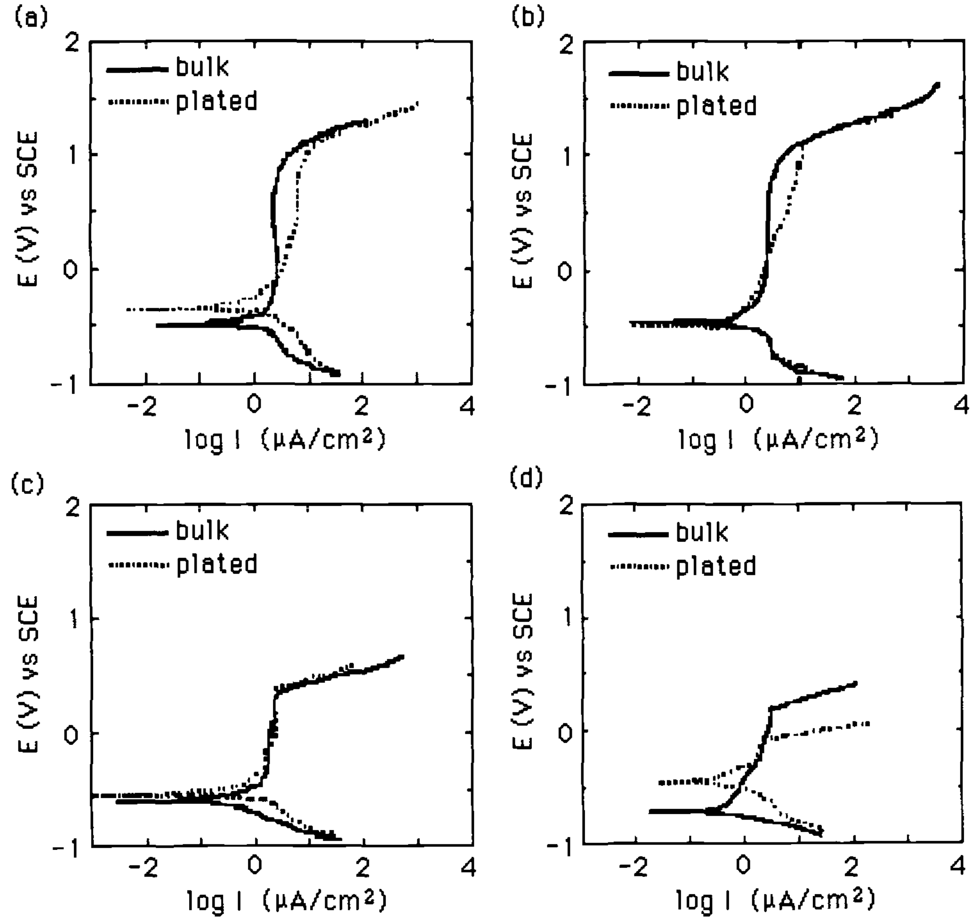

FIG. 3—*Comparisons of PAP between bulk and plated permalloys in seven different electrolytes:* (a) *0.1* M K_2SO_4; (b) *0.1* M K_2SO_4 + *0.01* M *KCl*; (c) *0.1* M K_2SO_4 + *0.1* M *KCl*; (d) *0.1* M K_2SO_4 + *1.0* M *KCl*; (e) *0.1* M K_2SO_4 + *0.0001* M H_2SO_4; (f) *0.1* M K_2SO_4 + *0.0005* M H_2SO_4; *and* (g) *0.1* M K_2SO_4 + *0.01* M H_2SO_4.

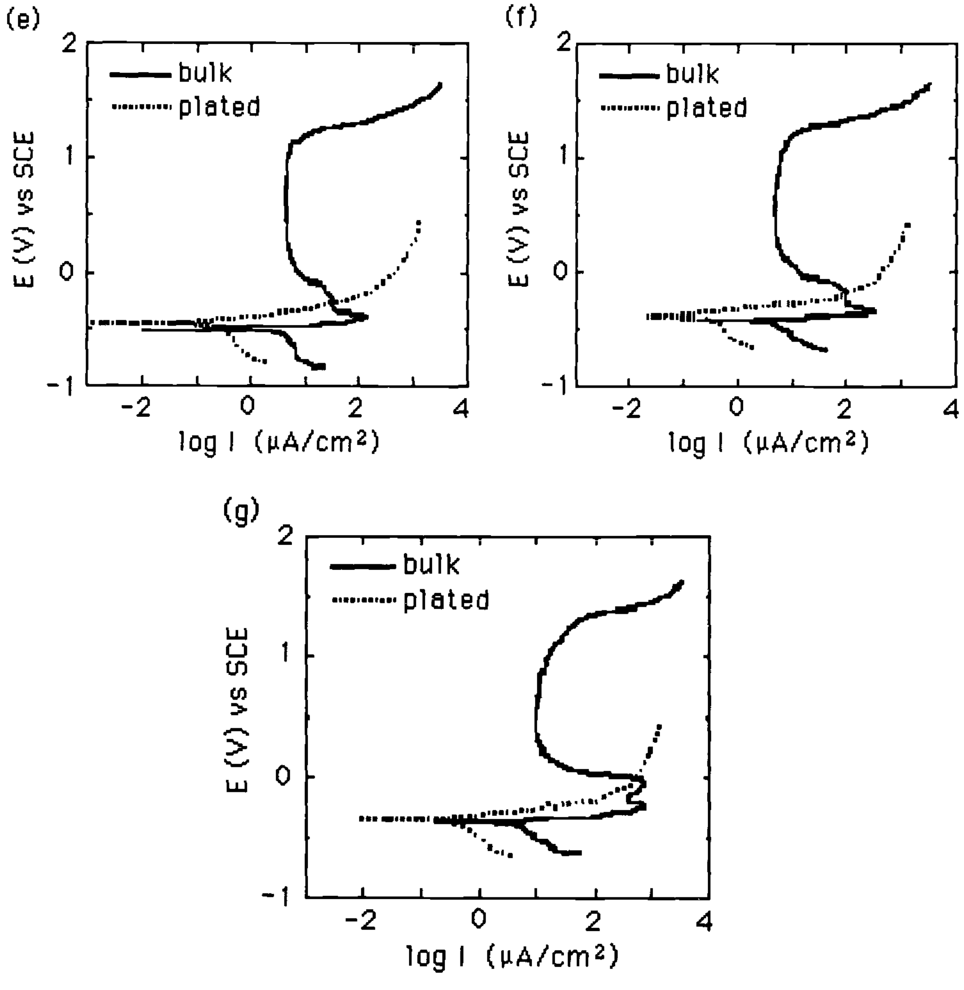

FIG. 3—*Continued.*

the highest chloride ion concentration (Fig. 3*d*), the electroplated permalloy has a lower breakdown voltage than bulk permalloy. Figures 3*e* to 3*f* compare the PAP results of bulk permalloy and electroplated permalloy in electrolytes of different pH values and show quite different behavior; bulk samples are typical of the passive behavior of Ni-rich alloys, whereas the EP films show only active behavior more typical of Fe-rich alloys [*10*].

Comparison of Composition, Morphology, and Crystal Structure

In an effort to explain the differences in the passive behavior of the electroplated samples and the bulk samples, we used a number of methods to characterize the composition, the composition uniformity, the crystal structure, the texture, and the grain structure. Figure 4 shows the XRD results of: (*a*) FCC Ni with random orientation distribution; (*b*) bulk permalloy; and (*c*) plated permalloy. Comparison of the relative peak heights establishes that the orientation distribution of bulk permalloy is random and that the electroplated permalloy has a (200) tex-

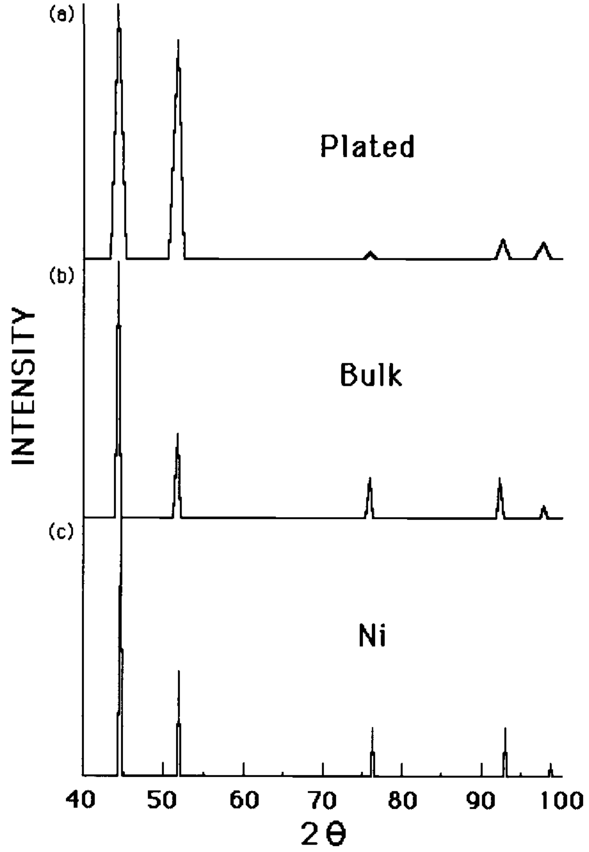

FIG. 4—*Comparison of Bragg-Brentano XRD results of:* (a) *plated permalloy;* (b) *bulk permalloy; and* (c) *FCC Ni with random orientation distribution.*

ture. In addition, there is a significantly smaller grain size in the electroplated permalloy, as evidenced by the larger half-peak widths of electroplated permalloy.

Table 4 gives the composition of the alloys, as obtained by EPMA-WDS. Five data points with 1000 Å probe size were taken; it was found that these two materials are homogeneous on the scale of the probe size and that there is no submicron-scale segregation. In addition, there were no impurities detected by EPMA that could be traced to contamination from the plating bath, such as sulfur, phosphorous, and chlorine. The difference in the passive behavior of the EP films and the bulk alloy (and for sputter-deposited alloys, as reported in an earlier study [*10*]) cannot be attributed to composition difference, composition segregation, or impurities.

The morphology of the PAP test surface of both specimens has been studied by SEM, as shown in Fig. 5. It is found that the grain size of bulk permalloy is about 20 mm and that the grain size of electroplated permalloy is very fine grain and is below the limit of detection with the SEM. The grain size of sputter-deposited films (SP) was also very fine, comparable in size to electroplated; however, the passive behavior of the sputter-deposited films is similar to the bulk material [*10*]. This indicates that grain size is not a dominant factor in their passive behavior.

We used TEM diffraction to compare the grain size on a finer scale and to check for a small

TABLE 4—*EPM-WDS composition analysis of bulk and plated permalloys.*

	Atomic % of Iron	
Data Point	Bulk	Plated
1	19.87	17.57
2	19.68	17.03
3	20.02	16.73
4	20.06	16.95
5	19.82	17.30
Average	19.89	17.12

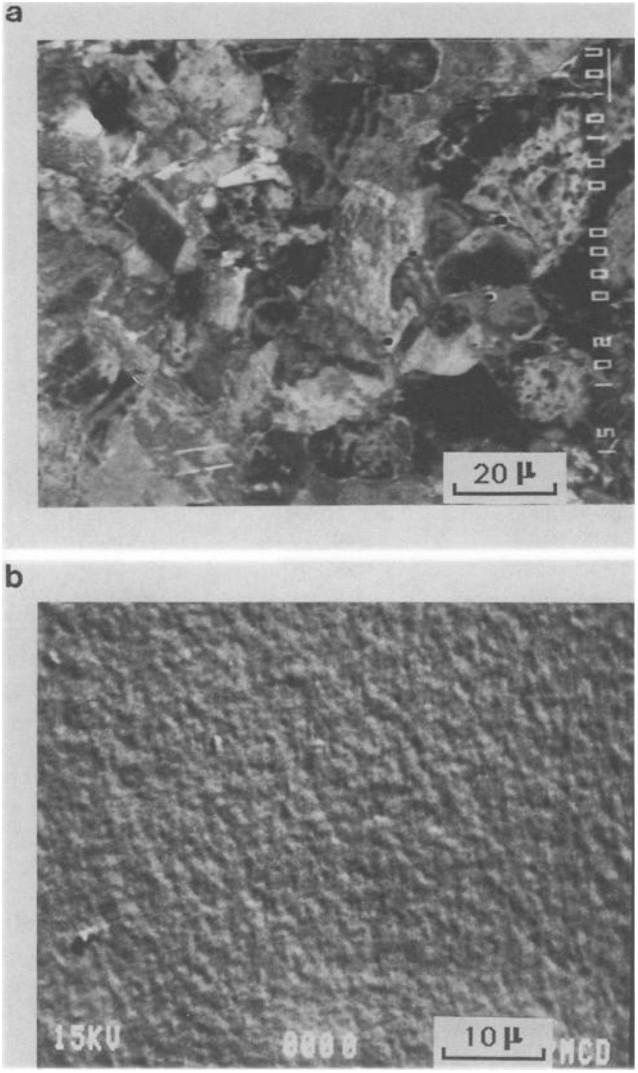

FIG. 5—*Secondary electron images of* (a) *bulk permalloy and* (b) *plated permalloy.*

amount of extra phase, too small to be detected by XRD. Figure 6*a* is a diffraction pattern of electroplated permalloy, and only the FCC phase is observed. Figure 6*b* is a bright field image of electroplated permalloy and shows that the grain size of the electroplated permalloy perpendicular to the plating direction is about 200 to 300 Å. Figure 7 is a cross-section TEM observation of the electroplated permalloy. Figure 7*a* is a low magnification bright field image which shows the glass substrate and the 2-mm-thick permalloy layer. Figure 7*b* is a high magnification bright field image which shows the glass substrate, the sputter-deposited seed layer (~1000 Å thick), and the initial electroplated layer. Figure 7*b* shows that sputter-deposited seed layers have sharp and straight grain boundary structure and that their columnar grains coalesce together tightly. Figure 7*c* and 7*d* are the bright field image and (111) dark field image

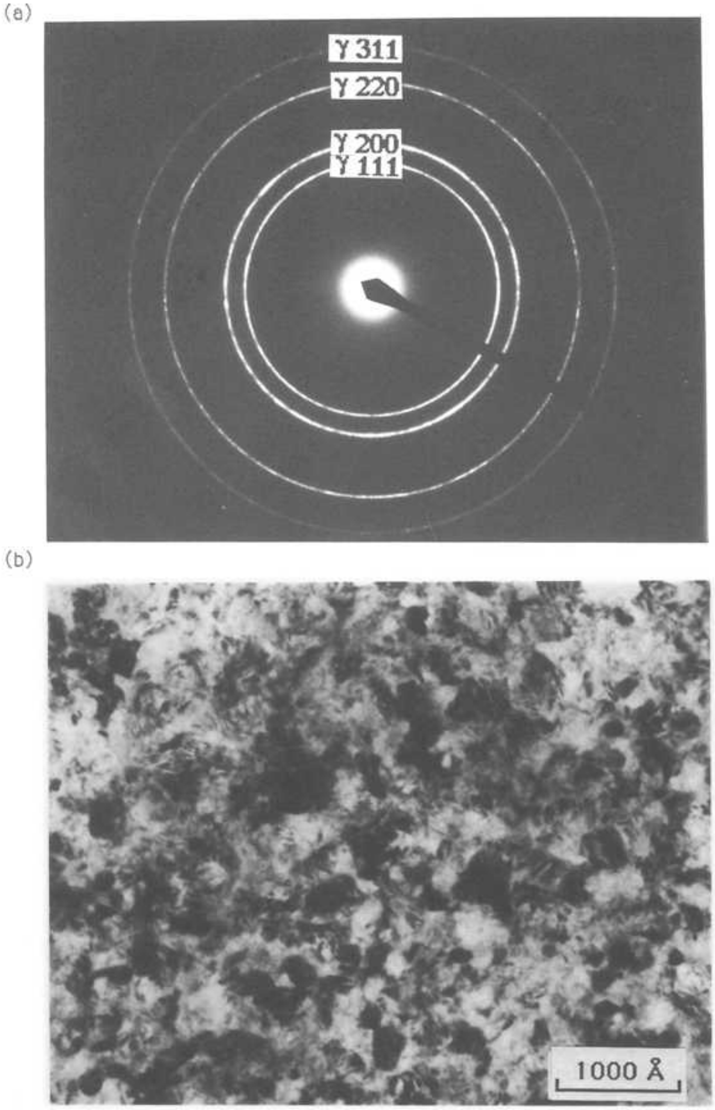

FIG. 6—*TEM plane views of plated permalloy films:* (a) *diffraction pattern;* (b) *bright field image.*

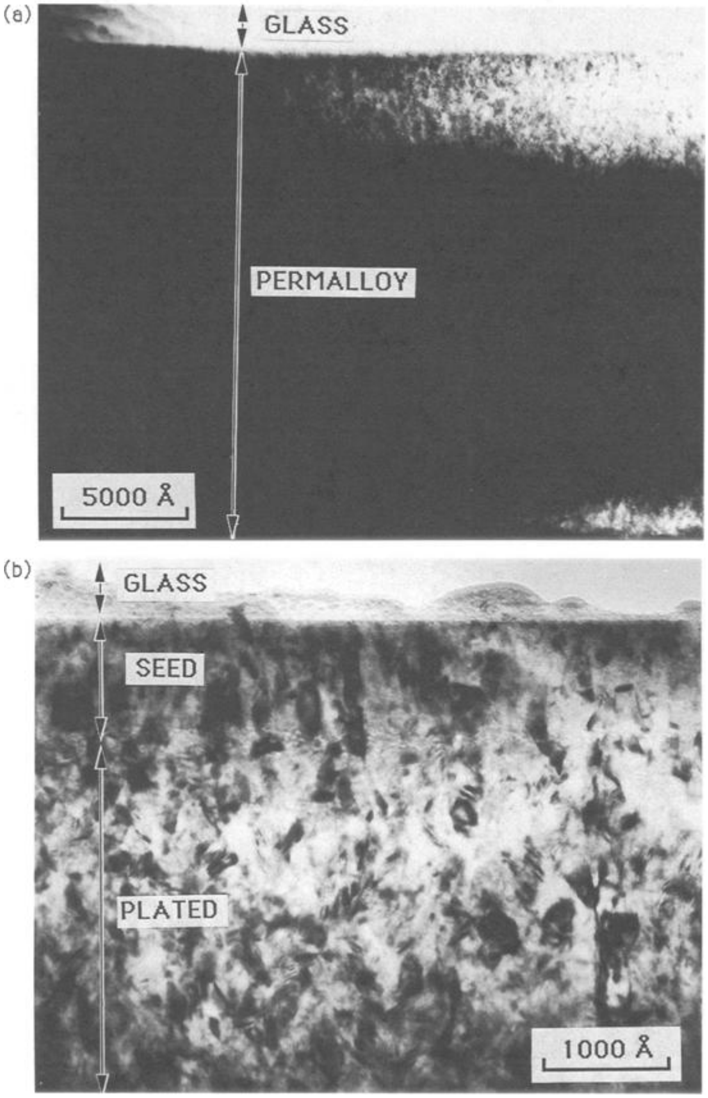

FIG. 7—*TEM cross-section images of plated permalloy thin film:* (a) *low magnification bright field image;* (b) *bright field image of sputtering deposited permalloy seed layer and initial plated permalloy layer;* (c) *bright field image of plated permalloy; and* (d) *(111) dark field image of plated permalloy.*

of the middle part of the electroplated permalloy layer and show that the electroplated permalloy also has a columnar structure. However, there is not a sharp boundary between the neighboring columnar grains of the plated layer; there appears to be a loose transition between the grains, which may provide localized regions of preferred corrosion. This may explain that the electroplated permalloy has the higher passive current density in 0.1 M K_2SO_4 and active-only behavior in acidic electrolyte, and a lower breakdown voltage in higher chloride ion concentrations. Similar observations are reported by T. G. Wang and G. W. Warren [*12*] and by C. M. Egert [*13*].

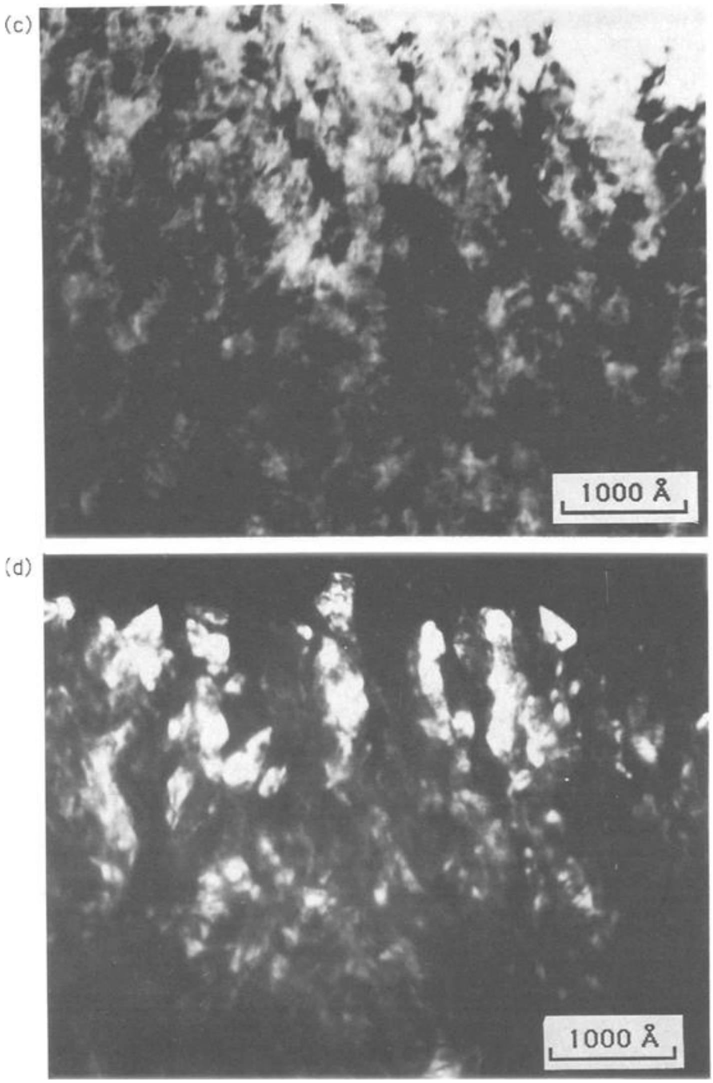

FIG. 7—*Continued.*

Summary

1. In both bulk permalloy and electroplated permalloy films, the pitting potentials decrease with increasing chloride ion concentration, but both types of samples show impressively low passive current densities in the presence of chloride ions. At higher choloride ion concentrations, the electroplated permalloy films show a lower pitting potential.

2. For the bulk permalloy samples, the corrosion potential, the primary passive potential, the critical current density, the passive current density, and the pitting potential increases with decreasing pH.

3. The electroplated permalloy shows only active behavior in acidic electrolytes, although it has the same crystal structure and almost the same composition as bulk permalloy.

4. The microstructure characteristics of electroplated permalloy film are: (a) there is no observable composition segregation with probe size of 1000 Å; (b) only the face centered cubic (FCC) phase is detected in both XRD and TEM selected small area diffraction studies; (c) there is a columnar grain structure with 200 to 300 Å in diameter and about 1000 Å in length; and (d) there is a (200) texture.

5. Based on the present work and previous work [*10*], we propose that the grain structure of the electroplated permalloy is responsible for the difference in the passive behavior of the two types of samples studied; in particular, the loosely bonded columnar grains of the EP films provide localized points for preferential attack.

Acknowledgments

The authors express their appreciation to International Business Machines, Storage Systems Product Division for financial support and to Hewlett Packard Laboratories for assistance in instrumentation. Helpful and illuminating discussions with A. Yen, P. Long, and D. Wong are gratefully acknowledged.

References

[*1*] Brundle, C. R., Silverman, E., and Madix, R. J., *Journal of Vacuum Science and Technology*, Vol. 16, 1979, p. 474.
[*2*] Lee, W. Y., Scherer, G., and Guarnieri, C. R., *Journal of Electrochemistry Society*, Vol. 126, 1979, p. 1533.
[*3*] Pollak, R. A. and Bajorek, C. H., *Journal of Applied Physics*, Vol. 46, 1975, p. 1382.
[*4*] Cohen, S. L., Russak, M. A., Baker, J. M., McGuire, T. R., Scilla, G. J., and Rossnagel, S. M., *Journal of Vacuum Science and Technology*, Vol. A6, 1988, p. 918.
[*5*] Rice, D. W. and Suits, C. J., *Journal of Applied Physics*, Vol. 50, 1979, p. 5899.
[*6*] Rice, D. W., Suits, C. J., Nepela D., and Tremoureux, R., *Journal of Applied Physics*, Vol. 50, 1979, p. 7089.
[*7*] Rice, D. W., Suits, C. J., and Lewis, S. J., *Journal of Applied Physics*, Vol. 47, 1976, p. 1158.
[*8*] Eriksson, H. and Salwen, A., *IEEE Transactions of Magnetism*, Vol. 13, 1977, p. 1451.
[*9*] Lee, W. Y. and Eldridge, J., *Journal of Electrochemistry Society*, Vol. 124, 1977, p. 1747.
[*10*] Bornstein, J. G., Lee, C. H., Capuano, L. A., and Stevenson, D. A., *Journal of Applied Physics*, Vol. 65, 1989, p. 2090.
[*11*] Flinn, P. A. and Waychunas, G. A., *Journal of Vacuum Science and Technology*, Vol. B6, 1988, p. 1749.
[*12*] Wang, T. G. and Warren, G. W., *IEEE Transactions on Magnetics*, Vol. MAG-22, No. 5, 1986, p. 340.
[*13*] Egert, C. M., *Corrosion—NACE*, Vol. 44, No. 1, 1988, p. 36.

ISBN 0-8031-1470-2